ALMA MATER STUDIORUM
UNIVERSITÀ DEGLI STUDI DI BOLOGNA
Facoltà di Scienze Matematiche Fisiche e Naturali

Dottorato di Ricerca in Geofisica
XXIII Ciclo

Settore scientifico disciplinare di afferenza: GEO/10

"IMAGING OF CRUSTAL SCATTERERS USING MULTIPLE SEISMIC ARRAYS"

Ph.D. Thesis of:
Pamela Roselli

Tutor:
Dr. Thomas Braun

Supervisor:
Dr. Andrea Morelli

Coordinator:
Prof. Michele Dragoni

2011

RINGRAZIAMENTI

Sono troppe le persone a cui sento di dovere davvero tanto...

If I successfully finished my PhD, thanks to ***Dr. Matthias Ohrnberger*** *with his patience, professionalism, and scientific intelligence to understand and to resolve my difficulties both during my stay in Potsdam and in Rome (internet-mails); I can define fruitfully and scientifically stimulating to work together.*
Moreover, I would like to thank ***Dr. Frank Krüger*** *for introducing me to the University of Potsdam giving me the possibility to start this interesting joint work.*
I want to thank all my "german"-"international"colleagues (Lilian, Tobias, Josnella, Vero, Carsten, Lydia, Carolina) and Tanja because they made me feel at home with parties, "Italian"-coffee-breaks and ice-cream-breaks.. during my stay in Potsdam.

Vorrei ringraziare la mia RUF, **Dott.ssa Claudia Piromallo** per la professionalità, l'umanità, l'infinita disponibilità dimostrata durante questi tre anni; i preziosi consigli e il tempo che ha saputo dedicarmi.
Vorrei ringraziare il mio Direttore, **Dr. Antonio Piersanti** per l'interesse dimostrato verso questo lavoro e la giusta grinta che mi ha saputo trasmettere.
Vorrei ringraziare il mio Relatore, **Dr. Thomas Braun** per avermi appoggiato in questo lavoro.
Vorrei ringraziare la **Dott.ssa Diana Latorre** per la sua disponibilità, la sua costante assistenza ed i suoi continui incoraggiamenti.

Se sono riuscita a portare a termine questo lavoro di Dottorato lo devo anche a Paola (oramai mia consulente), Marina (alias "Tonna" con gli indimenticabili "Happy-Travels"), Alessia, ai compagni del caffè Mauro e Mario (con il quale siamo ormai alla seconda tesi condivisa) ai "Pollajoli" o "Ex-Pollajoli" o presunti tali (Danilo, Michele, Monica, Luisa, Cosmiana, Christos).
Un ringraziamento speciale va ad Antonella e Marta, soprattutto per la pazienza.

Sono felice di aver avuto la possibilità di condividere questi 3 anni (dei 12..) in compagnia della mia Danielina (che ha conquistato un'altra volta un posto nei ringraziamenti di una mia tesi….e nella mia vita) e Laila (alias "Nana") il cui supporto è stato indiscutibile (soprattutto nei giorni precedenti alla consegna in cui è scappata in Tanzania).

Un grazie a Mamma e Papà che continuano ad avere fiducia in me.

Mamma & Papà

INDEX

Abstract

Array seismology is an useful tool to perform a detailed investigation of the Earth's interior. Seismic arrays by using the coherence properties of the wavefield are able to extract directivity information and to increase the ratio of the coherent signal amplitude relative to the amplitude of incoherent noise. The Double Beam Method (DBM), developed by *Krüger et al. (1993, 1996)*, is one of the possible applications to perform a refined seismic investigation of the crust and mantle by using seismic arrays. The DBM is based on a combination of source and receiver arrays leading to a further improvement of the signal-to-noise ratio by reducing the error in the location of coherent phases. Previous DBM works have been performed for mantle and core/mantle resolution (*Krüger et al., 1993; Scherbaum et al., 1997; Krüger et al., 2001*). An implementation of the DBM has been presented at 2D large-scale (Italian data-set for M_w=9.3, Sumatra earthquake) and at 3D crustal-scale as proposed by *Rietbrock & Scherbaum (1999)*, by applying the revised version of Source Scanning Algorithm (SSA; *Kao & Shan, 2004*). In the 2D application, the rupture front propagation in time has been computed. In 3D application, the study area (20x20x33 km^3), the data-set and the source-receiver configurations are related to the KTB-1994 seismic experiment (*Jost et al., 1998*). We used 60 short-period seismic stations (200-Hz sampling rate, 1-Hz sensors) arranged in 9 small arrays deployed in 2 concentric rings about 1 km (A-arrays) and 5 km (B-array) radius. The coherence values of the scattering points have been computed in the crustal volume, for a finite time-window along all array stations given the hypothesized origin time and source location. The resulting images can be seen as a (relative) joint log-likelihood of any point in the subsurface that have contributed to the full set of observed seismograms.

CHAPTER 1

Introduction

In the last years, important advances have been conducted in seismology. With the recent developments in the fields of communication and information technology, the tools for geophysical investigation have reached a new standard level. Both old approved and new seismological methodologies, have provided a formerly unknown degree of resolution e.g. when imaging the velocity distribution and the discontinuities of the crust, mantle and core-mantle. Moreover, a key role was played by the high accuracy of the seismic stations equipped by three component broad-band sensors, providing high quality data that represent the basis for high resolution analyses. All these progresses have been useful to better understand the complex physical, chemical, geological and geodynamic processes that characterize the Earth and strongly connect one another. Furthermore, detailed geophysical investigations can give important contributions to better understand rupture processes committed to the study of seismic hazard and the management of energy resources. Since their development in the 1960s, seismic arrays have given a new impulse to seismology and nowadays they have become an indispensable tool to investigate the Earth's interior. Recordings from many uniform seismometers in a well-defined, closely spaced configuration produce high-quality and homogeneous data sets with accurate timing, which can be used to study the Earth's structure in great detail. For this purpose many different, specific array techniques have been developed and applied to an increasing number of high-quality array data sets. Most processing methods use the ability of seismic arrays to measure the vector velocity of an incident wave front, i.e., slowness and back-azimuth. This information can be used to discriminate between seismic phases, separate waves from different seismic events and improve the signal-to-noise ratio by stacking

with respect to the varying phase slowness. The vector velocity information of scattered or reflected phases can be used to determine the region of the Earth from whence the seismic energy comes and with what structures it interacted. Therefore seismic arrays are perfectly suited to study the small-scale structure and variations of the material properties of the Earth. Most of traditional array methods (i.e. beamforming, f-k analysis, vespagram) assume that the energy arriving at the array can be approximated as a plane wavefront. This is a proper assumption for most arrivals from teleseismic source-receiver distances, but breaks down for local distances where source and array are separated by less than a few array apertures (curved wavefront), and for phases originating close to the array, such as scattered energy or P-wave to Rayleigh wave conversions.

In this work a small scale analysis oriented to the investigation of the local crustal scattering structure has been performed, where the receiver arrays, the sources and the scatterers are situated close to each other. To this scope, unconventional seismological tools such as the Double Beam Method (DBM; Krüger et al., 1993, 1996) and the Source-Scanning Algorithm (SSA; Kao & Shan, 2004) have been applied and originally implemented into the software package CAP (Continuous Array Processing; Ohrnberger 2004) in order to obtain images in both space and time of seismic sources and scattering points. The DBM is based on a joint use of source and receiver arrays leading to a further improvement of the signal-to-noise ratio, with respect to traditional array methods, by reducing the error in the location of coherent phases. The DBM has been implemented at a crustal-scale, as formerly proposed by Rietbrock & Scherbaum (1999), by applying a revised version of the SSA (Kao & Shan, 2004). The result of the algorithm is not just a sum of absolute amplitudes; instead, a normalization with respect to the number of receivers and a scanning for time windows (named *slices*) along all the trace have been introduced. Moreover, in the present approach, the reference time is assumed to be fixed for all hypothetical source points and the concepts of migration and back-propagation of energy have not been applied. The study crustal volume (20x20x33 km^3), the data-set and the source-receiver

configurations used are related to the KTB-1994 (Bavaria, Germany) seismic experiment (Jost et al., 1998), running 60 short-period seismic stations arranged in 9 small arrays deployed in 2 concentric rings around the borehole. In order to setup an analysis procedure capable to apply the DBM, a "pseudo realistic" synthetic data-set was created, based on the real source-receiver configuration of the KTB-1994 experiment and on a 1-D velocity model of the study area. Two different typologies of sources have been simulated: an explosion and a double-couple event. The application of the revisited SSA to the computed synthetic seismograms for both sources was realized by using the CAP-code (Ohrnberger, 2004). Many different array configurations and parameters setting have been tested and the coherence values of the phases generated from each scatterer have been computed estimating the semblance (Douze & Laster, 1979) distribution images as a function of depth. The best results have been obtained from the source-array, the receiver-array and their combination that constitutes the double beam. This new approach to Array Seismology opens new perspectives to the investigation geophysics, offering a dynamic point of view for both the Earth structural studies and the rupture processes. Moreover, it is interesting to consider the different scales, both local and global, at which this approach can be applied.

Following this Introduction, in the second Chapter the Array Seismology state-of-art is described; in the third Chapter the theory of Source-Scanning Algorithm is introduced and a 2D application is presented; in the fourth Chapter the methodology is discussed and the implementation is illustrated; in Chapter five details on the receivers, data, parameterization and CAP-code are shown; in Chapter six the final results are described and discussed; in Chapter seven the conclusions of the work are exposed.

CHAPTER 2

Array Seismology

In the following section a short introduction to array seismology is given. After an historical overview, examples about array installations (both in Italy and in the world) are shown. The array principles of traditional and advanced method are shortly described: f-k analysis, beamforming, vespagram and Array Response Function.

2.1 Seismic Array: overview

The idea to adopt array techniques to seismology came from the necessity to detect underground nuclear explosions. During the cold war the political partition of the world in east and west did not allow to surround the nuclear test sites of the "enemy" by sufficiently near installed seismic stations, a necessary condition for seismic networks to determine the hypocentre and to estimate the energy (magnitude) of small and moderate seismic events. In order to lower the detection threshold, array techniques, mainly developed in radio astronomy, radar and acoustics (Williams et al., 1980; Haykin, 1985; Tarenghi, 2008), have been implemented in seismology. Those techniques improve the signal-to-noise ratio, by using the coherence properties of the wavefield. Seismic array analysis can be described by the same basic mathematical principles as those that apply for arrays of antennae used in radio-astronomy or radar science (Capon 1969; Harjes & Henger, 1973) and they have the same effect on seismology as the widespread use of powerful telescopes has on modern astronomy. Generally, an array is a spatial cluster of instruments, with identical recording characteristics and central timing. Depending on the wavelength of the interesting wavefield, the frequency characteristics of the recording sensors, the relative inter-station distances and the array aperture must be chosen in such a way, that the analyzed signal is coherent. The first seismic arrays to detect underground nuclear

explosions were introduced in the late 1950s (Carpenter, 1965). Since the 1960s it has been demonstrated that seismic arrays are superior to single three-component stations for detecting and characterizing signals from explosions and earthquakes. The lowering of the detection threshold for global seismic events opened a new perspective in geophysics, and soon it came out that array techniques as a new type of seismological tool helped to provide a possibility of resolving the fine structure of the Earth's interior (e.g., Birtill & Whiteway, 1965; Wright, 1972; Doornboos & Husebye, 1972; Kværna, 1989; Weber et al., 1996). A seismic array differs from a local network of seismic stations mainly by the way in which the data are processed. Thus, in principle, a network of seismic stations can be used as an array, and data from an array can be analyzed as from a network. One of the main advantages of seismic arrays, compared to single seismological stations, is the improvement of the signal-to-noise ratio (SNR) due to the constructive summation of the coherent signals (beamforming) and the suppression of the incoherent noise. In general, array data show very high signal coherence across the whole array aperture as well as low coherence of noise between the individual stations. Signal coherence is dependent on local structure and noise conditions, on array design and on the frequency content of the signal of interest (Rost & Thomas, 2009). Many different array configurations exist, that have been optimized for specific purposes (Haubrich, 1968). The processing tools require small timing uncertainties between the individual channels of a network or array that, due to the common time base of seismic array, is not a problem (Rost & Thomas, 2002; Rost & Thomas, 2009). In addition, the seismic arrays can provide directional information (back-azimuth) and the apparent velocity of different seismic signals, which is important for the classification of signals (P, S, regional or teleseismic (Schweitzer et al., 2002). The merits of array data for signal detection and event location are beyond question (Braun & Schweitzer, 2008) and nowadays applications in seismology are manifold: seismic arrays led to refined velocity models of the Earth's interior (e.g. Kárason & van der Hilst, 2001), high resolution tomographic images on regional scale (e.g., Arlitt et al., 1999; Ritter et

al., 2001), detection of small-scale structures in the Earth's mantle (e.g., Castle & Creager, 1999; Krüger et al., 2001), the core-mantle boundary (e.g., Thomas et al., 1999; Rost & Reveraugh, 2001; Rost, 2010) and heterogeneities in the inner core (e.g., Vidale & Earle, 2000).

2.1.1 Examples in the World

In the last 40 years numerous seismic arrays at different scales have been installed in the world and array data have been used both to control the compliance of the Comprehensive Test Ban Treaty (CTBT) and for fundamental research. Experiments have been carried out with a wide variety of array designs. The first experimental seismic array with more than four elements was established in February 1961 by the United Kingdom Atomic Energy Agency (UKAEA) on Salisbury Plain (UK), followed in December 1961 by Pole Mountain (PMA, Wyoming, USA), in June 1962 by Eskdalemuir (EKA, Scotland, UK), and in December 1963 by Yellowknife (YKA, Canada), each of them with open data access. These types of arrays (the so called UK-arrays) are orthogonal linear or L-shaped. In the 1960s, arrays were tested with very different aperture and geometry, from small circular arrays with apertures of some kilometres to huge arrays with apertures of up to 200 km. The first large arrays were the LASA array in Montana (USA), built in 1965, with 525 seismometer sites (Frosch & Green, 1966) and the original NORSAR array in southern Norway consisting of 132 sites over an aperture of approximately 100 km with 198 seismometers, which became fully operational in the spring of 1971 (Bungum et al., 1971). Some of the most significant arrays are listed in Table 2.1 and examples of some array configurations are shown in Figure 2.1 (from Douglas et al., 2002).

Location	Code	Aperture (km)	No. of Seismometers	Operating Period	Remarks
Southeastern Norway	NORESS	3	25	Fall 1984 to date	Small aperture
Wichita Mts., OK, USA	WMSO	5	13	1964–July 1969	Small aperture
Eskdalemuir, Scotland	EKA	10	20	May 1962 to date	Medium aperture
Yellowknife, Canada	YKA	25	19	Nov 1962–May 1963 and Dec 1963 to date	Medium aperture. Gauribidanur (GBA) India and Warramunga (WRA) Australia are arrays of similar design
Billings, MT, USA	LASA	200	525	1965–1978	The large aperture seismometer array; 21 subarrays each of 25 seismometers

Table 2.1: Examples of Short-Period Seismometer Arrays (from Douglas, 2002).

The large LASA and NORSAR arrays and the UKAEA arrays have narrow band short-period seismometers and additional long-period seismometers in their original configuration, whereas the Gräfenberg Array (GRF) was planned and installed in the early 1970s in the south of Germany as an array of broadband sensors. It has an aperture of about 100 km (Harjes & Seidl, 1978; Buttkus, 1986) and an irregular shape (Fig. 2.2), which follows the limestone plateau of the Franconian Jura (Schweitzer et al., 2002). The processing algorithms for large arrays are different from the processing techniques used for the smaller arrays (Douglas, 2002).

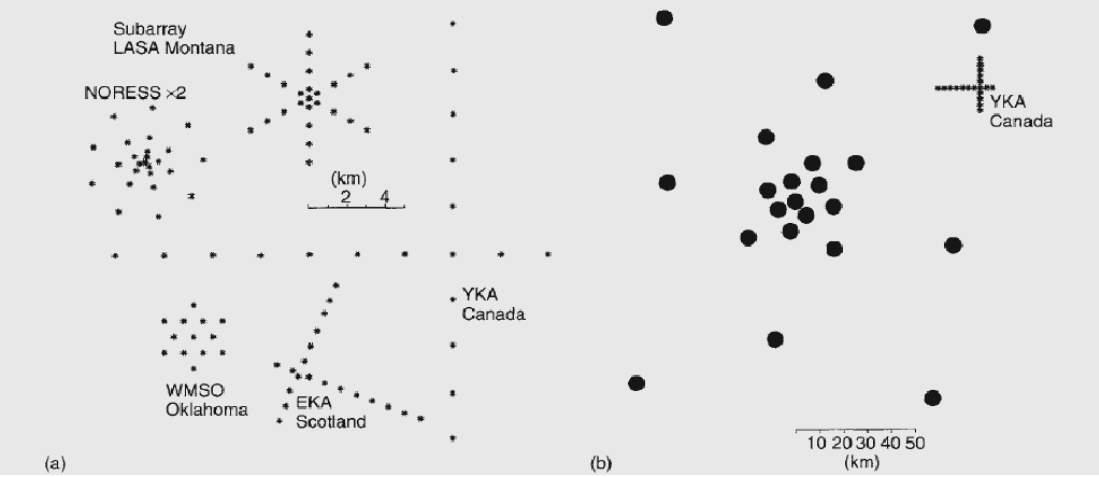

Figure 2.1: Examples of the layout used in short-period seismometer arrays. (a) Seismometer positions in some small- and medium-aperture arrays and a LASA subarray. The NORESS array is shown at twice the scale of the other arrays. (b) The sub-array within the LASA. The layout of YKA is superimposed on the figure to show the relative size of this array and the LASA (Douglas, 2002).

At the NORSAR Data Processing Centre (NDPC) at Kjeller, Norway, data have been acquired for many years from different types of arrays: e.g., the large aperture NORSAR array (aperture of 3 km), the small aperture arrays NORES (regional array of south of Norway) and ARCES (regional array of northern of Norway with seismometers located on concentric rings) and the very small aperture arrays at Spitsbergen and in Apatity, Kola peninsula. In general, the geometry and the number of seismometer sites of an array are determined by economy and purpose. Details about array configurations can be found in Haubrich (1968), Harjes & Henger (1973), or in Mykkeltveit et al. (1983, 1988). Large networks of seismometers have been installed to study Earth structure: GHENGIS (Roecker, 2001), EAGLE (Bastow et al., 2005), CANOE (Mercier et al., 2008), USARRAY (Henyey, 2000) and have proven their ability to resolve the structure of the Earth in great detail.

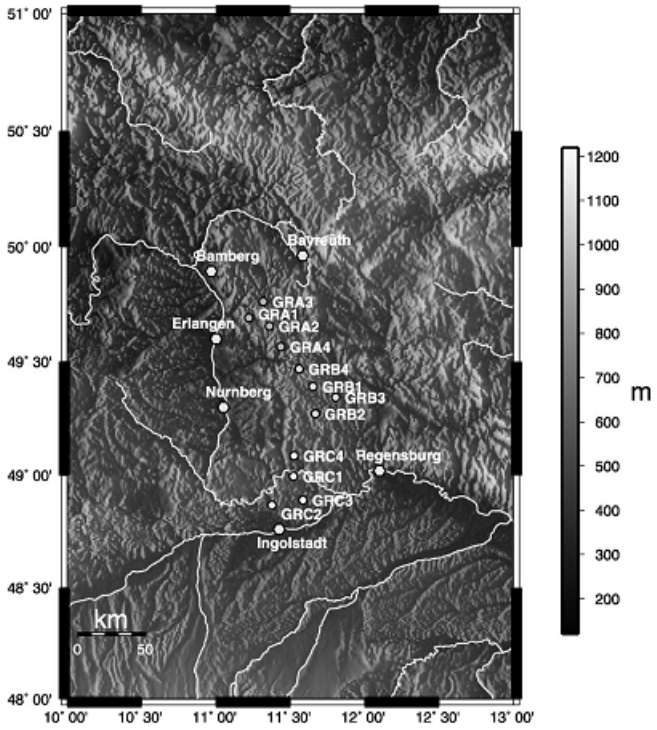

Figure 2.2: Location of the array stations of the GRF array. The circles represent the location of one-component vertical STS-1 broadband seismometers. Three of the stations (GRA1, GRB1, and GRC1) are equipped with three-component STS-1 seismometers (from Rost & Thomas, 2002).

In the last years very small temporary seismic arrays (aperture of about 8 km) have been installed to better understand in detail the structure, the geology and the possible interactions existing between the earthquakes and the fluids in the crust. In particular, the effects produced by the induced micro seismicity have been studied using array-techniques within the International Continental Drilling Program (ICDP) in the German Continental Deep Drilling Project KTB-1994 (Zoback et al., 1997; Jost, 1998) KTB-2000 (Baisch, 2002), for details see Chapter 5.

2.1.2 Examples in Italy

The diffusion of seismic arrays has been concentrated mainly in the USA, Germany and Norway. In Italy, temporary small aperture seismic arrays have been installed in the nineties to analyse volcano-seismic signals, as e.g. on Stromboli volcano (Neuberg et al., 1994), Saccorotti & Del Pezzo (2002). Also for the study of the microseismicity near the Alto Tiberina Fault (Central Italy), temporary small scale arrays have been installed (Braun & Schweitzer, 2008) , like a nine-element array near Città di Castello (aperture 2 km) and a 12-element array (aperture 3 km) to study the Non Volcanic Tremor (Shelly et al., 2007) in Northern Apennines (Braun et al., 2006). The only fix array installation in Italy has been deployed in central Italy inside the Gran Sasso Observatory (Scarpa et al., 2004; Saccorotti et al., 2006).

2.2 Traditional Array Methods

During the last 40 years, numerous array processing methods have been developed that use the high signal coherence and accurate timing of array data to generate high-resolution images of the Earth structure. Most array methods assume that the energy arriving at the array can be approximated as a plane wavefront. This is a good assumption for most arrivals from teleseismic source-receiver distances, but breaks down for local distances where source and array are separated by less than a few array apertures (curved wavefront), and for phases originating close to the array such as scattered energy (Thomas et al.,

1999) or P-wave to Rayleigh wave conversions (Clouser & Langston, 1995). For distances from the source much larger than the array aperture (i.e., more than about 10 wavelengths) a seismic wave approaches an array with a wavefront close to a plane (Schweitzer et al., 2002). An array is defined by a set of seismometers with one seismometer being assigned the role of a reference site. The relative distances from this reference point to all other array sites are used later in all array specific analysis algorithms. The propagation direction of elastic waves travelling in a spherical Earth and arriving at a seismological array can be described by two parameters (Fig. 2.3):

- vertical incident angle *i*. In practice, not the incident angle *i* but the inverse of the apparent velocity of the wave front across the array is used. This parameter is called slowness u v_0

$$\boldsymbol{u} = \frac{1}{\boldsymbol{v}_{app}} = \frac{\sin i}{v_0}; \qquad (2.1)$$

where v_0 is the medium velocity beneath the array.

- Back-azimuth θ is the angle of the wave front arriving at the array measured clockwise between the north and the direction to the epicentre in degrees.

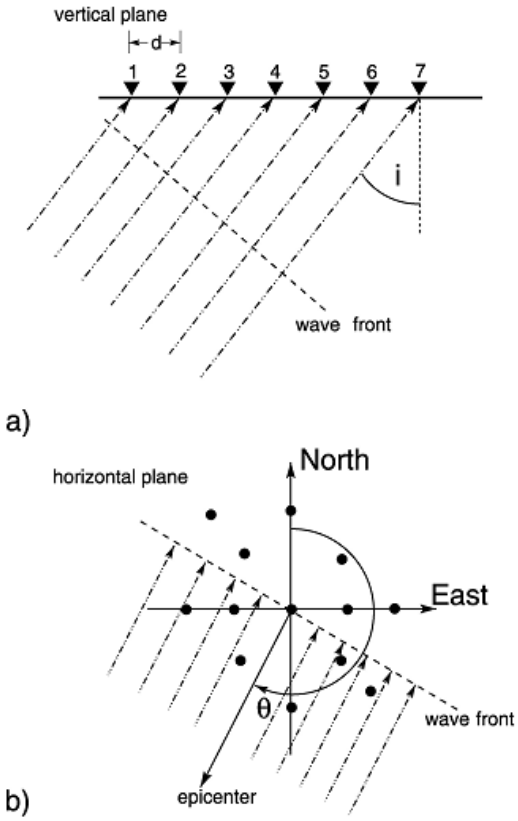

Figure 2.3: (a) The vertical plane of an incident wave front crossing an array at an angle of incidence *i*. (b) Sketch of the horizontal plane of an incident plane wave arriving with a back azimuth θ (from Rost & Thomas, 2002).

Both parameters are combined in the slowness vector **u**. In a spherical geometry this is:

$$\boldsymbol{u} = (u_x, u_y, u_z) = \left(\frac{\sin\theta}{v_{app}}, \frac{\cos\theta}{v_{app}}, \frac{1}{v_{app}\tan i}\right) = u_{hor}\left(\sin\theta\,, \cos\theta, \frac{1}{\tan i}\right)$$

$$= \frac{1}{v_0}(\sin i \sin\theta\,, \sin i \cos\theta\,, \cos i); \qquad (2.2)$$

The geometry of the slowness vector is shown in Figure 2. 4. The slowness vector **u** is oriented in the direction of wave propagation, and its modulus is the reciprocal of the wave speed.

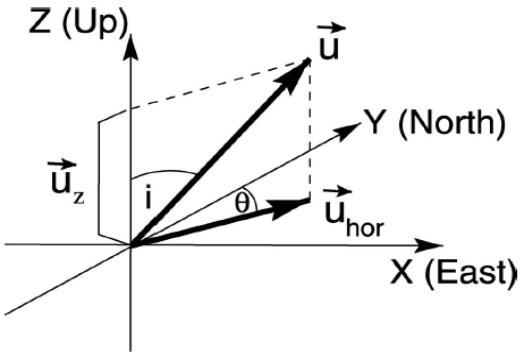

Figure 2.4: Components of the slowness vector **u**. The components incident angle *i* and back azimuth θ are marked. The slowness vector is normal to the incident wave front (from Rost & Thomas, 2002).

The ray parameter p and the horizontal slowness u_{hor} are interdependent:

$$p = \frac{r \sin i}{v} = \frac{R_0 \sin i}{v_0} = R_0 u_{hor}; \qquad (2.3)$$

R_0 is the distance of the turning point of the ray from the Earth's centre. Therefore the velocity at the turning point of the ray can be determined from the slowness. The seismic velocity below the array in the uppermost crust and the angle of incidence define the apparent propagation speed of the wavefront crossing the array (Schweitzer et al., 2002). This is not the physical propagation speed of the wavefront, therefore it is called *apparent velocity*. The estimates of the station-to-event back-azimuth and the apparent velocity of different types of signals are important both for event location purposes and for classification of signals, e.g., P, S, local, regional, or teleseismic events. If the arrival is a phase for which the slowness is known as a function of distance, the epicentral distance can be estimated and combined with the azimuth estimate to give a rough epicentre (and origin time), for an assumed focal depth (Douglas et al., 2002). Due to the discrete locations of the elements of the array, an incoming wavefront will arrive with small time offsets (or delay times) t between the stations, which depend on

the slowness vector **u** and the station location (characterized by the location vector $\mathbf{r}_j$):

$$t_j = \boldsymbol{r_j} \cdot \boldsymbol{u}; \qquad (2.4)$$

Measuring the time delays t_j between individual stations and knowing the station locations $\mathbf{r}_j$ therefore allows a direct measure of the slowness vector **u** (Fig. 2.4, 2.5, 2.6).

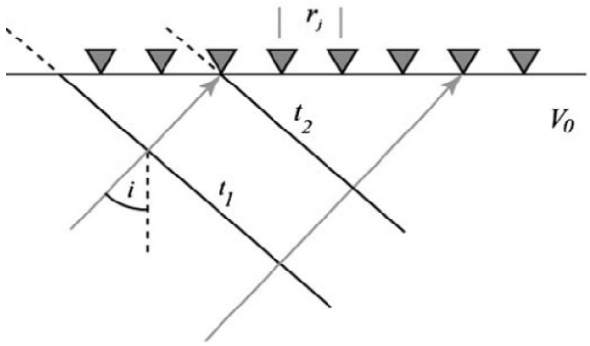

Figure 2.5: Due to the incident angle the plane wavefront travels across an array at the surface with an apparent velocity v_{app} dependent on the incident angle *i*. Since the array station locations are known this can be used to calculate the slowness. $\mathbf{r}_j$ are the locations of the stations from the centre station (from Rost & Thomas, 2009).

The accuracy of the measurement of the slowness vector depends on the quality of the timing between the station and on the station location (Rost & Thomas, 2009).

2.2.1 Beamforming

With an array we can improve the signal-to-noise ratio (SNR) of a seismic signal by summing the coherent signals from the single array sites. The arrival times for a seismic wave at each station of a seismic array can be estimated for each angle of incidence and hence it is possible to stack the recordings of the individual stations to enhance arrivals with known slowness *u* and/or back-azimuth θ by taking the inter-station delay times into account before stacking. This process is

called beamforming or "delay-and-sum" technique (Harjes & Henger, 1973; Rost & Thomas, 2002; Schweitzer et al., 2002). Beamforming uses the differential travel times of the plane wave front due to a specific slowness and back azimuth to individual array stations. If the single-station recordings are appropriately shifted in time for a certain back-azimuth and slowness, all signals with the matching back azimuth and slowness will sum constructively. The array centre is either a central instrument or the geometrical centre of the array. The incident wave field with the signal $f(t)$ and noise $n_i(t)$ with variance σ^2 is recorded at the centre station of the array as the time series:

$$x_{center}(t) = f(t) + n_i(t); \qquad (2.5)$$

Owing to the different locations of the array stations the incident wave front has different travel times to each station. The travel time difference is a function of the slowness of the wave front and the sensor location.

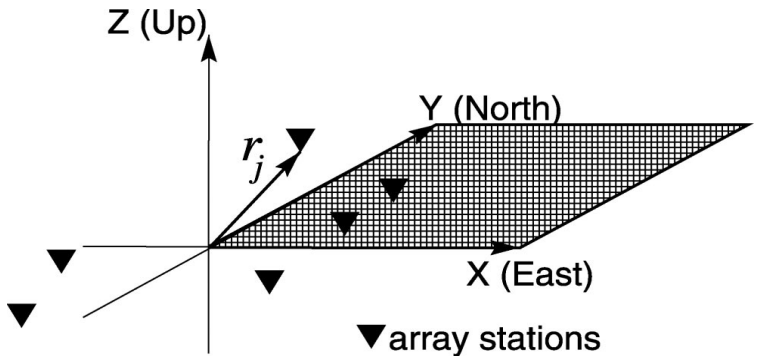

Figure 2.6: The definition of the sensor position vectors $\mathbf{r}_j$. The centre of the array is assumed to be in the centre of the Cartesian coordinate system (from Rost & Thomas, 2002).

For each station *i* at position $\mathbf{r}_i$ (location vector) the recorded time series is:

$$x_i(t) = f(t - \boldsymbol{r}_i \cdot \boldsymbol{u}_{hor}) + n_i(t); \qquad (2.6)$$

with $\mathbf{u}_{hor}$ representing the horizontal slowness vector. A trace, where the time shift is removed, can be calculated by:

$$\hat{x}_i(t) = x_i(t + \boldsymbol{r}_i \cdot \boldsymbol{u}_{hor}) = f(t) + n_i(t + \boldsymbol{r}_i \cdot \boldsymbol{u}_{hor}); \qquad (2.7)$$

The "delay-and-sum" beam trace for an array with M components is then computed by:

$$b(t) = \frac{1}{M}\sum_{i=1}^{M} \hat{x}_i\,(t) = f(t) + \frac{1}{M}\sum_{i=1}^{M} n_i(t + \boldsymbol{r}_i \cdot \boldsymbol{u}_{hor})\,; \qquad (2.8)$$

With uncorrelated noise n_i at the individual stations the time shifted noise terms do not sum up constructively, therefore reducing the noise amplitude by a factor of $\sqrt{M}$ compared to the signal (Rost & Thomas, 2002). As a prerequisite of this beamforming method all slowness vector components of the phase of interest must be known. Necessary assumptions for the beamforming are: the signal must be coherent across the whole array, the signal arrives as a planar wavefront and the noise field is uncorrelated $\sqrt{M}$ (Rost & Thomas, 2009). Thus, the superior signal detection capability of arrays is obtained by applying "beamforming" techniques, which suppress the noise while preserving the signal enhancing the signal to noise ratio (SNR). Examples (for ARCES array) of traces with and without beamforming, respectively, are shown in Fig. 2.7 and Fig. 2.8. Another example is illustrated in Fig. 2.9, in which an event in the Lake Tanganyika region (Tanzania/Burundi) is shown for the GRF array. This shows that the most important step during the summation (or beamforming) process is to find the best delay times, with which the single traces must be shifted before summation ("delay and sum") in order to get the largest amplitudes due to coherent interference of the signals (Schweitzer et al., 2002). The noise suppression is dependent on the number of stations used for the processing.

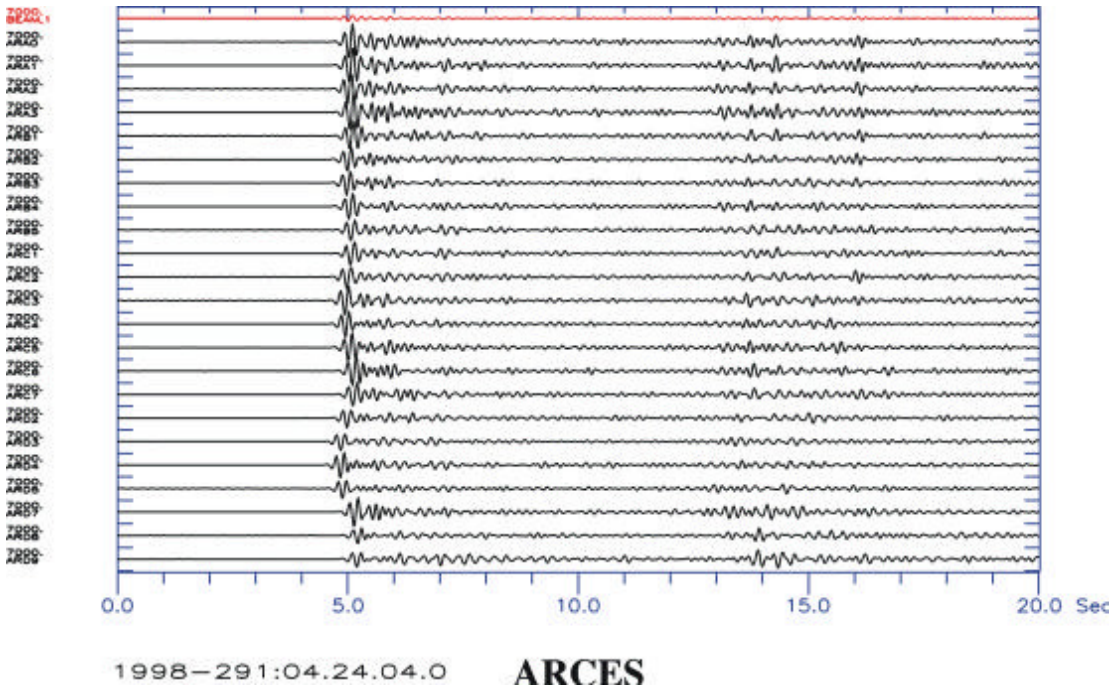

Figure 2.7: The figure show P-phase onsets of a regional event observed with the vertical short-period seismometers of ARCES. The top trace is an array beam, and the remaining traces are single vertical short-period seismograms. All data were filtered with a Butterworth band pass filter between 4 and 8 Hz and are shown with a common amplification. All traces were summed to create a beam without any delay-time application (from Schweitzer et al., 2002).

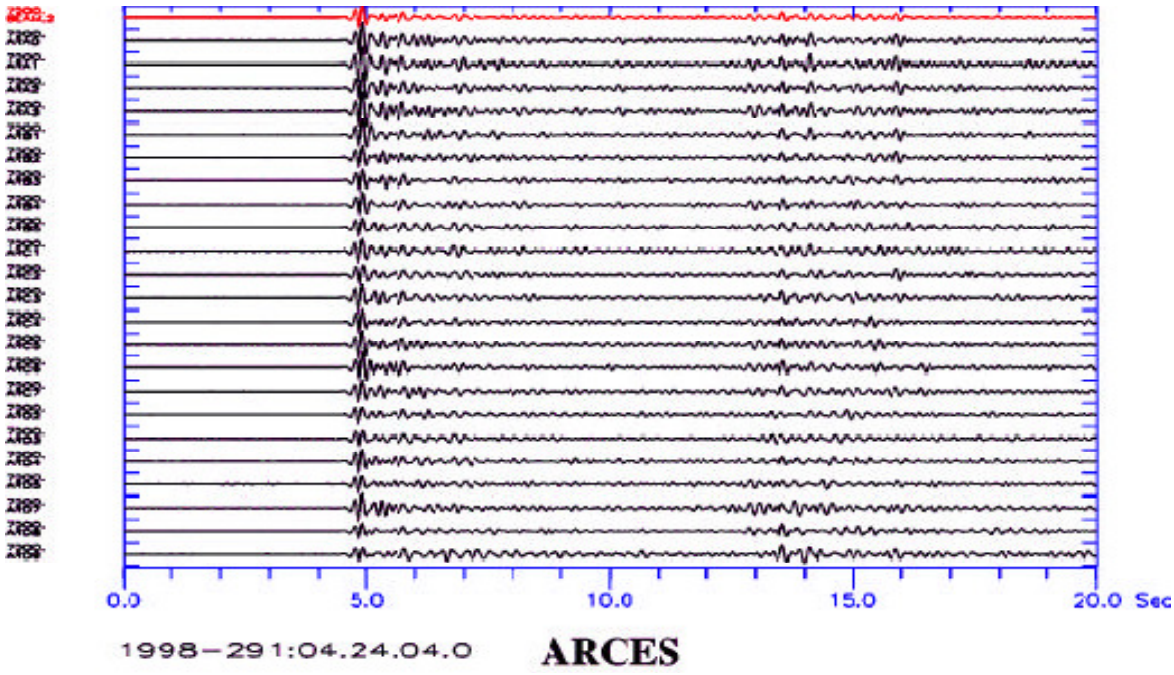

Figure 2.8: This figure shows P-phase onsets of a regional event observed with the vertical short-period seismometers of ARCES as in Fig. X but the single traces were first aligned and then summed. Note for this case the sharp and short pulse form of the first P onset of the beam and the suppression of incoherent energy in the P coda (from Schweitzer et al., 2002).

The calculated time delays assume a homogeneous underground beneath the array, which is not a good approximation for some arrays. Structural inhomogeneities in the array underground influence the travel times to individual stations, therefore leading to additional time differences which have to be taken into account for a successful beam. To this end, array mislocation vectors have been determined for some arrays (Bondar et al., 1999; Krüger & Weber 1992) that allow corrections taking the local structure underneath the array stations into account.

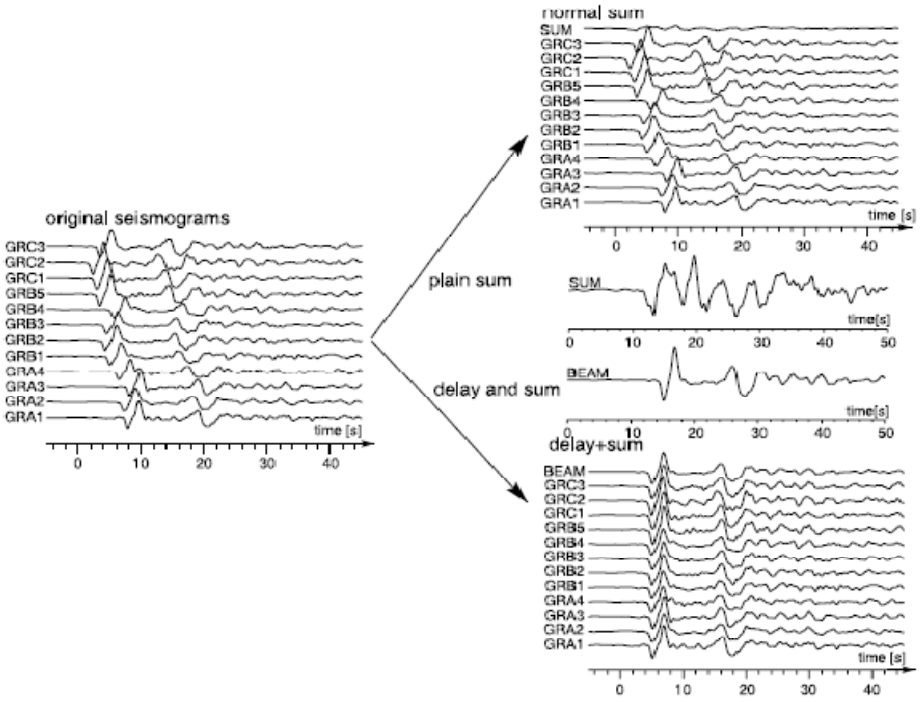

Figure 2.9: Example of the plain sum and "delay and sum" method for an event in the Lake Tanganyika region (Tanzania/Burundi) (2 October 2000 at 0225 UT, depth of 34 km recorded at the Gräfenberg array (GRF) (GRA1 to GRC3). The left-hand side shows the traces as recorded by the array stations. The right-hand plots show the results of (top) a plain sum and (bottom) a delay and sum. High amplitudes and no signal distortion are achieved by the delay and sum method (from Rost & Thomas, 2002).

In conclusion, the beamforming method amplifies the phases with an appropriate slowness, while suppressing incoherent noise and the phases with different slowness. The signal coherency is dependent on wavelength and array aperture, i.e., the signal coherency can rapidly decay if the aperture of the array is too large compared to the wavelength of the signal. If the noise field is correlated (Friedrich et al., 1998) a weighting factor can be applied to the traces prior to summing (Johnson & Dudgeon, 1992) to mitigate the effects of the coherent noise.

2.2.2 Vespagram

As discussed in the last section 2.2.1, the beamforming method enhances the amplitude of a signal with a given slowness u. To determine the unknown horizontal slowness or back-azimuth of an arriving signal the so-called vespa process (VElocity SPectral Analysis; Davies et al., 1971) can be used. vespa

procedure calculates array beams for varying slowness (and constant back-azimuth) but can also be expanded to work with varying back-azimuth (and constant slowness). The vespa in its original form (Davies et al., 1971) estimates the seismic energy arriving at the array for a given back-azimuth and different horizontal slownesses *u*. For applications of vespagram the prerequisite is that all components of the slowness vector of the phase of interest must be known. The method needs just one component of the slowness vector, horizontal slowness or back azimuth, as input. The time offsets recorded at each station of the seismic array depend on the slowness vector of the wave and the position of the station in the array, for a plane wavefront.

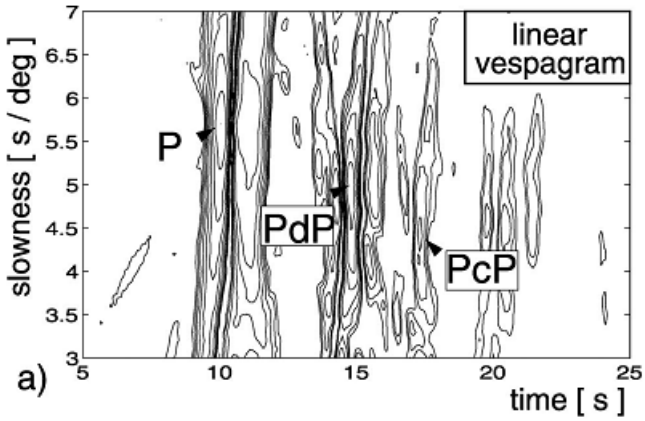

Figure 2.10: Vespagram for the event of 17 December 1991 in the Kurile region. The vespagram shows the energy recorded at the GRF and the German Regional Seismic Network (GRSN) for the theoretical back azimuth over time for varying slowness. The P, PcP, and PdP (reflection of P wave at the D discontinuity in the lowermost mantle) arrivals are marked. PdP and PcP show a slightly smaller slowness than P (Rost & Thomas, 2002).

These time delays are used in the vespa process to specify the slowness or back-azimuth of the wave front, since they provide a direct estimate of the back-azimuth and the slowness of the signal. The vespa combines the capability of beamforming to enhance the signal with the measurement of the slowness or back-azimuth (Rost & Thomas, 2002).

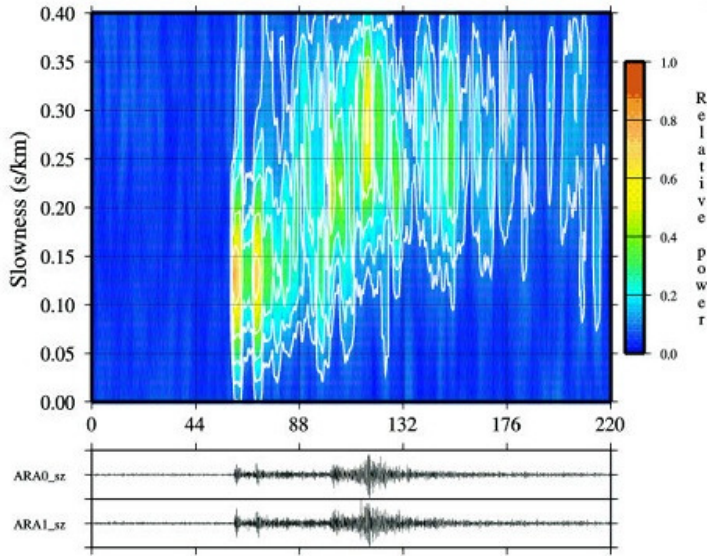

Figure 2.11: Vespagram for a mining explosion (December 21, 1992; 07:10; lat. 67.67°, lon. 33.73°) in the Khibiny Massif observed at ARCES array. Shown is the observed seismic energy for different apparent velocities (slowness) and a constant back-azimuth of 118° (from Schweitzer et al., 2002).

The graphic result of this method is the *vespagram* that is a diagram of the energy content (amplitudes) of the incoming signals as a function of slowness or back azimuth and time (Fig. 2.10 and Fig. 2.11).

2.2.3 Slowness estimation: f-k analysis and Array Response Function

The seismic array method, originally introduced as "f-k analysis" by Capon (1969) has been further developed to include wide-band analysis, maximum-likelihood estimation techniques, and three-component data (Kværna & Doornbos, 1986; Kværna & Ringdal, 1986; Ødegaard et al., 1990). The f-k analysis is used as a reference tool for the complete slowness vector estimation in terms of back-azimuth θ and slowness u. The f-k analysis calculates the power distributed among different slownesses and directions of approach (Capon, 1969; Harjes & Henger, 1973; Aki & Richards, 1980). The determination of slowness and back-azimuth of a signal by f-k analysis consists in a grid search for all u and θ combinations. Every grid point in the f-k space corresponds to a relative time shift between the single seismic traces and the systematic scan of the f-k space can be performed to find the best parameter combination, producing the highest

amplitudes of the summed signal. This computation is performed in the spectral domain to save computation time (Rost & Thomas, 2002). The principle is beamforming in the frequency domain for a number of different slowness values. This method can be used to locate seismic sources (natural earthquakes and/or explosions). Because the f-k analysis is a frequency-domain method, one has to define an interesting frequency range. The following derivation of f-k analysis follows Kelly (1967) and Harjes & Henger (1973). A signal arriving at a reference point within the array with a horizontal velocity v_s and a back-azimuth θ is described as $s(t)$. The nth seismometer with the location vector $\mathbf{r}_n$, relative to the array reference point records the signal:

$$x_n(t) = s(t - \boldsymbol{u}_0 \cdot \boldsymbol{r}_n); \qquad (2.9)$$

$$\boldsymbol{u}_0 = \frac{1}{v_0}(\cos\theta\,, \sin\theta); \qquad (2.10)$$

Where $\mathbf{u}_0$ is the slowness vector and v_0 is the surface velocity. The maximum amplitude of the sum of all array seismometers is reached if the signals of all stations are in phase, that is, if the time shifts $\boldsymbol{u}_0 \cdot \boldsymbol{r}_n$ disappear (beamforming). So, the output for an array of N elements will be:

$$y(t) = \frac{1}{N}\sum_{n=1}^{N} x_n\,(t + u_0 \cdot r_n); \qquad (2.11)$$

For a signal with a different slowness vector $\mathbf{u}$ the beam trace computed with the (9) will be:

$$y(t) = \frac{1}{N}\sum_{n=1}^{N} s\{t + [(\boldsymbol{u}_0 - \boldsymbol{u}) \cdot \boldsymbol{r}_n]\}; \qquad (2.12)$$

The total energy recorded at the array can be calculated by the integration of the squared summed amplitudes over time using Parseval's theorem. The following equation can be obtain:

$$E(\boldsymbol{k}-\boldsymbol{k}_0) = \frac{1}{2\pi}\int_{-\infty}^{+\infty} |S(\omega)|^2\,|A(\boldsymbol{k}-\boldsymbol{k}_0)|^2 d\omega; \qquad (2.13)$$

where

$$|A(\boldsymbol{k}-\boldsymbol{k}_0)|^2 = \left|\frac{1}{N}\sum_{n=1}^{N} e^{(2\pi i(\boldsymbol{k}-\boldsymbol{k}_0)\cdot \boldsymbol{r}_n)}\right|^2; \qquad (2.14)$$

is the Array Response Function, *S(ω)* is the power spectral density and **k** is the wave number vector with

$$\boldsymbol{k} = (k_x, k_y)\omega \cdot \boldsymbol{u} = \frac{\omega}{v_0}(\cos\theta, \sin\theta); \qquad (2.15)$$

and $\mathbf{k}_0$ is the wave number vector for $\mathbf{u}_0$. The final equation (2.14) is the Array Response Function (ARF) and represents the Fourier Transform of the array configuration, the energy absorption of the array as function of the wavenumber.. The ARF is controlled by the design (aperture, configuration, and inter-station spacing) of the array:

- The array aperture determines the resolution of the array for small wavenumbers
- The number of seismic stations (array elements) controls the quality of the array as wavenumber filter
- The inter-station distances define the position of the side lobes in the array transfer function

- The geometry of the array defines the azimuth dependence of the former items

When designing an array a detailed knowledge of the geology and lateral heterogeneities have to be included in the planning phase. The array underground should be as homogeneous as possible, and the station sites should be installed at similar altitudes. A station elevation correction must be considered if the time shift caused by the altitude differences amounts to approximately 1/2 of the time delay between two samples (Braun et al., 2004). The result of the f-k analysis is the power spectral density as a function of the slowness and the back-azimuth. The slowness can be calculated from the wave number vector **k** = (k_x, k_y) and u_s as the apparent horizontal slowness.

The power spectral density is displayed in a polar coordinate system called the f-k diagram. In the f-k diagram the back-azimuth is plotted on the azimuthal axis, and the slowness is plotted on the radial axis (see Figure 2.13).

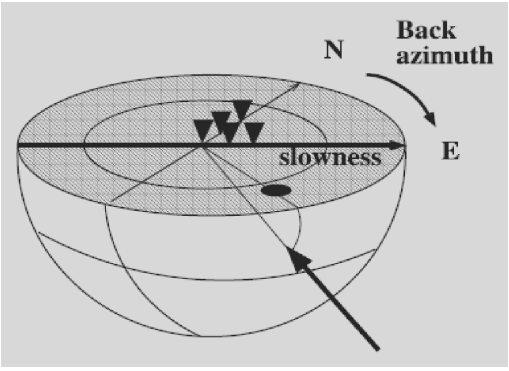

Figure 2.12: Explanation of the f-k diagram. An incident wave travels through an imaginary half sphere beneath the array at point (X). The half sphere is projected to the surface in the f-k diagram. The distance of the maximum energy from the origin gives the slowness; the angle from north gives the back azimuth (from Rost & Thomas, 2002).

Figure 2.14a shows the ARF of the small-aperture Yellowknife array (YKA) computed for a theoretical monochromatic wave with a frequency of 1 Hz. For comparison, the ARF of the German Gräfenberg array is shown in Figure 2.15a. Its larger aperture of 50 by 100 km and the different configuration result in a much better resolution for slowness and back-azimuth than for the small-aperture Yellowknife array. The f-k analysis can only be applied to short time windows with a duration of some seconds. Large time windows may contain several different phases with different slowness vectors, which make the unambiguous identification of a phase impossible. This implies that the f-k analysis is best carried out using arrays for which the delay times of the arriving signal at all stations are small.

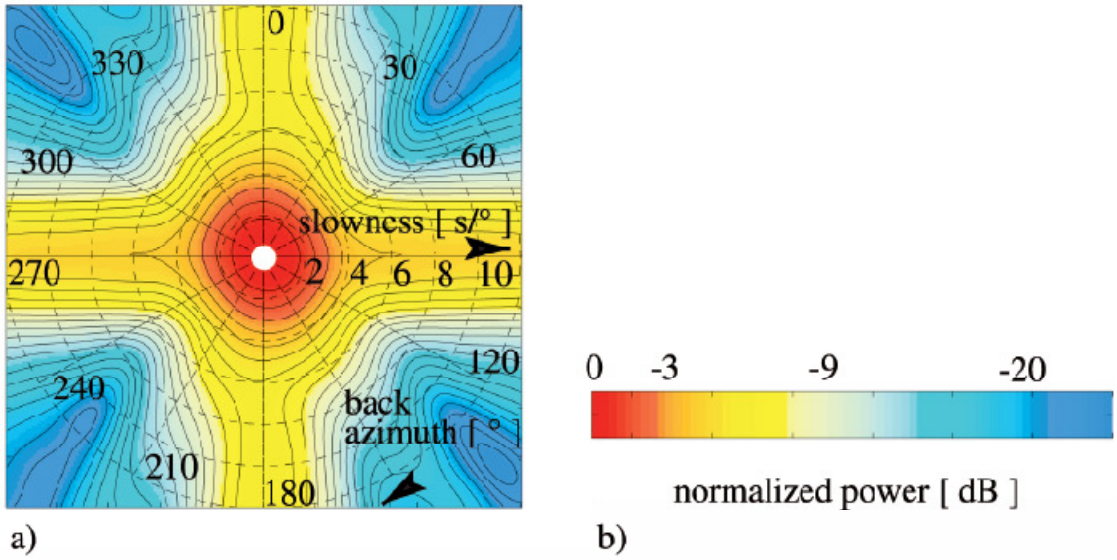

Figure 2.13: Array response function of the small aperture Yellowknife array (YKA) computed for 1-Hz data. The logarithmic power spectral density is colour-coded, and the maximum is normalized to 0 dB. The 1-dB isolines are added. The maximum power density is normalized to 0 dB (red). The slowness from 0 to 12 s/deg with 2 s/deg per tick is displayed on the radial axis; the back azimuth is shown clockwise from 0° to 360°. The slowness and back-azimuth of the maximum power is marked by the white circle. (b) Power colour scale for all f-k diagrams (from Rost & Thomas, 2002).

This disadvantage can be avoided by careful selection of the time windows studied. As with most other array methods, the f-k analysis assumes a plane wave front arriving at the array, small heterogeneities beneath the receivers can alter the wave front and destroy the coherency of the signals. This may change the results of the f-k analysis (Rost & Thomas, 2002).

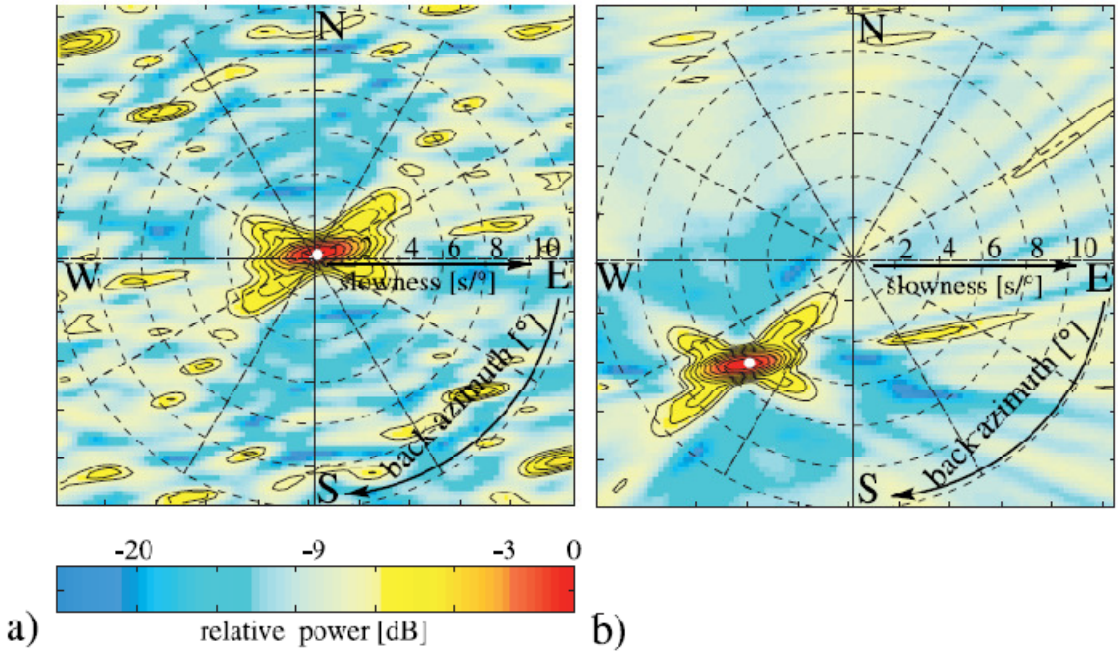

Figure 2.14: (a) ARF of GRF-array. Owing to the larger aperture the resolution is higher than that of YKA (Figure 13a). (b) The f-k analysis of a wave arriving with a slowness of 7.75 s/deg and along a back azimuth of 225° (from Rost & Thomas, 2002).

Examples of f-k analysis performed by a small aperture array installation in Central Italy is shown for the CDC-array in Figure 2.16 and 2.17. Here the array data were processed using the broadband f-k algorithm of Kværna & Dornboos (1986), which represents an extension of the original single frequency wave number analysis of Capon (1969). Broadband f-k analysis uses a band-pass filtered signal as input, that can be interpreted as the stack of several monochromatic f-k results. For a correct application of f-k analysis of the analysed wavefield, it is fundamental that the array geometry guarantees a correct spatial sampling of the coherent part of the band-pass filtered signal.

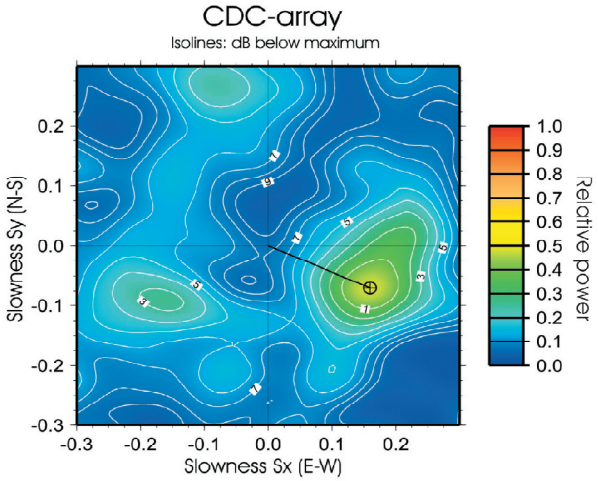

Figure 2.15: f-k analysis based on the nine band-pass filtered (2.0-6.0 Hz) vertical traces of a local seismic event (*ML*=1.8) occurred at 40 km ESE from the CDC-array. The maximum peak level (relative power 0.48) is found for v_{app}=5.74 km/s and back-azimuth of 113.7°) from Braun et al. (2004).

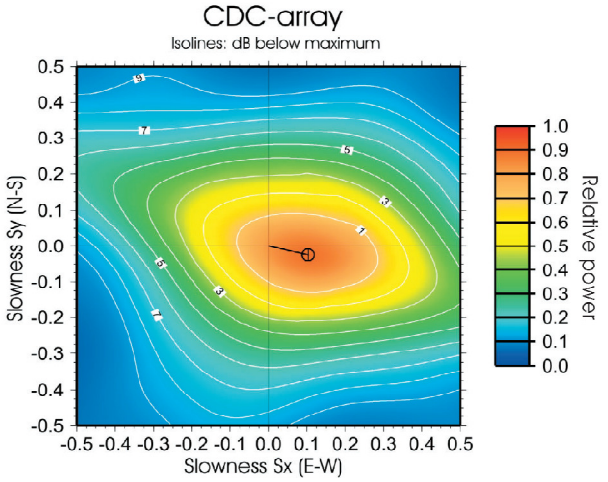

B

Figure 2.16: analysis of the nine band-pass filtered (0.8-2.5 Hz) vertical records of a regional seismic event (*ML*= =3.5), located in the Greece-Albania border region. For the maximum peak level (relative power 0.88) an apparent velocity of v_{app}=9.43 km/s was determined, reaching the array from a back-azimuth of 103.3° (from Braun et al., 2004).

CHAPTER 3

Source-Scanning Algorithm

The following section deals with the Source-Scanning Algorithm, an unconventional approach to recover the distribution and the sequence of seismic sources exploiting waveform information from a seismic array, by systematically searching through a range of trial source locations and origin times.

3.1 Introduction

The determination of hypocentral parameters of a seismic source is commonly achieved by minimizing the difference between observed and predicted arrival times of various phases at a number of stations and is possibly refined, for specific cases, through relative locations using travel-time differences between pairs of events (e.g. Waldhauser & Ellsworth, 2000) or stations (e.g. Zhou, 1994). However, in presence of closely spread events in space and time the high level of background noise can hamper phase identification and correlation with the proper source. Inversion of seismic waveforms can in principle provide better estimates of source distribution in space and time, but its application to small-scale studies is limited by the ability to calculate accurate short-wavelength seismograms and by the often required a priori knowledge about the focal mechanism and dimension of the fault. An unconventional approach to identify the distribution of seismic sources which does not require either to pick arrival times of seismic phases accurately (or to calculate synthetic seismograms), is to back project the seismic energy into the source region by stacking the seismograms recorded at an array of seismic stations according to the relative time shift of each station-to-possible-source-location. Recently, algorithms have been developed to account for curved wave fronts. This allows to analyze also seismic events where the epicentral distance is not much larger than the array aperture (the plane wave approach is not valid for epicentral distances that amount to less than approximately ten times the array aperture). One of the first

applications was done by Spudich & Cranswick (1984), who observed with an accelerometer array the rupture propagation during the 1979 Imperial Valley earthquake (California). Other studies followed (e.g. Huang, 2001; Kao & Shan, 2004; Krüger & Ohrnberger, 2005; among the others), which are all based in principle on a curved wavefront stacking scheme. The principle is to grid the assumed seismic source region appropriately and to calculate the theoretical travel-times from each single grid point to every single station. The seismic traces are shifted relatively according to the theoretical travel-times and the seismic energy of the stacked traces is stored for each grid cell. In this way the seismic traces sum up constructively for the area of instantaneous energy radiation. Repeating the procedure for subsequent time windows (named time-slices) the possible migration of the source location can be evidenced. The Source-Scanning Algorithm (Kao & Shan, 2004) is one of the methods based on this approach. Two applications of SSA are considered here. A 2D example of a large earthquake study, where the source to locate is intended in terms of the rupture front propagation during the M_w = 9.3 Sumatra earthquake (December 26, 2004). The 3D small-scale application described in detail in Chapter 4 and Chapter 5, with the specific implementation of a modified SSA, aimed at locating the sources of scattering in the crust.

3.2 The Source-Scanning-Algorithm

Kao & Shan (2004) have introduced a seismic array method to represent the distribution of seismic sources in space and time without any *a priori* knowledge of the orientation or geometry of the actual fault plane. This method, named the Source-Scanning Algorithm (SSA), exploits waveform information, including both relative amplitudes and arrival times, from an array of seismic stations, to determine whether or not a seismic source is present at a particular time and location. By systematically scanning through a range of trial source locations and origin times, they are able to recover the entire distribution and sequence of seismic sources without the need either to pick arrival times of seismic phases

accurately or to calculate synthetic seismograms. A further merit of SSA is that it can take full advantage of a known (and presumably more accurate) 3-D velocity model, reducing the effect of lateral velocity heterogeneity (Kao & Shan, 2004). The SSA method identifies the existence of seismic sources in space and time by calculating the so-called "brightness" function for all grid points inside the model space. The larger the value of the brightness function, the better the consistency between the identified sources (that is, epicentre, depth and origin time) and observed waveforms. The SSA has been used to locate the tremors in Cascadia region (Kao et al., 2005; Kao et al., 2006) or to identification of earthquake rupture plane (Kao & Shan, 2007). Assuming a seismic event recorded by a seismic array of N stations, the first step is the amplitude normalization followed by the calculation of the "brightness" of a point η at a specific time τ:

$$br(\eta,\tau) = \frac{1}{N}\sum_{n=1}^{N}\left|u_n(\tau + t_{\eta n})\right|; \qquad (3.1)$$

where u_n is the normalized seismogram recorded at station n, $t_{\eta n}$ is the predicted travel-time from point η to station n of a particular phase with the largest observed amplitude (on a regional scale, this means the S phase). If all the largest amplitudes originated from a source at point η and time τ , then $br(\eta, \tau) = 1$ (Fig. 3.1). Likewise, $br(\eta, \tau) = 0.1$ means that a hypothetical seismic source at point η and time τ would generate only about 10% of the largest observed amplitude at each station. By systematically searching through all η and τ for the local maxima of the brightness function, effectively there will be the reconstruction of the spatial and temporal distribution of the seismic sources. In practice however, due to an imperfect knowledge of the velocity model, the predicted arrival time of the largest amplitude at each station may be slightly different from that observed.

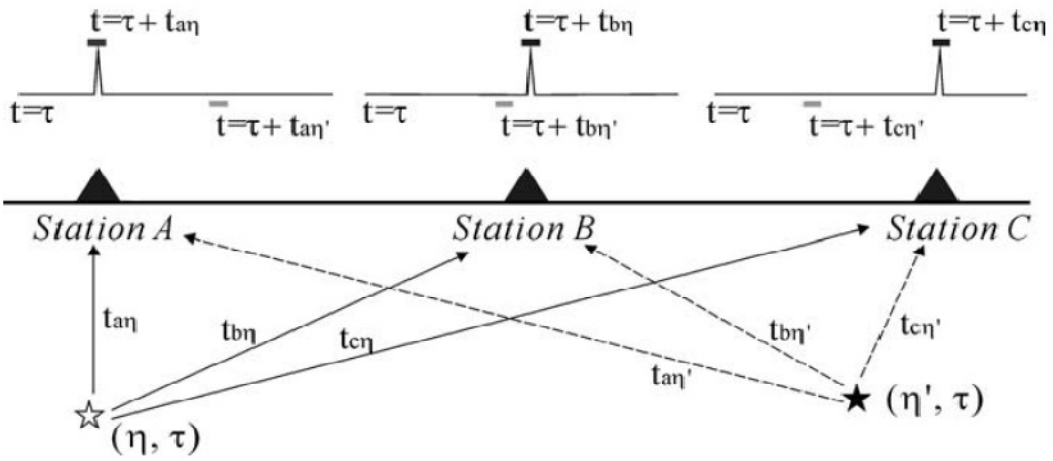

Figure 3.1: A schematic diagram to illustrate the concept of SSA. The "brightness" of a point η at time τ is calculated by summing the normalized amplitudes from all stations at the predicted arrival times (i.e. τ plus the respective travel-times $t_{a\eta}$, $t_{b\eta}$, and $t_{c\eta}$, as marked by the solid short bars). A bright spot (white star) is found if its location and time are consistent with the arrival of the largest amplitude at each station. A point without any seismic source (η', τ) will have little brightness (black star) due to the lack of amplitude at the predicted arrival times ($\tau + t_{a\eta'}$, $t_{b\eta'}$, and $t_{c\eta'}$, as marked by the grey short bars); from Kao & Shan (2004).

Therefore, instead of using only the amplitude at the predicted arrival time, that is, $u_n(\tau + t_{\eta n})$ the equation (3.9) can be modified to include a contribution from surrounding points within a chosen time window, thus:

$$br(\eta,\tau) = \frac{1}{N}\sum_{n=1}^{N}\left\{\frac{\sum_{m=-M}^{M} W_m \left|u_n(\tau + t_{\eta n} + m\delta t)\right|}{\sum_{m=-M}^{M} W_m}\right\}; \qquad (3.2)$$

where M is the number of points within the time window centred around the predicted arrival time, δt is the sampling interval, and W_m is a weighting factor which varies according to how far the arrival time of the energy departs from the predicted arrival time.

3.3 A 2D Application: Source Tracking of the 2004 Sumatra Earthquake by Using Italian Network

A MatLab (http://www.mathworks.com/products/matlab/) language code has been written based on the formulas by Kao and Shan (2004), in order to test the

SSA algorithm. As seismic broadband data the Dec. 26, 2004 M_w = 9.3 Sumatra earthquake has been chosen, as recorded by the 25 stations of the Italian Broadband Seismic Network (ISBN) (Figure 3.2a). The scope of this analysis is to study the space-temporal evolution of the P-wave energy radiated during the 2004 Sumatra earthquake. With an area of 1100x500 km^2, the aperture of the ISBN is of comparable dimension as the GRSN. The epicentral distance towards the source region amounts to about eight times the array aperture. Therefore the plane wavefront assumption cannot be applied. For this purpose a Source Scanning Algorithm (SSA) was developed, similar to the one proposed by Kao & Shan (2004) and further applied by Krüger & Ohrnberger (2005). The Sumatra source area (Latitude min-max 0°-20°; Longitude min-max 85°-105°) was first gridded into latitude and longitude intervals of 0.2° and then for each grid point the theoretical P-wave travel-time to each of the 25 recording stations was calculated, using the ak135 model (Kennet et al., 1995). For each grid cell, one-minute long seismogram segments were stacked with respect to station CERT (geometrical centre of ISBN, black-star in Fig. 3.2a), after having shifted the single traces according to their pre-computed theoretical travel-times. Thereafter the procedure was repeated for the estimated rupture duration of 450 s shifting the reference trace in steps by 5 s.

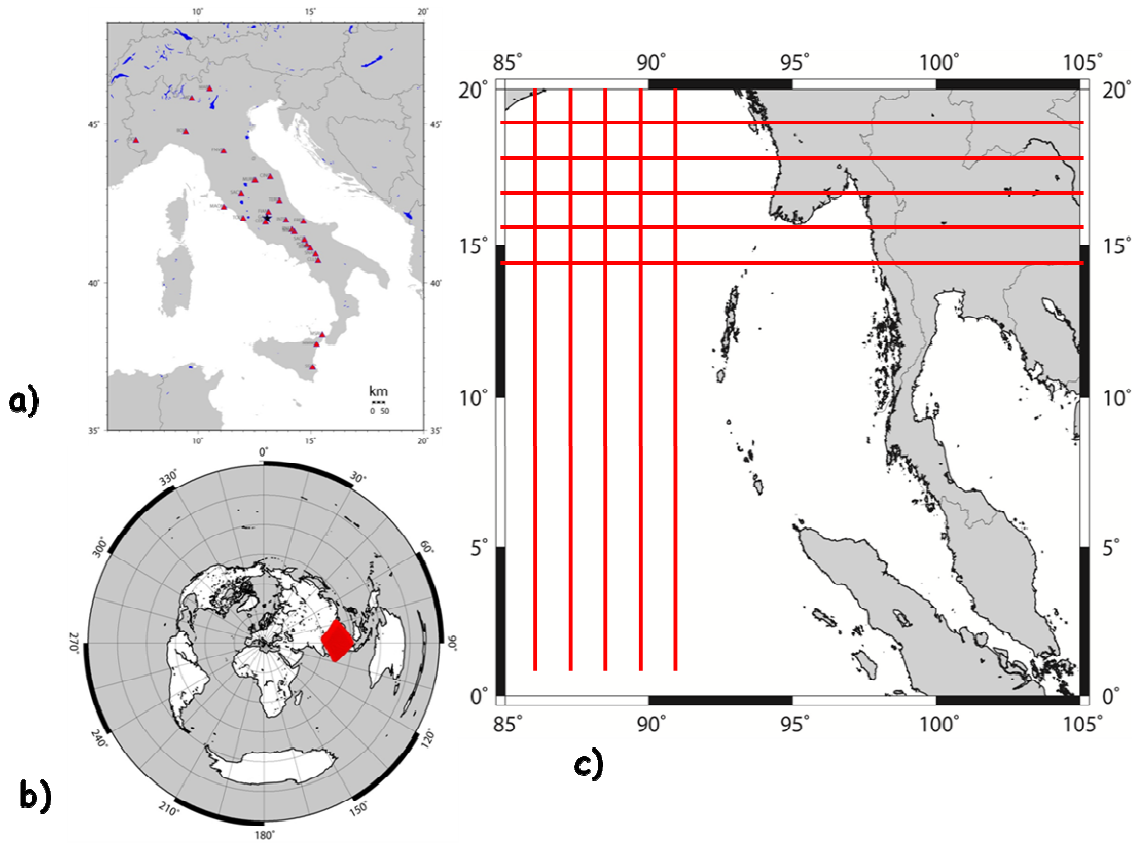

Figure 3.2: a) Location map of Italy with part of ISBN receivers constituting the broad-band Italian seismic. The red triangles represent the receivers that have recorded the Sumatra M_w: 9.3 event. The black-star is CERT receiver that is the geometrical centre of array; b) Polar projection with CERT located in the centre. The red zone shows the grid area used for the grid search; c) Location map of Sumatra study region in which the red lines summarize the 10201 cells that correspond to the red zone in c)

The analysis has been applied to only one depth fixed at 25 km. The receivers that have recorded the event and have been considered to form an array have been 25, 10201 grid cells and 90 time shifts. Following Krüger & Ohrnberger (2005) the resulting beam trace was squared and integrated in order to assign to each grid point a representative value for the source strength.

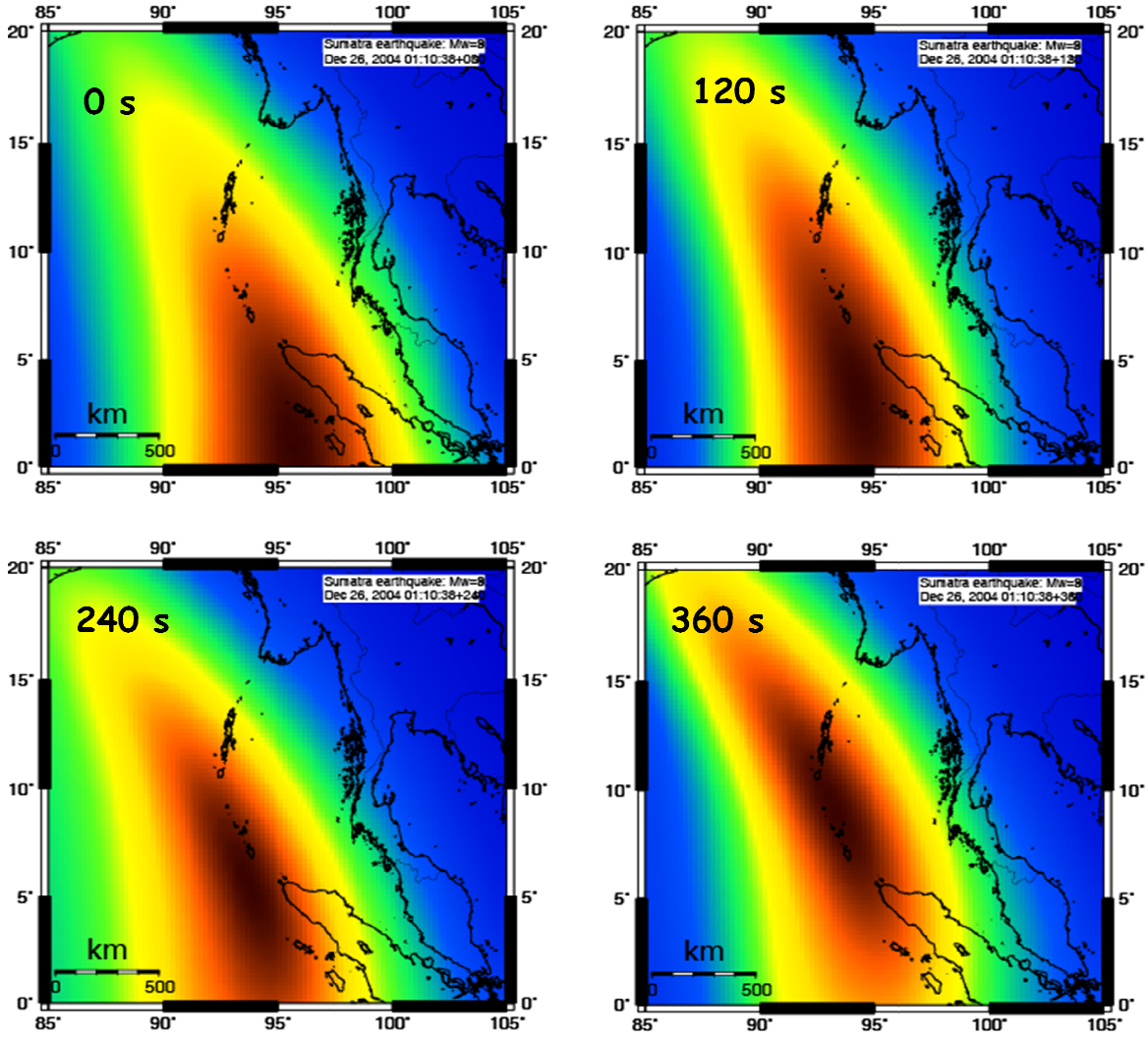

Figure 3.3: Location maps of Sumatra study area in four different times(in the left top for each map: 0s, 120s, 240, 360s) in which can be observed the evolution of seismic energy, then the rupture front propagation in the time.

Figure 3.3 shows the image of the seismic energy radiation for each grid cell, frozen at time windows of 0s, 120s, 240s and 360s. A clear shift of the seismic energy maximum from south to north can be observed, that amounts to ≈ 1000 km in 6 min, corresponding to a mean rupture velocity of 2.75 km/s. This result is in accordance to values reported by Ishii et al. (2005) and Krüger & Ohrnberger (2005).

CHAPTER 4

Methodology

This chapter provides theoretical explanations about the Double Beam Method (DBM), in particular the theory, the computer code highlighting the improvements with respect to previous works. The implementation of the DBM into the CAP-code (Continuous Array Processing) is explained by applying the method for the study of crustal scatterers.

4.1 Fundamentals of the Double Beam Method

The Double Beam Method (DBM) is one of the possible double array stacking techniques (Revenaugh & Mendoza, 1996; Reasoner & Revenaugh, 1999; Kito & Krüger, 2001; Krüger et al., 1993; Krüger et al., 1996) available to investigate the crustal and mantle structure by means of array seismology. Previous DBM applications have been performed for different investigation scales: regional for the upper crust (Rietbrock & Scherbaum, 1999) and, on a global scale, for the study of mantle and core-mantle discontinuity (Krüger et al., 1993; Scherbaum et al., 1997; Krüger et al., 2001, etc etc...). The *Double Beam* technique is still not a common tool in seismology. However, in the present thesis this methodology was applied using the opportune implementations for the proper claims. The DBM provides images of spatially distributed heterogeneities using information from combinations of source- and receiver-arrays (Scherbaum et al., 1997). The DBM is based on the principle of Green's function reciprocity, for which the source and receiver positions in a seismic experiment can be exchanged without affecting the observed seismogram (Niazi, 1969; Spudich & Bostwick, 1987; Scherbaum et al., 1991). With respect to a single array analysis, a combination of source and receiver arrays leads to a further improvement of the signal-to-noise ratio (SNR) due to the summation of a higher number of individual recordings and to the different suppressing properties in the source- and in the receiver-

array. The technique used in this work is based on the DBM devised by Krüger et al. (1993, 1996). The objective is to locate the seismic crustal scatterers in terms of depth and travel-times. The DBM determines and uses the information about the direction of a wavelet leaving the source-array together with the information about the direction of the same wavelet arriving at the receiver-array to identify the travel path of the corresponding phase and to locate the corresponding scattering points (Rietbrock & Scherbaum, 1999). In Fig. 4.1 both, the standard receiver-array geometry, as well as the reverse configuration, the source-array geometry, is shown.

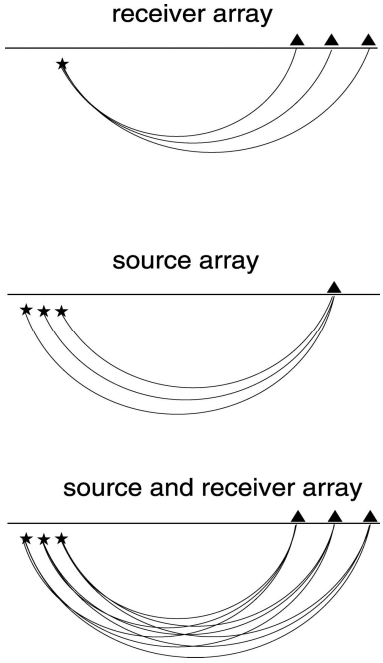

Figure 4.1: Principle of DBM. Stars denote the sources; triangles are the receivers. Compared to a single beam, the region where the rays turn is much better sampled by the DBM (from Rost & Thomas, 2002).

In the following, the concept of DBM for a small-scale crustal application is illustrated in detail. The main difference between a large-scale (mantle/core) and a small-scale (crust) approach is to consider either a plane or spherical wave-front. In the first case, the conventional array seismology techniques (cv. Chapter 2) can be applied; in the second case not. The receiver array is situated too close to the earthquake sources and the diffractors or scattering points are situated

even closer to receiver and source array). The only small-scale case studied in literature was published by Rietbrock & Scherbaum (1999), which will shortly be revisited in the following to better illustrate the DBM concept. Fig. 4.2a shows the cross-section relative to the recording geometry for an experiment with a source-array, constituted by four hypothetical sources (S_1, S_2, S_3, S_4) , three receivers (r_1, r_2, r_3), which setup the receiver-array, and a hypothetical diffractor D.

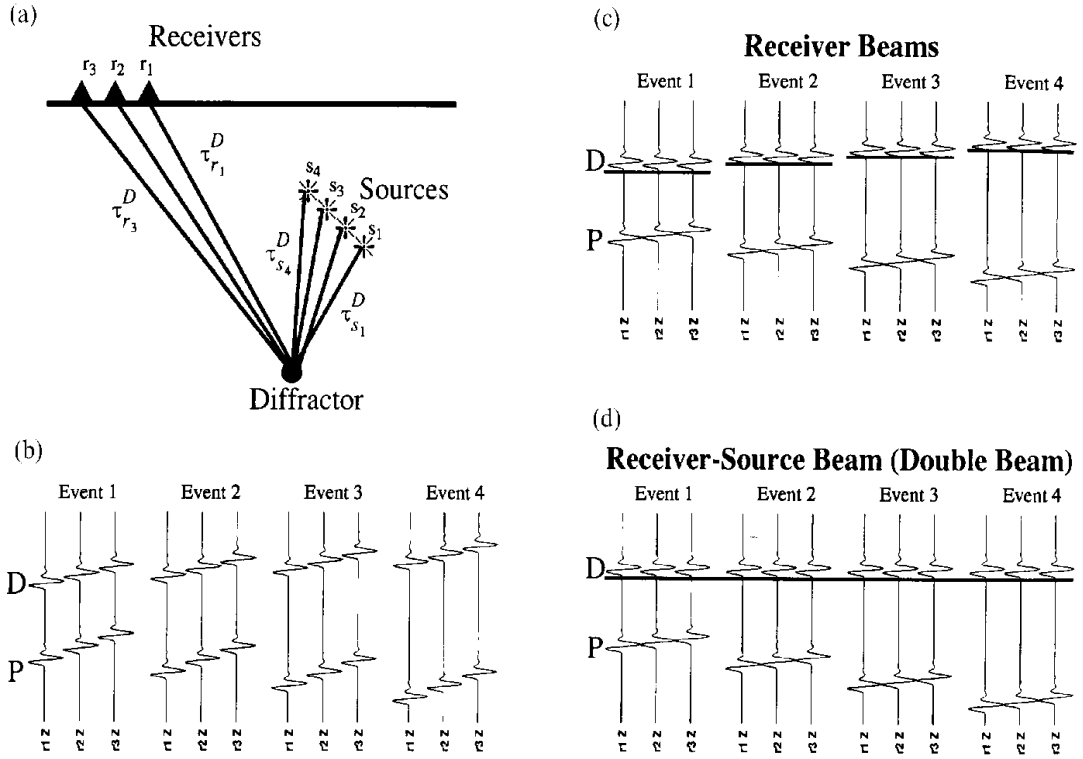

Figure 4.2: (a) Cross-section of the DBM recording geometry; (b) The recorded waveforms corresponding to the cross-section (a); (c) The alignment in conventional receiver beams, whereas in (d) the alignment in the DBM is shown. P indicates the direct wave and D the diffracted one (from Rietbrock & Scherbaum, 1999).

The first arrival represents the direct *P* wave, labeled P. A second arrival D is due to scattering from the diffractor at depth. The travel-time (τ) for this later arrival depends on the source-receiver geometry and the position of the diffractor and is given by the travel time from the source to the diffractor plus the time from the diffractor to the receiver. The DBM in Rietbrock & Scherbaum (1999) requires further to specify a target phase D to compute the theoretical move-out for a

certain Earth model in the receiver- or source-array. Aligning the traces in individual receiver beams according to the slowness of the phase D leads to Fig. 4.2c whereas the final alignment in the DBM is shown in Fig. 4.2d. Conventional receiver beam stacking configuration leads to an enhancement of the *D* phase, but the direct *P* phase is still quite clearly visible (Fig. 4.2c). Using the DBM, the *D* phase becomes more amplified due to the higher number of traces lined up in the stacking process (Fig. 4.2d), while the direct *P* phase becomes even further suppressed (Fig. 4.2d), because the slowness in the receiver array and source array differ from the investigated *D* phase slowness. Phases with nearly identical slownesses in the receiver array can therefore be separated by their slowness difference in the source array (Rietbrock & Scherbaum, 1999). Subsequently, in order to compute the double beams, the source-array and receiver-array beams are calculated. The final result is given by both contributions added over all the sources and receivers used. The procedure to compute the beams of receivers has already been outlined in paragraph 2.2.1 (Beamforming). The following paragraph deals with source array and Double Beam forming. The concept of combining clusters of sources in source arrays has been known since a long time (Niazi, 1969). According to the Green's functions reciprocity theorem, the recordings of several seismic sources by a single instrument can be used in the same way as several recordings of a single source (Spudich & Bostwick, 1987; Scherbaum et al., 1991). The accuracy of the results (i.e. the improvement of the SNR) depends, to a great extent, on the quality of the available information about the sources, such as location, origin times and source mechanism (Rost & Thomas, 2009). Source arrays are indeed rarely used in global seismology due to imprecisely known source parameters, except for arrays of nuclear explosions (Goldstein et al., 1992) with well known hypocentral parameters and simple and similar source mechanisms. Scherbaum et al. (1991) have showed, through analysis of micro-earthquakes clusters, that it is possible to separate direct phases from phases that are reflected at the Moho due to their different slowness properties in the source-arrays. Using earthquakes for source-array stacks

requires different normalizations for the source mechanism and the source depth. For example, to overcome some of these problems, static origin time corrections can be applied to each seismogram (Krüger et al., 1996). Static corrections assume that the waves approaching the source-array propagate along great circle paths with a slowness u and add an additional time shift according to this slowness u. The source beamforming is then performed relative to u, providing only relative slowness and back-azimuth information of phases (Krüger et al., 1996; Thomas et al., 2002). In analogy to the coherency requirement for the wave field in receiver-array studies, the waveforms must be similar. In general, this requirement can be fulfilled by a source normalization method, such as a deconvolution with the source wavelet (Oldenburg, 1981). An advantage of source arrays is the identical response of the recording instrument and the same subsurface beneath the station. A disadvantage, however, is that multiples from upper mantle discontinuities and other near-receiver structures are enhanced. Following Rost & Thomas (2002) the main mathematical concepts of source and receiver array-beams will be shortly outlined. The source-array beam $S_i(\boldsymbol{u};t)$ for an arbitrary slowness vector $\mathbf{u}$ is given by:

$$S_i(\boldsymbol{u},t) = \frac{1}{K}\sum_{k=1}^{K} a_k(t) * x_{ik}(t-\kappa_k); \qquad (4.1)$$

where K is the number of the sources, $a_k(t)$ is the source equalization factor to normalize the wavelets of different sources by convolution, $*$ is the convolution operator and x_{ik} is the seismogram of source k at station i. The form of equation (4.1) is similar to (2.6); the time delays are calculated by $\kappa_k = (\boldsymbol{r}_k - \boldsymbol{r}_0)\boldsymbol{u}$ and $(\boldsymbol{r}_k - \boldsymbol{r}_0)$ describes the relative position of the event in the source-array relative to a reference point $\boldsymbol{r}_0$ or the location of a master event. The time delays κ may contain corrections for depth differences or source medium differences between events. From equation (2.7) the receiver-array beam with N seismic stations can be written as:

$$R_K(\boldsymbol{u}_r, t) = \frac{1}{N}\sum_{i=1}^{N} x_{ik}(t + \boldsymbol{r}_i \boldsymbol{u}_r); \qquad (4.2)$$

where $x_{ik}(t)$ is the seismogram of source s_k recorded at station $\boldsymbol{r}_i$ and $\mathbf{u}_r$ a given slowness vector. From equation (4.1) the source-array beam for K sources is calculated by

$$S_i(\boldsymbol{u}_s, t) = \frac{1}{K}\sum_{k=1}^{K} a_k\,(t) * x_{ik}(t - \kappa_k); \qquad (4.3)$$

where $x_{ik}(t)s_k$the time-delays between the sources are calculated by $\kappa_k = (\boldsymbol{s}_k - \boldsymbol{s}_0)\boldsymbol{u}_s$ for a given slowness $\boldsymbol{u}_s$. The source- and receiver-array configurations can be integrated to construct double beams. In the first step, the source time delays $\kappa_k = (\boldsymbol{s}_k - \boldsymbol{s}_0)\boldsymbol{u}_s$ are computed for a certain source slowness vector $\boldsymbol{u}_s$ and for each station i of the receiver array the traces are delayed with κ_k and summed to form a source-array beam $S_i(\boldsymbol{v}, t)$ for a single phase with slowness $\boldsymbol{u}_s$. In a second step the time delays $\tau_i = (\boldsymbol{r}_i - \boldsymbol{r}_0)\boldsymbol{u}_r$ are calculated for each station i in the receiver-array for a receiver slowness $\boldsymbol{u}_r$. The source-array beams S_i are then delayed with τ_i and summed to form the double beam:

$$D(\boldsymbol{u}_r, \boldsymbol{u}_s, t) = \frac{1}{I}\sum_{i=1}^{I} S_i\,(\boldsymbol{u}_s, t - \tau_i); \qquad (4.4)$$

As a special property, the DBM provides slowness information in the source region and at a distant array, simultaneously (Scherbaum et al., 1997). By steering the source- and receiver-array to selected target vectors $\mathbf{u}_s$ and $\mathbf{u}_r$, it is possible to determine the slowness and back-azimuth of wavelets at the receiver-array in addition to their slowness and azimuth in the source region. The enhancement

factor of the DBM in comparison to a receiver array is larger by a factor proportional to $\sqrt{(k)}$, with k as the number of sources used for the source beam forming, shown in equation 4.1 (Krüger et al., 1996). Since the DBM is a combined source and receiver slant stack, the problems of the individual methods transfer to the DBM.

4.2 Application of DBM to a small-scale crustal study

The objective of the DBM application is to image the crustal scattering structure using micro-earthquakes recorded at a close-by array of stations in analogy to the study by Rietbrock & Scherbaum (1999). Back to the example of the configuration sketched in Fig. 4.2, the seismograms recorded from the array of stations located at the surface is shown in Fig. 4.3, where the first arrival is the direct P wave (labelled P) and a second arrival is a phase (labelled PX) generated from the scattering of the buried diffractor D.

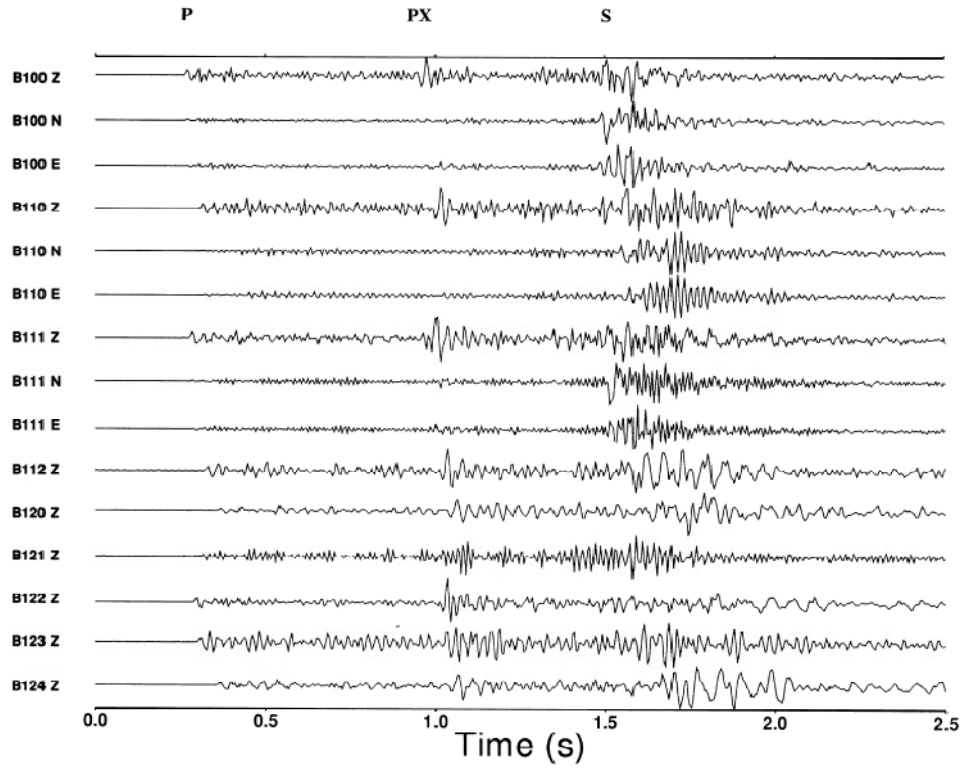

Figure 4.3: The N, E and Z components of seismograms recorded at array named B100 used by Rietbrock & Scherbaum (1999); P, PX an S are the labelled phases used.

Considering the small scale geometry of the configuration, instead of the standard plane wave approach, the travel-times are computed for each event-scatterer-station combination on a grid of possible diffractor points. Thus the travel-times are computed from the source *k* to a particular diffractor point D(x,y,z) and from there to the receiver *i*. Traces are shifted by the computed travel-time differences in order to align each individual trace according to the individual travel path $\tau_{ki}^{D(x,y,z)} = \tau_k^{D(x,y,z)} + \tau_i^{D(x,y,z)}$. For the total number I_k of recorded seismograms x_{ki} (of event *k*), the power in the receiver beam (RBP) for the time window T and the possible scatterer location (x,y,z) is given by:

$$RBP(x,y,z)_k = \frac{1}{T}\sum_{t=-T/2}^{T/2}\left\{\frac{1}{I_k}\sum_{i=1}^{I_k} x_{ki}\left(t+\tau_{ki}^{D(x,y,z)}\right)\right\}^2 ; \qquad (4.5)$$

with *t* representing the discrete lapse time (with respect to the origin time of the event) evaluated at multiples of the sampling interval. For the source beam the power (SBP) will be:

$$SBP(x,y,z)_i = \frac{1}{T}\sum_{t=-T/2}^{T/2}\left\{\frac{1}{K_i}\sum_{k=1}^{K_i} x_{ki}\left(t+\tau_{ki}^{D(x,y,z)}\right)\right\}^2 ; \qquad (4.6)$$

where K_i describes the total number of sources observed at the receiver *i*. Using the double beam configuration the total power (DBP) for the possible diffractor point D at the point (x,y,z) is given by:

$$DBP(x,y,z) = \frac{1}{T}\sum_{t=-T/2}^{T/2}\left\{\frac{1}{N}\sum_{n=1}^{N} x_n\left(t+\tau_n^{D(x,y,z)}\right)\right\}^2 ; \qquad (4.7)$$

where N is the total number of seismograms observed from the events at the receivers. τ_n corresponds to travel-time for the whole source-diffractor-receiver path for the *n*th seismogram. This allows the detection of phases with small amplitudes that are coherent in the whole double beam configuration. In most cases the local site structure beneath the receivers can distort the incoming wavefront inside the small array installations and can affect the absolute travel-times, causing differences as large as 20-30 m, or even higher, as indicated by static corrections calculated in reflection experiments (Martini & Stiller, 1992). Relative beamforming can be used to correct these effects. Under relative beamforming, all traces are shifted such that a known reference phase (for example the direct P phase) aligns at its theoretical arrival time at each station. The resulting DBP_{ref} (x, y, z) therefore describes the scattering ellipsoid with respect to the ray path of the reference phase:

$$DBP_{ref}(x,y,z) = \frac{1}{T}\sum_{t=-T/2}^{T/2}\left\{\frac{1}{N}\sum_{n=1}^{N} x_n\left(t + \tau_n^{D(x,y,z)} + \tau_n^0\right)\right\}^2 ; \qquad (4.8)$$

τ_n^0 is the difference between the observed and the theoretical onset time of the reference phase. The previously described procedure is the same used for a normal DBM if the computation of the travel-times τ^D is changed to a plane-wave approach.

4.3 Implementations

The implementation of the DBM here presented is constituted by a further development of both SSA (see Chapter 3 for details) of Kao & Shan (2004) and the crustal study of Rietbrock & Scherbaum (1999) approach. For this purpose the original SSA (Kao & Shan, 2004), which exploits waveform information (absolute amplitudes and arrival times) from a seismic array by systematically scanning through a range of source locations and origin times, has been slightly modified.

Applying the DBM concept as amplitude-dependent measure of waveforms coherency the mathematical quantity named *Semblance* (Douze & Laster, 1979) has been used. The semblance is defined as the power in the beam divided by *M* (number of seismograms) times the total power in the traces $f_i(t)$. The semblance function varies in the range of $0 \leq S \leq 1$. The data coming from all channels have a perfect coherence if S=1.

$$S(\tau_i) = \frac{\sum_t [\sum_t f_i(t+\tau_i)]^2}{M \sum_t \sum_i f i^2(t)}; \qquad (4.10)$$

In the SSA of Kao & Shan (2004) the coherence is computed as a sum over stations constituting the array (see Chapter 3 for details). In the implementation presented in this work, the result of the algorithm is not just a sum of absolute Amplitudes; instead, a normalization with respect to the number of receivers and a scanning for time windows (named *slices*) along all the traces has been introduced.

In our revisited version (explained in equation 4.9), the coherence is computed for a finite length time window (*K* samples):

$$Co(\varphi,\tau) = \frac{1}{N} \frac{\sum_{\boldsymbol{k=1}}^{\boldsymbol{K}} \left| \sum_{n=1}^{N} u_n(\tau + \tau_{\varphi n} + k\Delta t) \right|^2}{\sum_{\boldsymbol{k=1}}^{\boldsymbol{K}} \sum_{n=1}^{N} \left| u_n(\tau + \tau_{\varphi n} + k\Delta t) \right|^2}; \qquad (4.9)$$

the coherence Co in correspondence of a grid-point φ is the result of recording at each station N of each array of a normalized seismogram u_n at a source time τ plus a predicted time grid-point-station $\tau_{\varphi n}$ (theoretical travel-time) for each time-window scanning $k\Delta t$ long. In practice, the scanning of the seismograms in the time domain, is executed for each slice (0.2 s long) for continuous steps (0.1 s long) (Fig. 4.4).

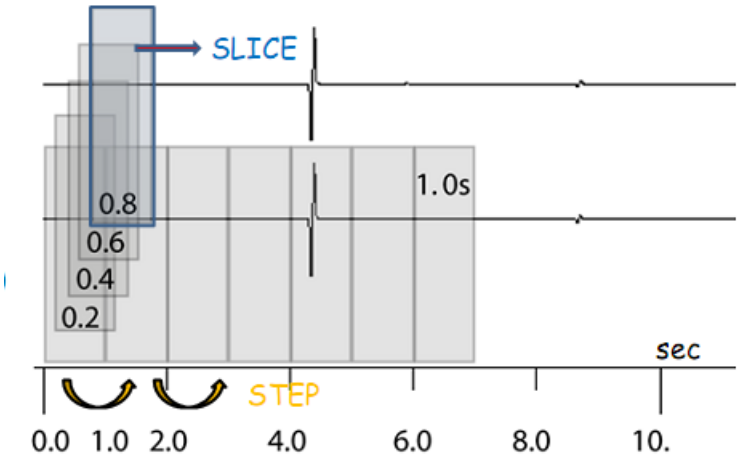

Figure 4.4: Simple representation that displays the temporal scanning performed on the seismograms of all the receivers constituting the arrays involved in the study; in this simplified example, only two traces are shown.

Moreover, the scanning algorithm computes the coherences of the seismic phase generated in correspondence of the scattering point, for each slice, by using the correspondent theoretical travel-times. In this work, the theoretical travel-times have been computed "a priori" from each receiver to each potential source both through the Tau-P package (Crotwell et al., 1999) and analytical solutions, by using a simple homogenous reference model (cf. Chapter 5). In the similar crustal application described by Rietbrock & Scherbaum (1999) and mentioned in Paragraph 4.2, a migration formulation is used. Each grid point in the subsurface is considered to be a potential scattering point. The energy stacks, or coherence values, for a time window around some phase arrival at one reference trace are smeared back into the grid volume to find potential scatterers in the subsurface. The absolute time of source (or scattering point) excitation is irrelevant and the always present trade-off between travel-time and origin time of source excitation leads to smearing of potential seismic source volumes in space and time. In the present approach instead, the reference time is assumed to be fixed for all hypothetical source points (e.g., $\tau_{\varphi n}$). Then, if the correct origin time is

approached in the scanning process are the scattering points that contribute coherently in the receiver and source arrays and thus will be imaged in the same volume. In Rietbrock & Scherbaum (1999), the receiver and source beams or semblances, respectively averaged, are summed to eventually combine all information. Here the log semblance values, equivalent to multiplying coherence values and then transforming to log-scale are summed.

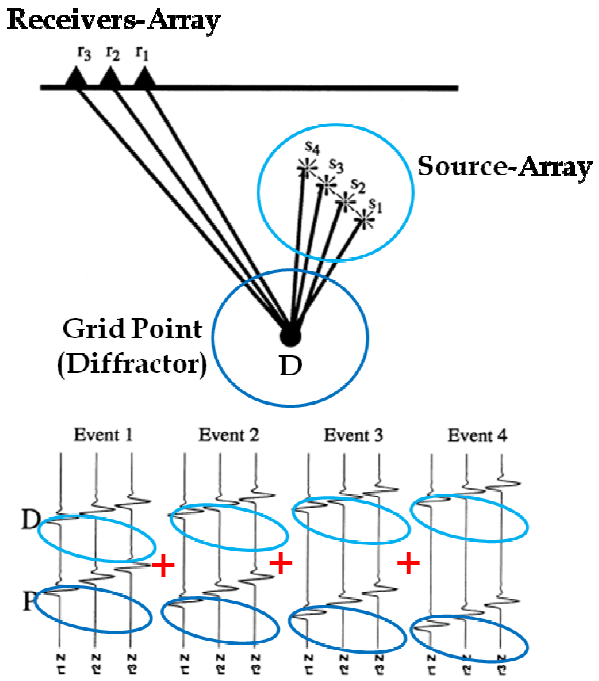

Figure 4.5: DBM approach respect to the Rietbrock & Scherbaum (1999) is shown. The blue and light blue circles represent the contribution in time of scattering point and source-array, respectively. The red symbols contribute to explain that the move-out correction respect to a defined phase D respect to the first arrival P have not been applied. The traces have been evaluated together executing the scanning of all possible coherent phases generated to the scattering points, without the move-out. The back-propagation of energy has not applied and fixed both time and source location are considered.

The resulting images can be seen as a (relative) joint log-likelihood of any point in the subsurface having contributed to the full set of observed seismograms (see Chapter 4). The concept is to evaluate all traces together executing the scanning of all possible coherent phases generated by the scattering points, without the move-out. The back-propagation of energy has been not applied, instead both

time and source location are considered fixed (Fig. 4.5). It is important to mention that in this work a single scattering model is pursued, i.e. no multiple scattering path is possible.

CHAPTER 5

Data-Set and Parameterization

This section is dedicated to the characteristics of the study area, the tectonic-geological setting, the selected data-set and the applied parameterization. In detail, the choice of data and location area is strongly conditioned and limited by the prerequisites asked from the DBM. In order to obtain high resolutions results, seismic multi-array data was chosen, recorded during the KTB-1994 experiment. Moreover, in order to setup an analysis procedure capable to apply the DBM, a "pseudo realistic" synthetic data-set was created, based on the real source-receiver configuration of the KTB1994 experiment and on a 1-D velocity model of the study area. The following section describes in detail the different steps for the best setting parameters of the input-files, the parameterization, the travel-times computation and all technical and numerical details of processing.

5.1 Introduction

For a successful application of DBM, a particular data-set and a suitable receiver and source configurations are required. The correct choice of these elements is fundamental to obtain a high resolution in the final results. The first prerequisite is to dispose of a high resolution ARF (cf. Chapter 2) for one or more arrays involved in the DBM procedure. The number and the geometry of receivers affect the array quality. The higher the number of receivers and sources, the higher the number of seismograms which contributes in the DBM to a better reduction of error in the locations of the scattering points (cf. Chapter 3). The importance assigned to location of seismic sources increase significantly in DBM respect to the others array methods. The accuracy of an exact identification of scatterers is proportional to the number and the correct location of hypothetical (gridding of the source space). The importance of having a well-performing data-set is crucial during the code testing and a similar data-set is almost unique both in terms of

array-geometry and source locations. In order to perform a best investigation of the crustal scatterers by using the DBM method, a detailed knowledge of the geological and tectonic setting of the study area is needed. Many reasons characterize the KTB-1994 (see Paragraph 5.2) as an appropriate data-set for the testing procedure:

- the geologically noted deep drilling zone
- the relations between the analysis method and the induced seismicity (e.g., during the CO_2 storage)
- the availability of a very detailed location of seismic sources that will constitute the source-array for DBM application
- a number of geological, chemical and structural studies conducted in KTB-area that contribute together to obtain a good starting model for CAP (cf. Chapter 4).

5.2 The KTB-1994 Experiment

In December 1994 at the German Continental Deep Drilling Program KTB drill site (http://www.geophysik.uni-kiel.de/wwwts/ICDP/; Emmermann & Lauterjung, 1997) in south-east Germany (Bavaria; Fig. 5.1), a fluid injection-induced seismicity experiment was conducted in the framework of the ICDP program (http://www.icdp-online.org/front_content.php). This drilling project consisted in a pilot-hole of 4 km and a main-hole of 9.1 km (Zoback & Harjes, 1997; Jost et al., 1998).

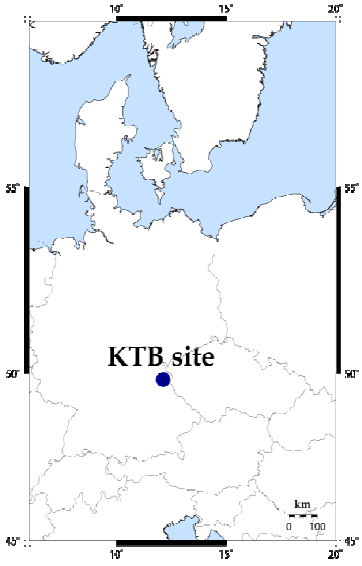

Figure 5.1: Location map of the Continental Deep Drilling Site (KTB) borehole in south-east Germany (Bavaria).

The first objective was to extend the knowledge of crustal stress based on borehole measurement down to about 7.7 km (Brudy et al., 1997; Zoback & Harjes, 1997) to the total depth of the borehole and in situ temperatures (260°C) more closely approaching 300°C, the expected onset of the brittle-ductile transition. In the KTB-1994 experiment, the borehole had reached a final depth of 9.1 km and temperatures of about 270°C. After completing drilling, hydraulic-fracturing and fluid injection experiments were performed for evaluating the brittle/ductile transition hypothesis in the crystalline crust at an unprecedented depth level (Zoback & Harjes, 1997; Brudy et al, 1997). Aside from the rheological background of the injection experiment, the induced seismicity enabled a detailed study of source properties and scaling relations for these unique data. A temporary network was installed in the region surrounding the KTB drill site to record any seismicity induced by injection of 200 m^3 of KBr/KC1 brine at the bottom of the borehole. This temporary network consisted by 73 short-period seismic stations (200-Hz sampling rate, 1-Hz sensors) at the surface around the KTB drill site. The network was configured in four concentric rings of about 1 km (A-ring), 5 km (B-ring), 10 km (C-ring) and 15 km (D-ring) radius (Fig. 5.2). This configuration ensured a good coverage of the focal hemisphere The stations of

the inner two rings were arranged in sub-arrays with 4 and 9 sensors. Additionally, a three-component borehole geophone (1000-Hz sampling rate, 28-Hz sensor) was installed at 3.9 km depth in the KTB pilot hole, about 200 m west of the main hole (Jost et al., 1998). Portable digital acquisition systems with Global Positioning System (GPS) time signals were used in a continuous recording mode to avoid missing the expected small signals associated with the induced events (Zoback & Harjes, 1997). . After two hours injection the induced seismicity resulted in 400 seismic events with $-2 \leq Ml \leq 1.2$ generated at an average depth of 8.7 km close to the borehole. Most of the seismicity occurred in seismic clusters, and the recorded waveforms are very similar.

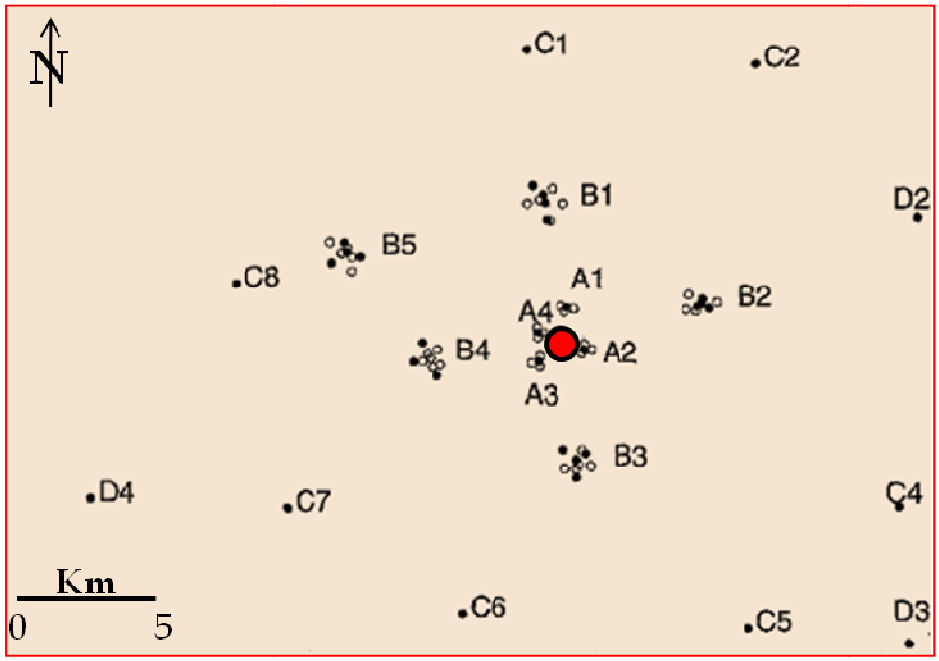

Figure 5.2: Geometrical distribution of 73 short-period seismic stations (200-Hz sampling rate, 1-Hz sensors) of KTB drilling project. The stations were configured in four concentric rings of about 1, 5, 10, and 15 km radius from the borehole (red circle). Open circles indicate vertical sensors; filled circles, three-component stations (Jost et al., 1998).

The fault-plane solutions for several micro-earthquakes have been determined using first-motion polarities and *SH/P* amplitude ratios from records of the surface stations (Herrmann, 1975; Snoke et al., 1984). Since most events were too

weak to reliably read the first-motion polarity, the similarity of waveforms have been used to produce compound fault-plane solutions (Büßelberg et al., 1995; Zoback & Harjes, 1997). The largest of 400 earthquakes had a local magnitude of M_L=1.2 with a strike-slip/reverse source mechanism (Zoback & Harjes 1997). All events belonging to the same cluster apparently have the same or at least a very similar focal mechanism. In Fig. 5.3 the two main seismic clusters (named Cluster 1 and Cluster 4) of focal mechanisms for the strongest M_L = 1.2 event are shown: a strike-slip mechanism at an average depth of about 8.9 km and a strike-slip/thrust mechanism at an average depth of 8.6 km (Jost et al., 1998).

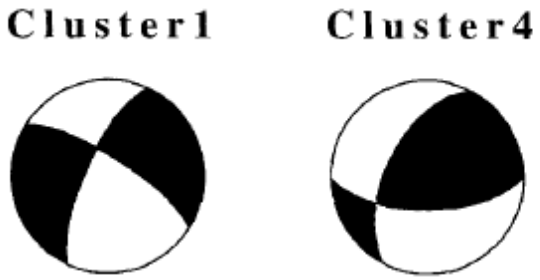

Figure 5.3: The obtained strike-slip mechanism for cluster 1 at an average depth of about 8.9 km and strike-slip/thrust mechanism for cluster 4 (with the M_L = 1.2 event) at an average depth of 8.6 km (from Jost et al., 1998).

5.3 Geological and Tectonic Setting of KTB area

The KTB drilling site is located at the western margin of the Bohemian Massif, at the contact zone of the two southern units of the Variscan belt in Europe (Saxothuringian and Moldanubian; Wagner et al., 1997). At this suture zone, the Saxothuringian plate in the north-west collided with the Moldanubian plate in the south-east about 320 million years ago. The Franconian Lineament is the surface expression of a major NW-SE striking and east-dipping Cretaceous thrust fault. Gneisses and amphibolites of the Bohemian Massif were thrust westward over Permo-Mesozoic sediments. The Franconian Lineament was cut at about 7 km depth in the borehole in addition to other numerous faults at various depths (Harjes et al., 1997). After intersecting a stack of complexly folded and faulted

metamorphic rocks, known as Erbendorf-Vohenstrauss zone (ZEV), it ends at 9.1 km depth in a tectonically crushed felsic rock unit, only two km above a prominent mid-crustal layer, the so-called Erbendorf body (Rabbel et al., 2004; Rietbrock & Scherbaum, 1999). The ZEV is an example of metamorphic crystalline crust found in many places of the Earth where multiple tectono-metamorphic cycles finally created a complex geological structure from initially simple strata. The rock column drilled at the KTB site basically consists of alternating felsic and mafic layers, mainly biotite-gneiss and amphibolite. They were steeply folded and squeezed mainly under ductile conditions and finally displaced and stacked along various conjugate and azimuthally varying fault planes. The deformation processes started in the middle Paleozoic when the Variscan terranes of the Saxothuringian, Bohemian, and Moldanubian subsequently collided. In the late Carboniferous, between 335 and 305 Ma, the final and post-orogenic collapse initiated the ascent of granite bodies found today north and east of the KTB site (Rabbel et al., 2004). The summarized overview of the tectonic and geological setting of KTB drill zone inferred from surface geology, drilling results and seismic reflections (Hirschmann, 1996; Rabbel et al. 2004) is shown in Fig. 5.4.

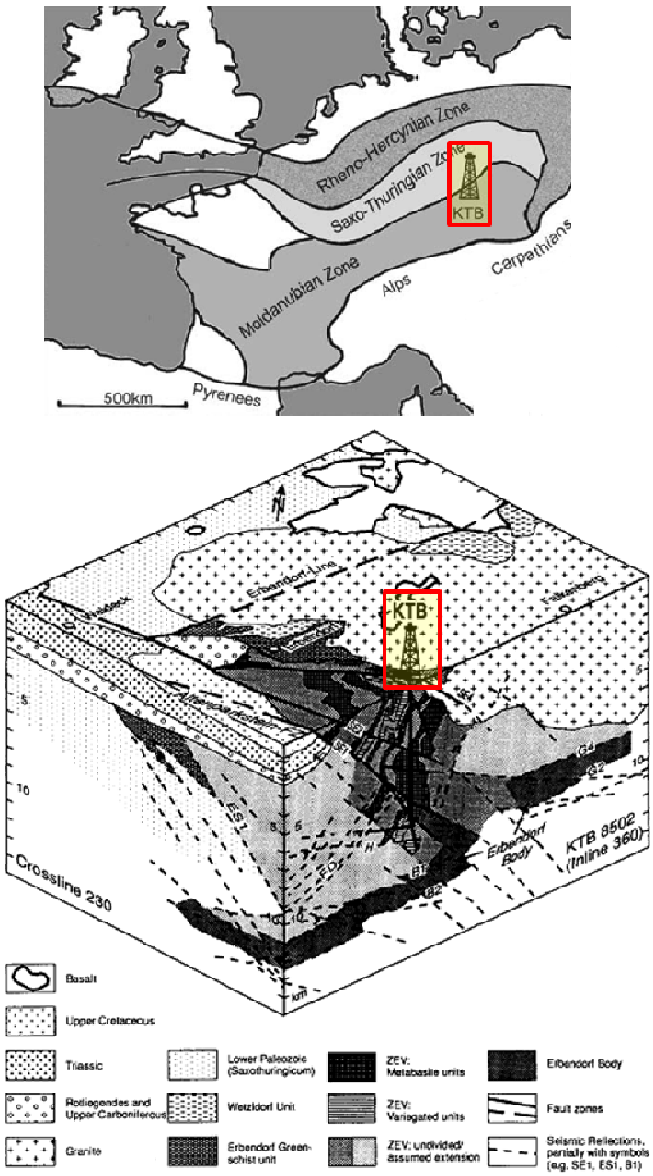

Figure 5.4: Geological and tectonic setting of KTB in plan (top) and in a 3D interpretation (bottom) inferred from surface geology, drilling results and seismic reflections (from Hirschmann, 1996; Emmermann & Lauterjung, 1997). This picture shows deep fault zones and a strong structural complexity.

5.4 Selected Data-Set

The seismic stations selected for this study are part of the KTB-1994 project (cf. Paragraph 5.2) and consists of 60 short-period seismic stations (200-Hz sampling rate, 1-Hz sensors) arranged in 9 small arrays deployed in 2 concentric rings around the KTB borehole about 1 km (A-arrays) and 5 km (B-array) radius. Each of the A- and B-arrays have been equipped with 4 and 9 stations, respectively (Fig. 5.5). The details of the receiver locations are listed in Table 5.1.

Station Name	Longitude (°)	Latitude (°)
A100	12.1251	49.828833
A110	12.128583	49.828367
A111	12.123717	49.8277
A112	12.121983	49.829283
A200	12.1334	49.815783
A210	12.136883	49.815683
A211	12.13215	49.81465
A212	12.133417	49.81735
A300	12.110817	49.811983
A310	12.111517	49.81355
A311	12.111433	49.8104
A312	12.107417	49.811483
A400	12.1107	49.820967
A410	12.11035	49.822717
A411	12.113133	49.820967
A412	12.110617	49.819483
B100	12.114167	49.861167
B110	12.113167	49.863667
B111	12.114833	49.856
B112	12.1115	49.862167
B120	12.117667	49.865833
B121	12.123	49.861167
B122	12.116333	49.856
B123	12.1055	49.861
B124	12.108333	49.8665
B200	12.190667	49.829833
B210	12.191167	49.831333
B211	12.194167	49.8285
B212	12.188667	49.829
B221	12.198	49.830333
B222	12.192167	49.825667
B223	12.183167	49.828167
B224	12.1845	49.832667
B300	12.1305	49.780167
B310	12.134	49.7835
B311	12.129333	49.778833
B312	12.1295	49.781667
B320	12.132333	49.7845
B321	12.1365	49.779667
B322	12.129833	49.776167

B323	12.123833	49.779
B324	12.123167	49.784667
B400	12.058166	49.813
B410	12.056666	49.814333
B411	12.059	49.810167
B412	12.053833	49.812
B420	12.0615	49.8155
B421	12.062833	49.810833
B422	12.061166	49.807667
B423	12.049666	49.812
B424	12.053833	49.817833
B500	12.017333	49.845667
B510	12.017333	49.847
B511	12.0195	49.844333
B512	12.014666	49.8455
B520	12.016	49.848667
B521	12.023666	49.844333
B522	12.019833	49.839833
B523	12.009666	49.8425
B524	12.009	49.848833

Table 5.1: Name, longitude and latitude of the 60 receivers used are listed.

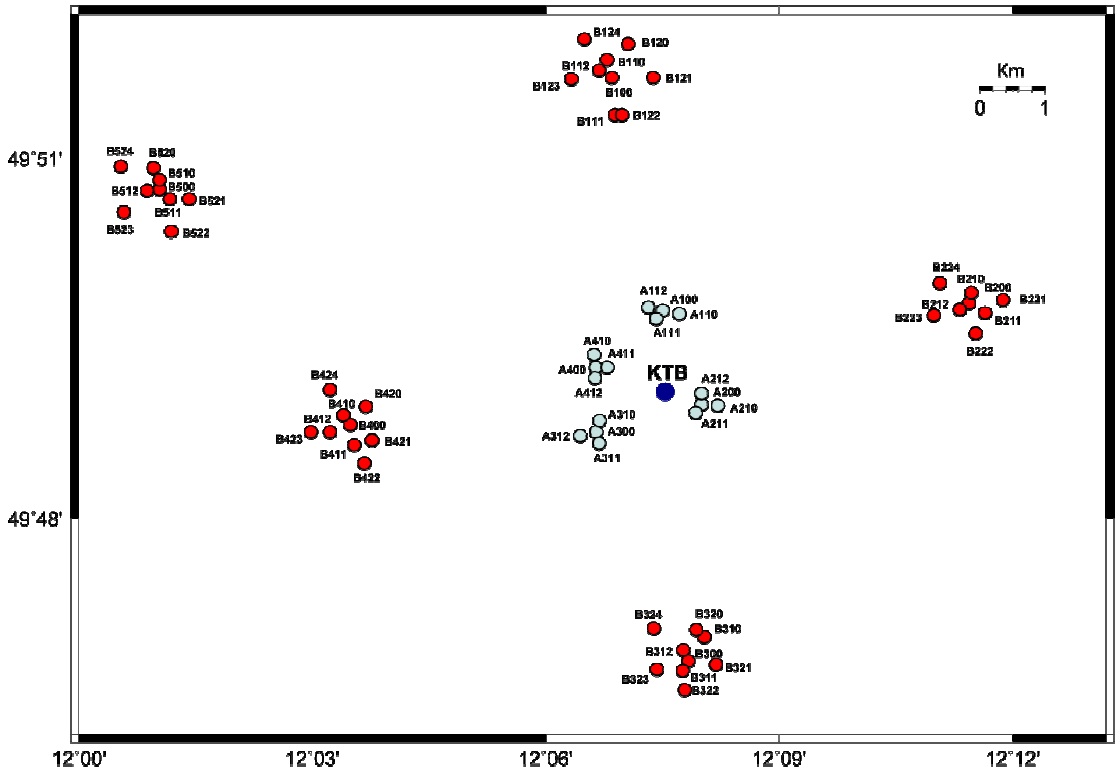

Figure 5.5: Map of the 60 seismic stations of KTB-1994 experiment selected for this work. The light-blue dots are the A-arrays and the red dots are the B-arrays. The blue dot indicates KTB borehole location.

Three or four stations for each B-arrays and only one station for each A-arrays are equipped with a three component sensors. For the preliminary analysis the M_L=1.2 event was chosen, both, in synthetic and real format (see Paragraph 5.4.1 and 5.4.2). For the arrangement and analysis of the data, we used the Seismic Handler (SH; Stammler K., 1993) software package that is a powerful seismic waveform analysis tool.

5.4.1 Real Data

The KTB-1994 data was recovered from the University of Bochum (Germany). The original waveforms were recorded in the CSS 2.8 format. The data of all 400 events (for a total of 24000 waveforms for 60 stations) have been converted first into the ASCII and then in GSE2 format, the data format required by CAP (see Chapter 4). From the entire ABCD-network, which consists of 73 stations, only data from the vertical component of those 60 stations which are organized in seismic arrays (AB) have been selected. Data was bandpass filtered in a frequency range between 1 Hz and 20 Hz.

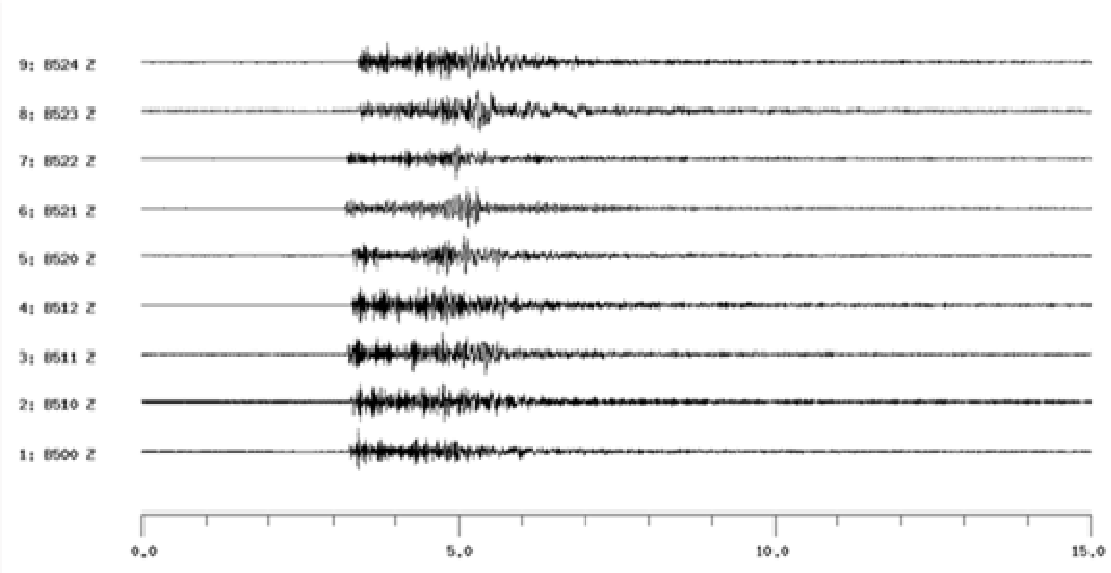

Figure 5.6: The biggest real event (M_L=1.2) recorded by B500-array in a time-window between 0 s and 15 s (Z-components) and no filtered.

Moreover, the filtered data was cut in a time-window between 0 and 15 s. Fig. 5.6 and 5.7 show the respective unfiltered and filtered seismograms recorded at array B500 for the strongest real data event (M_L=1.2).

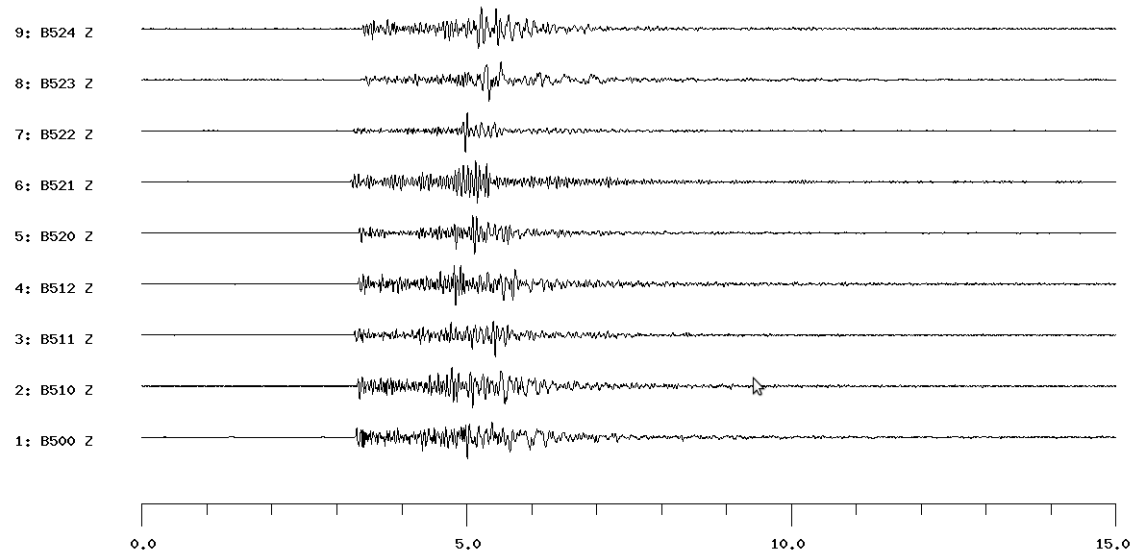

Figure 5.7: The biggest real event (M_L=1.2) recorded by B500-array in a time-window comprised between 0 s and 15 s (Z-components) and filtered between 0 Hz and 15 Hz.

5.4.2 Synthetic Data

In order to test and to better understand all the features of the implementation of the DBM in CAP, a set of synthetic seismograms have been computed reproducing the major characteristics of the real data. Two different typologies of sources have been simulated: an explosion and a double-couple event. The explosion is an isotropic source and hence the seismic energy is radiated spherically, whereas in the seismic double-couple case the radiation pattern depends on the fault and slip orientation. For the double-couple event simulation the biggest event (M_L=1.2) was chosen. In order to reproduce the focal mechanism parameters, the Cluster 1 strike-slip mechanism shown in Fig. 5.3 was approximated. The complete synthetic seismograms have been calculated for a layered half-space earth model, using the fortran-code QSEIS 5.5, by Wang (1999). For each seismic array (A,B), seismic source (S88 – S92) and source type (explosion and double-couple) QSEIS requires one single input-file , for a total of 90 different input-files, containing the following parameters (the detailed format of the QSEIS input-files is shown in the Appendix section):

- Source Parameters: for each of the five seismic sources the exact hypocentral parameters have been adopted, from Rietbrock & Scherbaum (1999). For the sources S88, S89, S90, S91, S92 the relative distances to the KTB borehole are listed in Table 5.2, the absolute locations are shown in Table 5.3. The choice of sources S88-S92 is based on the high resolution of their hypocentral determination.
- Receiver Parameters: for each array the depth (km), the number of receivers, the relative distances from each receiver and the source (km), the backazimuths of each receiver (respect to the source) are listed in ascending order of relative distances (source-receiver). In this case, the source and receiver coordinates are converted from geographical to cylindrical.
- Waveform Parameters: the start-time (s), the end-time (s), the number of samples and the wavelet duration.
- Moment Tensor Parameters: both for the explosion and double-couple event have been set:

	Mxx	**Myy**	**Mzz**	**Mxy**	**Myz**	**Mzx**
explosion	1.0E+09	1.0E+09	1.0E+09	0	0	0
Double-couple event	0.61E+09	0.02E+09	0.64E+09	0.61E+09	0.35E+09	0.34E+09

- Model: the multilayer model parameters in correspondence of the source site constituted by depth (km), P-velocity (km/s), S-velocity (km/s) and density (g/cm^3), shown in Table 5.4.

Sources	X(km)	Y(km)	Z(km)	Magnitude
S88	-0.107	-0.219	0.539	1.2
S89	-0.025	-0.199	0.509	-0.2
S90	-0.025	-0.184	0.502	-0.3
S91	-0.080	-0.267	0.527	-0.3
S92	-0.055	-0.120	0.511	-0.4

Table 5.2: Locations and magnitudes of the main Cluster 1. The coordinates are given relative to the KTB main hole bottom (12.1256E 49.81765N, −8.5362 km). The location uncertainties are in the range of tens of metres (Harjes, personal communication); from Rietbrock & Scherbaum (1999).

Sources	Longitude (°)	Latitude (°)	Depth (m)
S88	12.125	49.8156	-7.9972
S89	12.1255	49.8158	-8.0272
S90	12.1255	49.8159	-8.0342
S91	12.1251	49.8152	-8.0092
S92	12.1253	49.8165	-8.0252

Table 5.3: Absolute locations of sources extracted by the Table 5.1 (Rietbrock & Scherbaum, 1999).

Several test have been performed before establishing the final values for the QSEIS input-files.

Setting the following waveform parameters: start-time -2.0 s, end-time 38.95 s record length 4096 samples, sampling rate 100 sps, wavelet duration 0.2 s for each trace have been noted not good results (not focusing, anomalous coherence values) in the results after the CAP-run (see Paragraph 5.6), interpreted as the "wrap-around effects" (that is a effect produced in the time-domain in the traces when the sampling is not sufficient for the Fourier Transform executed during the data-creation with QSEIS) . In order to suppress these effects, the waveform parameters have been changed as follows: start-time -2.0 s, end-time 77.99 s, record length 8192 samples, sampling rate 100 sps and a wavelet duration of 10 s

for each trace. Moreover, the reasons of the start times setting (-2 s) are related to the sample adjustment between the CAP-code and Seismic-Handler setting. In detail, the start-time of QSEIS is located 1 s before the CAP source-time, this 1 s difference corresponding to 193 samples. In this way, a total number of 600 Z-component waveforms have been reproduced: 300 for the isotropic source and 300 for double-couple events, respectively. Examples of waveforms produced for array B500 are shown in Fig. 5.8 and 5.9, representing the synthetic explosion and synthetic double-couple event in a time window between 0 s and 15 s.

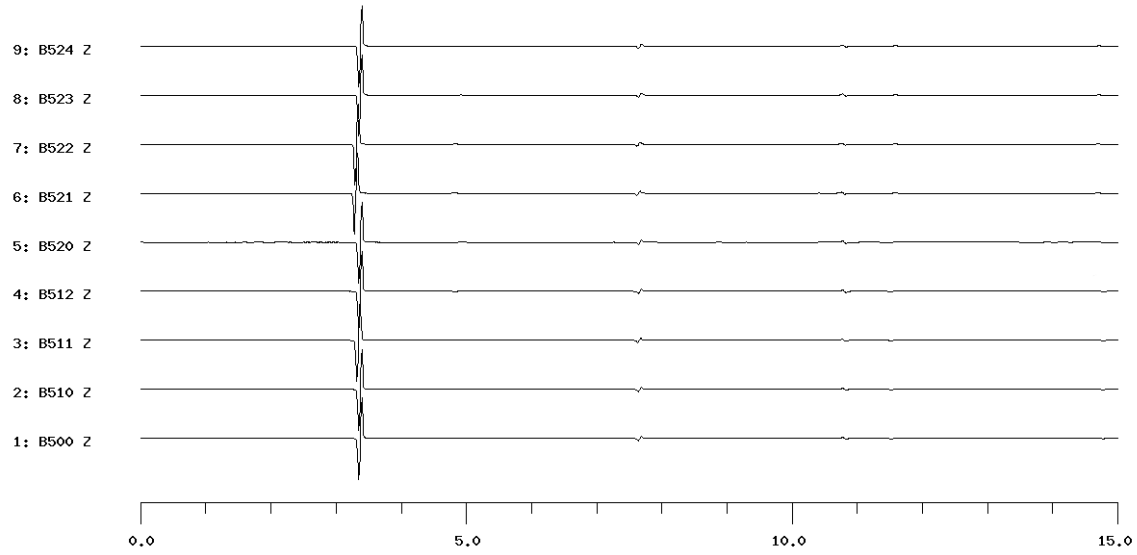

Figure 5.8: The seismic explosion reproduced for the B500-array using QSEIS-code (Wang, 1999) in a time-window comprised between 0s and 15 s considering the source S88 (Z-components).

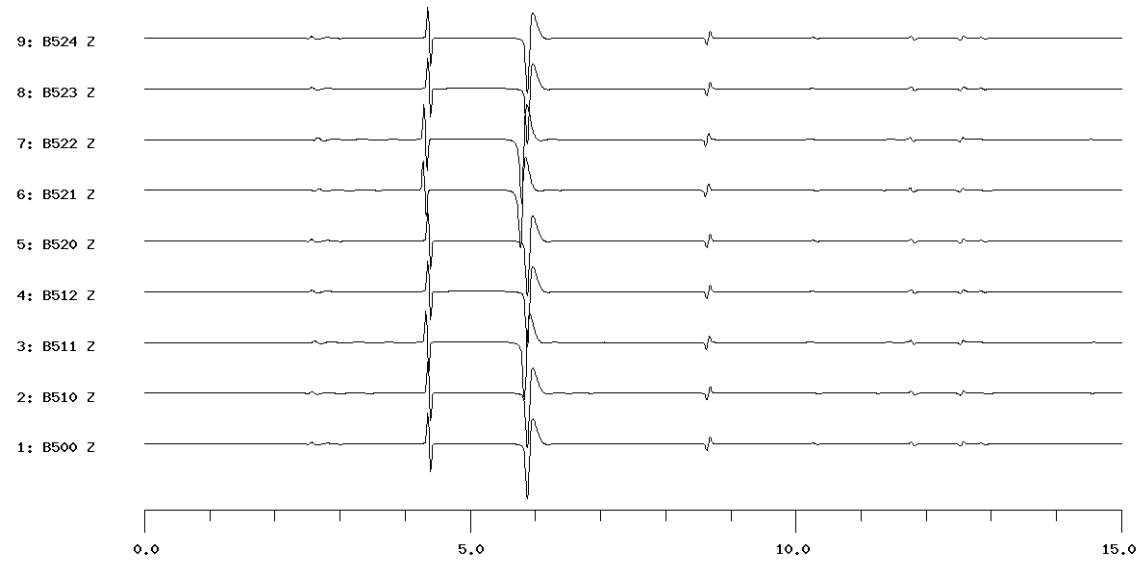

Figure 5.9: The seismic double-couple event reproduced for the B500-array using QSEIS-code (Wang, 1999) in a time-window comprised between 0s and 15 s considering the source S88 (Z-components).

5.5 Parameterization and Travel-Time Computation

One of most the important elements that contributed to a successful application of our approach to the DBM is the correct parameterization of the study area. The study area encompasses a crustal volume of 20x20x33 km^3 (Latitude-range: 49.7277°/49.9677°; Longitude-range: 11.9989°/12.2522°) dimensioned and enveloped in surface around the KTB borehole (Lat: 12.1256°; Lon: 49.8176°). Each depth layer of this crustal volume was gridded into 1681 nodes, representing the hypothetical scattering points. The node spacing amounts to 500 m horizontally and 1 Km in depth. This results in 41x41x34 cells that correspond to a total of 57154 potential scattering points in the crustal volume (Fig. 5.10). The simple 1D scattering model shown in Fig. 5.11 is used for the synthetic data testing. To achieve the double beam configuration (constituted by one array of receivers and one array of sources) the receivers were arranged in different configurations, in order to test the best resolution. The array geometries considered and tested during the analysis are the following:

A. Only one single array/one source
B. Multiple single arrays/one source-array
C. Big-One array/one source-array

The geometry A, "Only one single array" means that one single array of nine elements constitutes the "receiver array" in the DBM, for each of the five sources. Geometry B, "Multiple single arrays" implies that all nine arrays have been used to constitute the "receiver array", even if the computation of coherence were effectuated individually for each single array and for each of the five sources. Geometry C, "Big-One array" denotes that the receiver array is constituted by all 60 receivers together for each of the five sources.

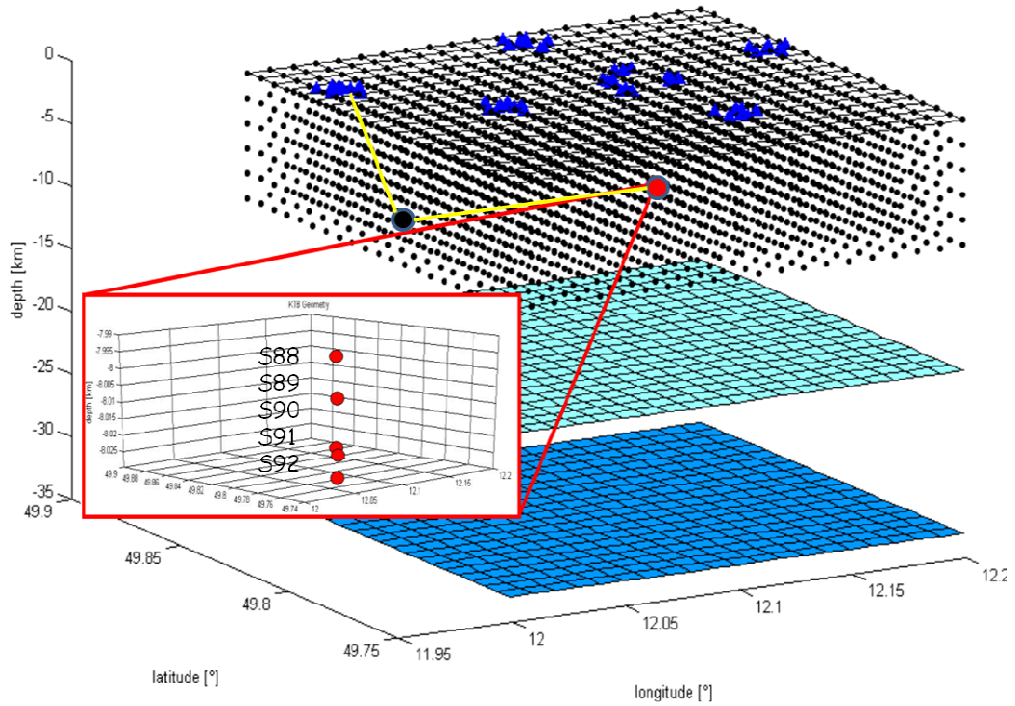

Figure 5.10: Parameterization of the crustal volume. The zoom window shows in detail the depth location of the five seismic sources used. The blue triangles depict the receivers of nine multiple seismic arrays; The black dots indicate the nodes (potential scattering points). Light blue and blue planes represent crust and mantle discontinuities. The large red, green and black dots denote source, receiver and scatterer examples, respectively. The yellow lines are the hypothetical ray-paths.

Other elements needed are the seismic phases and the respective travel-times produced by the scattered seismic energy across the crustal model. The theoretical travel-times computation is one of the most important steps of the procedure. Moreover, the CAP-code needs the theoretical travel-time files to compute the coherences for each time-slice during the scanning. This was realized (i) through the TAUP (Crotwell et al., 1999) software and (ii) by with analytical solutions. Both ways of computation need for each grid point of the parameterized volume a coordinate file (longitude and latitude) 57154 lines long. According to the 1D model illustrated by Table 5.4 and Fig. 5.10, the principal possible seismic phases and relative travel-times have been computed, produced by the propagation of seismic energy from a source located at about 7.9 km depth within the first layer of the model.

SCATTERING MODEL

Depth[km]	Vp[km/s]	Vs[km/s]	ρ[g/cm^3]
20.000	5.0000	3.0000	2.7000
33.000	6.5000	3.7000	2.9000
40.000	7.8000	4.4000	3.3000

Table 5.4: The 1D scattering model used for the crustal volume parameterized is shown.

Based on the chosen parameterization, the ray paths sketched in Fig 5.11 are needed, from the sources to each grid point and from each grid point to the receivers. In Fig. 5.11, the green dashed lines represent the sources-to-grid-points and the blue lines the grid-point-to-receivers paths. The computation of the theoretical travel-times must be done for the scattered phases (PP, SS, PS and SP) associated to these ray paths. First, the resolution of TAUP for very small scale distances (hundredth of meters) has been tested through the comparison with analytical solutions. Then, the theoretical travel-times were computed introducing the Tau-P (*taup_create, taup_time*, see Crotwell et al., 1999) routines inside the CAP-code: during the CAP-runs the code reads in automatic procedure the travel-time tables generated. For the mantle and core model

required by TAUP, the crustal model (Table 5.4) was completed by the ak135 model (Kennet et al., 1995). To use TAUP, each grid point was simulated to be a receiver in order to compute the distances and travel-times from each source to each "receiver" grid-point. Unfortunately, this code expects the receivers at the surface only. t this point, a modification of the TAUP settings to simulate a progressive change of depths has been unsuccessfully tried. Eventually, these computations have been performed implementing the script-procedure to obtain the theoretical travel-time tables by using analytical solutions.

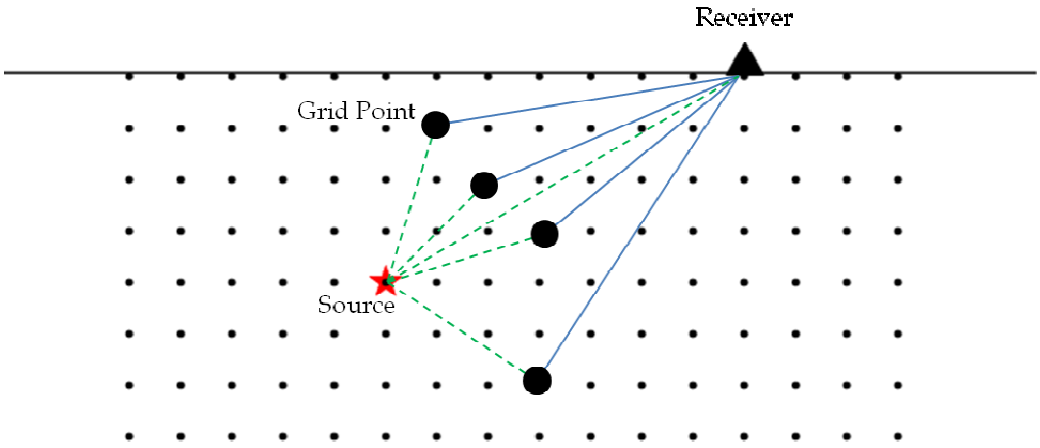

Figure 5.11: Simple scheme representing the typology of the paths used to compute the travel-time tables inserted in the CAP-runs. The red-star is the source of seismic energy, the black triangle represents the receiver in surface and the black dots are the grid-points. The green dashed-lines symbolize the direct P and/or S paths (from source to each grid-point) and the blue lines the paths from each grid-point and the receiver.

Thus, we have changed the CAP-code so that convert the travel-time tables from files produced from CAP (by using a subroutine of TAUP) to input-files for CAP to perform before the CAP-run. Finally, we have computed for each source, grid-point and receivers the theoretical travel-time tables by using analytical solutions.

5.6 The CAP code

The implementation of DBM has been integrated into the software package CAP (Continuous Array Processing; Ohrnberger 2004) in order to obtain images of seismic sources (and scattering points) in both space and time. This seismic code was originally devised to study the site effects and dispersion curves. The extraction of dispersion curve information from ambient vibration array recordings and the subsequent inversion for the shallow shear wave velocity structure especially for sites within urban areas has been the subject of Task B (WP05-07) of the European Community financed project SESAME (Site EffectS ASsessment using AMbient Excitation, EU-Grant No.: EVG1- 2000-00026).The software package CAP has been developed within the scope of this project in order to respond to the need of testing the potential of various frequency wavenumber techniques as well as the applicability of the spatial autocorrelation method for the extraction of phase velocity curves from microtremor array recordings (Ohrnberger, 2004). Nevertheless, the algorithms are implemented such that it is straightforward to use this software package for general continuous computation of wave propagation parameters in the context of seismological array analysis (Ohrnberger, 2004). All existing versions of CAP contain the same processing capabilities but differ in the I/O concept related to the underlying database structures. The different versions can be obtained from compiling the program code with different define switches and linking against different libraries. The program flow in CAP is divided into several blocks. After the program is started, user selectable parameters are read from a simple ASCII file. A cross check is performed on the given parameter settings in order to avoid unreasonable combinations of parameters or the misuse of certain methods. If the cross-check phase is passed, the waveform data is extracted from the database followed by another cross-check of data consistency (data gap detection, changes of sampling rates, availability of data window, etc.). After these initialization steps, the pre-processing block is entered. Dependent on the user's settings, CAP

allows for a limited number of pre-processing options applied to the raw waveform data. Once the pre-processing is finished, the processing loop is entered. After all available data has been processed, the raw analysis results are written to output files (Ohrnberger, 2004). In order to allow a quick visualization, a shell script is additionally created which scans the output files and creates postscript figures using the GMT software package by Wessel & Smith (1998). It is possible to apply a number of different array methods using CAP through the compiling of the setting file. The main methods include: H/V ratio computation, cross-correlation stacks, attenuation estimation, slowness response evaluation, determination of dispersion curves. CAP-code have been used to obtain the semblance values for each time-slice and grid-point set of data-set following the approach to the DBM used in this work. The possibility to select a particular and local velocity model for computing travel-time tables via *taup_time* (see Crotwell H.P. et al, 1999) has been introduced. This change has been indeed done in the file *io_funcs.c*.

5.6.1 Input files

To start the CAP-run ("*cap_sa*" command), the command lines require to set the opportune flags before each input and output file. Here an example for A100-array, SS phases and the event named 1994121800. The bold face letters are the flags correspondent to the files.

```
cap_sa -f 19941218000000.000 -l 19941218001000.000 -i mig-z.cfg -g A100+A110+A111+A112 -s
A100.slist -w synthetic.flist -c ktb.region  -m A100.S.tttable -o A100-Z < extra.miginp >&
A100-Z.log
```

Thus, the CAP-run needs to have the following compiled input-files available in the work directory:

- *starting-time-name:* the name (`19941218`) and the starting time (`000000. 000`) in seconds of the waveform to analyze . The flag is "-f".
- *end-time-name:* the name (`19941218`) and the end time (`001000. 000`) in seconds of the waveform to analyze. The flag is "-l".

- *mig-z.cfg*: the processing setting file (see Appendix for details). This is the richest input-file because it contains a number of information about the processing. For example, here the method, the length of windows (that we named *slices*) for scanning and the *steps* related, the Gaussian coefficient, the up-sampling, the decimation, the file-out, etc etc... can be set. Before to insert the final values, the tests on the Gaussian parameter (that control part of the resolution of the images) have been executed, introducing 0.3, 0.5 and 0.05 for each type of run; the best value chosen (reaching agood focusing and coherence in base of a visual analysis) to the final procedure is 0.05. The slices have been chosen 0.2 s length after a number of attempts in base of the frequency, wavelenght and considering the phases involved in the computation. The flag is "-i".
- `A100+A110+A111+A112`:the names of all stations that compose the analyzed array. The flag is "-g".
- *station.slist*: for each array involved in the analysis we created one file containing information about name, component, longitude, latitude and sensor (see Appendix for details). The flag is "-s".
- *synthetic.flist*: a waveform list file in which the absolute path and format of the data (the first two lines marked with "#") and the relative paths and header lines for each waveforms of the station (GSE2 formatted) are indicated. The flag is "-w". (see Appendix for details).
- *ktb.region*: this is the file that defines the study area in terms of latitude/longitude (°), number of latitude and longitude steps, number of layers in depth (km), depth (km) max and min (see Appendix for details). The flag is "-c".
- *tttable:* the travel-times file. For each grid point (for all depths) and receiver (in the reverse configuration as well) the travel time for each phase involved in the analysis is indicated. The flag is "-m".

- *model.nd:* file related to the model used. In this case it is the global ak135-model from the Moho depth to the inner-core. The top of the crust is changed according to a local model. This is constituted by six columns indicating depth (km), P-velocity (km/s), S-velocity (km/s), density (kg/m^3) and attenuation factors (for the crust only). This file must be present in the work directory even if not present in the command line for CAP-run.

```
crust
   0.000   5.0000    3.0000    2.7000      300.0   60.0
  20.000   5.0000    3.0000    2.7000      300.0   60.0
  20.000   6.5000    3.7000    2.9000      300.0   60.0
  33.000   6.5000    3.7000    2.9000      300.0   60.0
mantle
  33.000   7.8000    4.4000    3.3000      300.0   60.0
  40.000   7.8000    4.4000    3.3000      300.0   60.0
410 8.9 4.7 3.5
410 9.1 4.9 3.7
670 b10.2 5.5 4.0
670 10.7 5.9 4.4
2891 13.7 7.2 5.6
outer-core
2891 8.0 0.0 9.9
5149.5 10.3 0.0 12.7
inner-core
5149.5 11 3.5 12.7
6371 11.3 3.7 13
```

5.6.2 Output files

The CAP-code generates the main following output files for each array analyzed named: *tfbox*, *max* and *stmap*. The *tfbox* file is a simple ASCII file consisting of a header line starting with a '#' symbol, where the total number of time windows is specified as well as the number of frequency bands used. The columns contain start time relative to the absolute start time given, the length of the time window in seconds, the lower and the upper frequency limit. The *max* file is the main output file of CAP containing header information followed by analysis results in plain ASCII. The *stmap* files are the most important files for our application and an example of uppermost part is showed here:

```
# Time slice: 0 - Time: 787708802.000000
49.727700 11.998900 0.000000 0.142101 61556169714.224350 215.785432
49.727700 12.008900 0.000000 0.082141 36029752558.612564 211.133226
49.727700 12.018900 0.000000 0.135431 50796464565.754318 214.116670
49.727700 12.028900 0.000000 0.103576 41010733832.786201 212.257951
49.727700 12.038900 0.000000 0.160452 58325505760.233727 215.317170
49.727700 12.048900 0.000000 0.130601 52052334037.327744 214.328804
49.727700 12.058900 0.000000 0.133886 46799229727.214455 213.404774
49.727700 12.068900 0.000000 0.083818 36397463115.276070 211.221422
49.727700 12.078900 0.000000 0.141214 949053299262.864136 239.54581
49.727700 12.088900 0.000000 0.020056 402630225286.064209 232.098127
49.727700 12.098900 0.000000 0.069345 1316624983494.609131 242.389242
49.727700 12.108900 0.000000 0.142873 1317970552786.249512 242.398114
49.727700 12.118900 0.000000 0.214126 769858487726.836792 237.728218
49.727700 12.128900 0.000000 0.207120 421327894874.229248 232.492404
49.727700 12.138900 0.000000 0.099610 389035347791.126465 231.799781
49.727700 12.148900 0.000000 0.041885 404603930673.811462 232.140602
.........

.........
```

The first line starting with '#' symbol and followed by the slice-number and the correspondent time. From the second line there are seven columns with: the coordinates of grid-point (°), the depth (km), the semblance, the power $[nm/s]^2$ and semblance power, respectively. Last ones structure is repeated for each slice computed. The key of analysis is this *stmap* file. The final semblance values have been plotted by using GMT software (Wessel & Smith, 1998) constituting the final results of the work (see Chapter 6). Here the log semblance values (equivalent to multiplying coherence values and then transforming to log-scale) are summed.

CHAPTER 6

Progress of Work and Results

This section illustrates the main work-steps from the application of the DBM method. The flow chart describes al the working steps, starting from the input synthetic data to the CAP output files, which contain the coherence values for each scattering point of the investigated crustal volume. In the second step the chosen method to represent the coherences and the images of all the source- and receiver-array configurations are explained. At last, the best final results are analyzed and discussed.

6.1 Introduction

It has been already emphasized that the DBM is not a common tool in seismology. The largest number of DBM applications in literature are relative to studies on mantle discontinuities and the core/mantle boundary (cf. Chapter 3). In literature only one DBM application has been devoted to the crust, at a very small-scale (Rietbrock & Scherbaum, 1999), from which this work has been inspired. Though using a similar dataset, the method and procedure devised in this study are original and illustrated below. The final representation with the coherence distributions defining the scattering maps of the investigated crustal volume are produced for a number of different testing steps to evaluate the source-receiver-array combined configurations. Comparison of different results on the basis of focusing and resolution obtained in the final images has allowed to evaluate the best procedures to be followed.

6.2 Procedure Flow

The implemented procedure consists of two parts: (i) the computational part, starting from the production of synthetic data up to the calculation of the coherence values by customizing the CAP software and (ii) the imaging part, that consists in illustrating the CAP output-files as images of scattered crust.

In this paragraph, the first part of the procedure summarized in the flow chart of Fig. 6.1 is explained. The starting point is the creation of the files containing information necessary to the QSEIS input-files (cf. Chapter 5) in order to construct the synthetic data-set. A C-shell script (*compute_dist_azi.scr*) has been written (i) to convert the source- and receiver-coordinates from absolute geographical to relative cylindrical coordinates, with respect to each of the considered KTB-sources (S88, S89, S90, S91, S92) and (ii) to compute the new relative source-station distances (km) and back-azimuths (°). The following steps have been the production of the synthetic seismograms and the organization of work directories. The data produced have been converted from *ASCII* to GSE2 format and reallocated in six working directories: multiple-receiver-arrays, source-arrays, big-one arrays, both for the isotropic and the DC source. For each working directory there is one sub-directory containing the seismic data and one sub-directory containing the CAP files for each source. In the case of reverse configurations the sub-directory-data contains the same correspondent data, but re-arranged. After compiling the input-files for the CAP code, the runs have been executed computing the coherence for one single array and one single source at a time. The second step of the procedure consists mainly in the management of the CAP output-files (*stmap*, cv. Chapter 5) containing the semblance values for each grid-point. Once the single array coherences are obtained, they must be combined according to the geometries and the established configurations (A, B, C; see Chapter 4). In order to accomplish these combinations the semblance amplitudes are multiplied between them, so that the smaller energies have been suppressed and the larger ones have been amplified. In this way, a series of combined semblances are obtained and plotted as a function of the depth of the crustal volume studied.

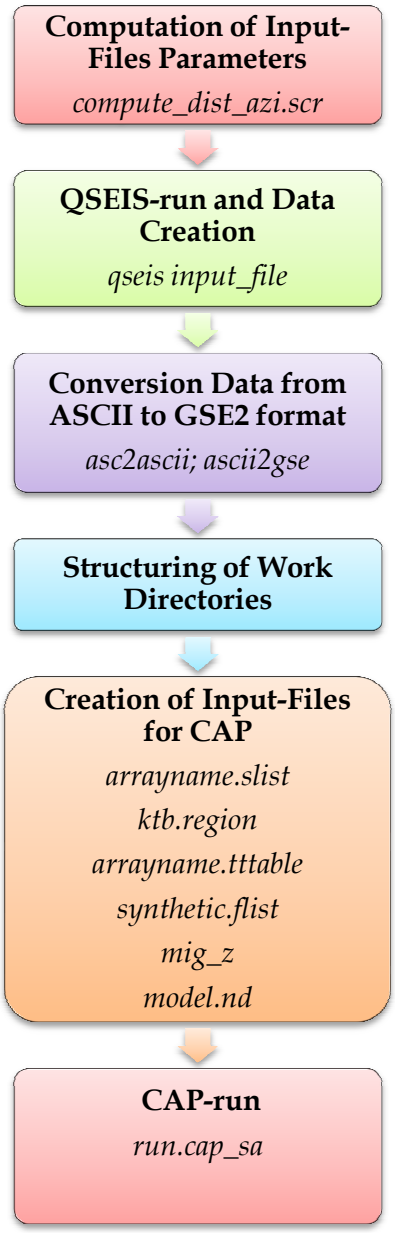

Figure 6.1: Flow chart of the first part of the procedure: from data creation to the CAP-run. The file names are indicated in italics.

In order to test the parameter settings, the focusing, the resolution and the robustness of the method, a series of tests on semblance combinations has been performed, applying different array-source geometries. In the next Paragraphs examples about the main geometries tested are summarized.

6.2.1 Coherence Mapping Tests

In the first example, a single array and single source for the simulated explosion have been combined and plotted, according to the A-geometry in Paragraph 5.5. In Fig. 6.2 results are shown for A100-array and S88-source, plotting the semblance distribution for the first eight time-slices, for a layer at 8.5 km depth. The source is located at about 7.9 km depth. The red and blue areas indicate the maximum and minimum semblance values, respectively. The explosion occurs at the time-slice number 5 and the maximum of energy is therefore expected to radiate from this moment on. Large semblance values distributed far from the source in space and earlier than the timing of explosion in time, with implausible circular pattern or linear orientation, are thus artefacts due to the Gaussian coherent noise of the synthetic data caused by QSEIS default. This becomes clearer in the second example, where all nine arrays and one single source for the explosion have been combined and plotted, according to the B-geometry in Paragraph 5.5. In Fig. 6.3 the semblance distribution for the same depth and the same time-slices of the previous example is shown. Comparing Fig 6.2 (single array) and Fig. 6.3 (multiple array), the major difference that can be noted is the complete suppression of the incoherent and smaller energies once more arrays are combined. The energy maximum is expected around the source (black and red stars), but the plots show still the presence of unrealistic circular and/or linear patterns. Even if these images have demonstrated the good suppression capability of the incoherent phases by combining information from several arrays, artefacts are still present since energy is not completely focussed. These problems may be caused by e the Gaussian noise of synthetic data, that becomes coherent and/or by the incorrect setting of parameters of input-files. Thus, after these first results part of the input parameters have been reset and a new data was generated (see Chapter 5).

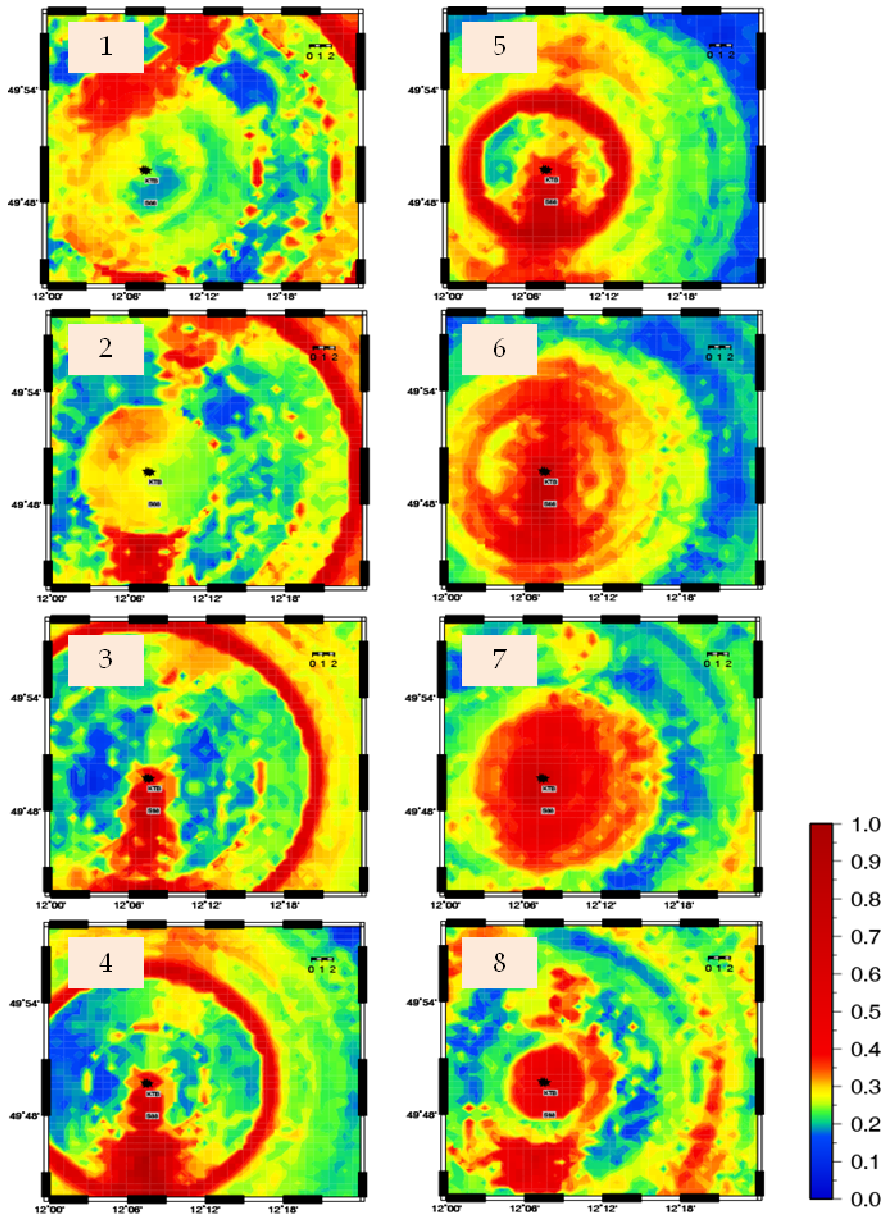

Figure 6.2: Semblance distribution for the combination of the S88-source-array and the A100-receiver-array. The first eight time-slices for a layer at 8.5 km depth are shown. Time-slices are numbered in the white boxes. On the right side the color palette for the semblance scale is plotted The maximum of coherent energy is concentrated in correspondence of the maximum semblance (red areas). The black stars map the location of the A100-array. The spatial scale (0-2 km) is shown at the top-right side of each plot.

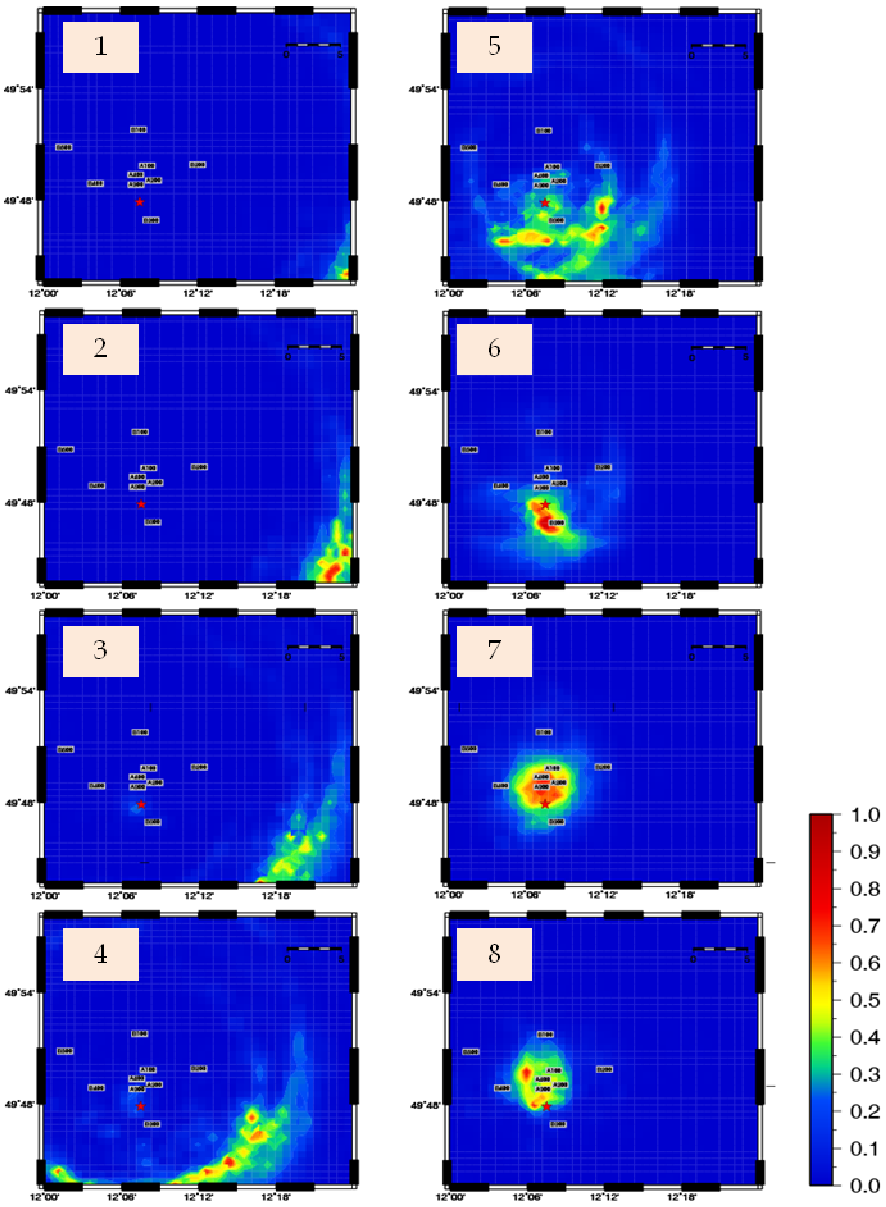

Figure 6.3: The same semblance distribution for the S88-source-array as in Fig. 6.2: now for all nine receiver-arrays. The first eight time-slices for a layer at 8.5 km depth are shown. The maximum of coherent energy is concentrated in correspondence of the maximum semblance (red areas). The red star indicates the KTB location. The spatial scale (0-5 km) is shown at the top-right side of each plot..

Fig. 6.4 illustrates the results obtained by using the new data for the simulated explosion and the same configuration as the previous example (all nine arrays and a single source, S88). The new results are presented for four selected depths (0 km, 8 km, 20 km and 33 km) chosen on the basis of the symmetry to the source

depth (7.9 km) and considering the discontinuities of the model used. The semblance distribution is plotted for three different time-slices starting at 2 s, 6 s and 8 s after the start-time of explosion. Fig. 6.4 illustrates clearly the presence of a very high focusing of the maximum semblance values around the seismic source (red star) and the complete suppression of incoherent phases (blue areas reveal the total absence of coherent energy).

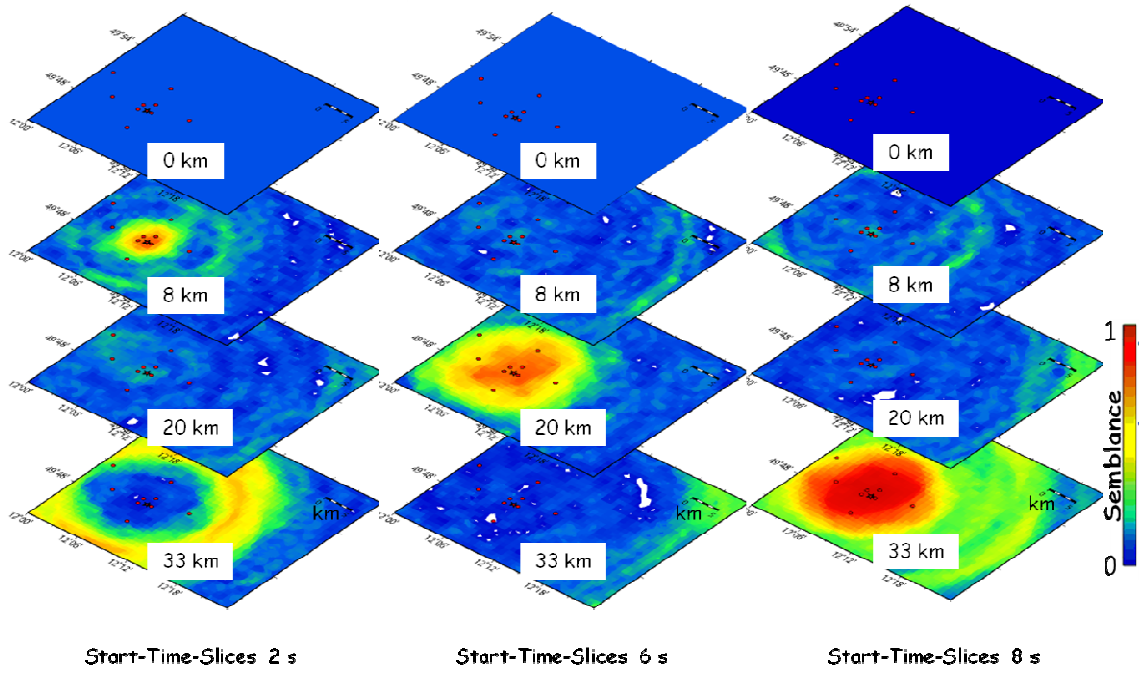

Figure 6.4: Semblance distribution as a function of depth (selected layers at 0, 8, 20 and 33 km) for the configuration of all-arrays and one single source (S88). Three different time-slices are shown, starting 2 s, 6 s and 8 s after the simulated explosion. The semblance colour palette is shown on the right. The red star and dots symbolize the KTB and arrays locations, respectively. The blue areas indicate the total absence of coherent energy.

Analysing the first time-slices (2 s, left picture column of Fig. 6.4) two main focuses at 8 km and 33 km can be noted. At 8 km depth, the energy is concentrated around the source. The contrast between the yellow-green smeared areas and the sharp red area close to the source is very strong. At a depth of 33 km, the presence of the yellow circular shaped area around the seismic source

projection (star) at this explosion-time (that corresponds to 2 s , then at the time-slice number 10) caused by mirror effects thus not to be interpreted as real coherences. Therefore, applying this method to synthetic data it is very important to distinguish between identify real coherences and artefacts. In order to correctly interpret the results a good knowledge about local geology and the features and characteristics of the used computer codes have to be taken into account. The second time-slice series freezed at 6 s present high semblance values at 20 km showing a good focusing around the projected source and receivers (red star and dots). However, the third time-slices (8 s) show an extended red area and the entire surface at 33 km presents high values of semblance. For these geometry and configuration have been obtained the good results in terms of focusing, depth attempted and semblance values.

6.2.2 Big-One configuration

The "Big-One" configuration consists of one large array formed by all 60 receivers of the 9 sub arrays (A, B) and one single source (c.f. the C-geometry in Paragraph 5.5). Fig. 6.5 shows the results for both, isotropic source and a synthetic double-couple event (S88-source), for time-slice n° 10 (start time???), plotted for each of the 33 crustal depth layers.. In the case of an isotropic source, the red areas that indicate the maximum semblance are located at 8, 20, 28 and 30 km. In the case of the double-couple event, the semblance distribution is not homogeneous but presents small irregular and smeared areas (red colour) from 0 km - 12 km, 19 - 20 km, 22 - 24 km, 28 -30 km. Even if the time-slice is close to the source start-time, the semblance related to the source is not focused, rather the energy results distributed across the upper 12 km depth layers.

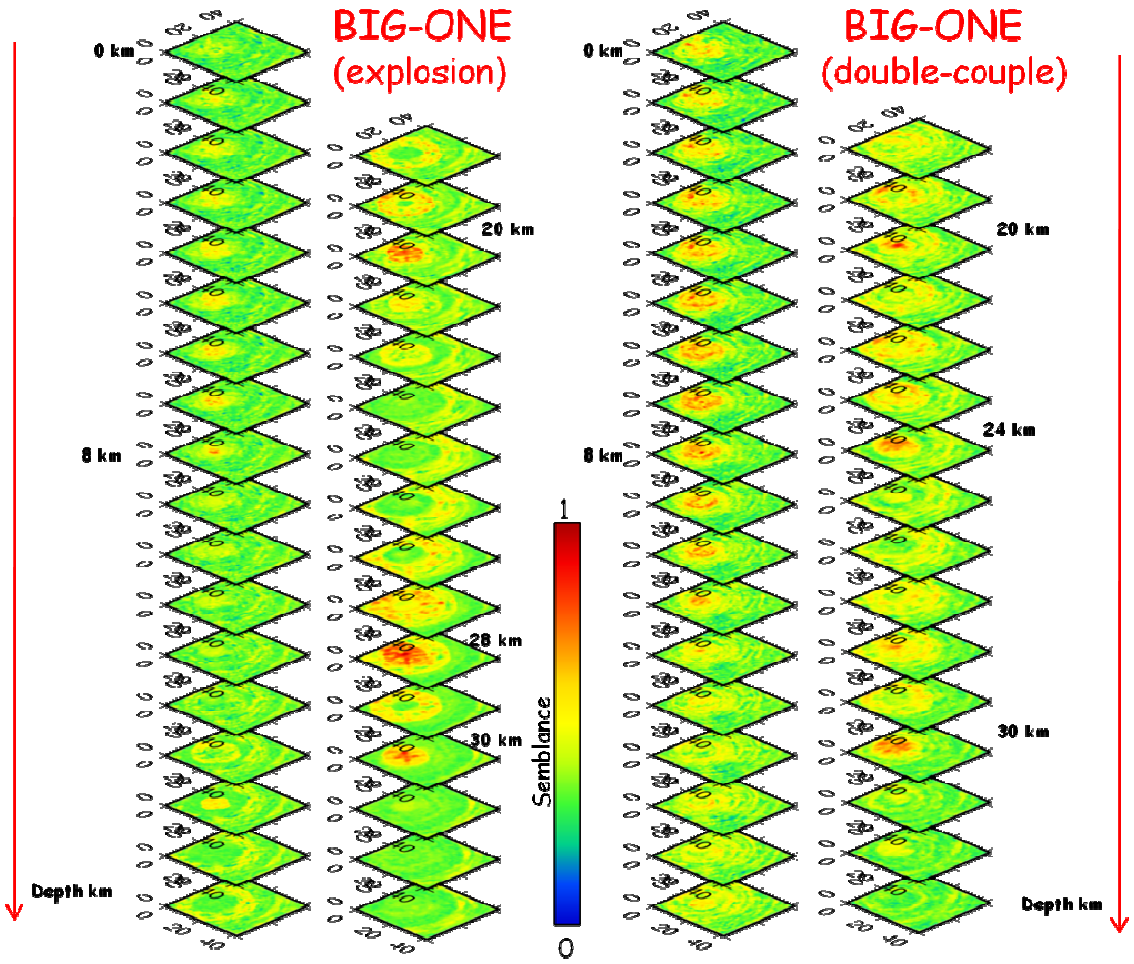

Figure 6.5: Semblance distribution as a function of depth for the Big-One array configuration, for both explosion (left) and double-couple (right) events. The most significant depth values are displayed at the maximum focusing of semblance (red areas) and all maps are related to a single time-slice (10). The semblance palette is shown in the middle.

Moreover, with respect to the other examples (see Fig. 6.4) the semblance values are generally very high for the entire area (green and yellow areas, the blue areas are not present) and for all depth layers.

These preliminary applications have been useful to evaluate the correct parameter setting. In the following paragraphs, the main final configurations characteristics for the DBM are presented.

6.3 Source-Array Analysis

In the following the reverse configuration is analysed All seismic sources have been combined to constitute the source-array; all 60 receivers in surface constitute the sources at the surface. Analyses for explosion and double-couple event are made using both PP phases only and PP-SS-PS-SP phases.

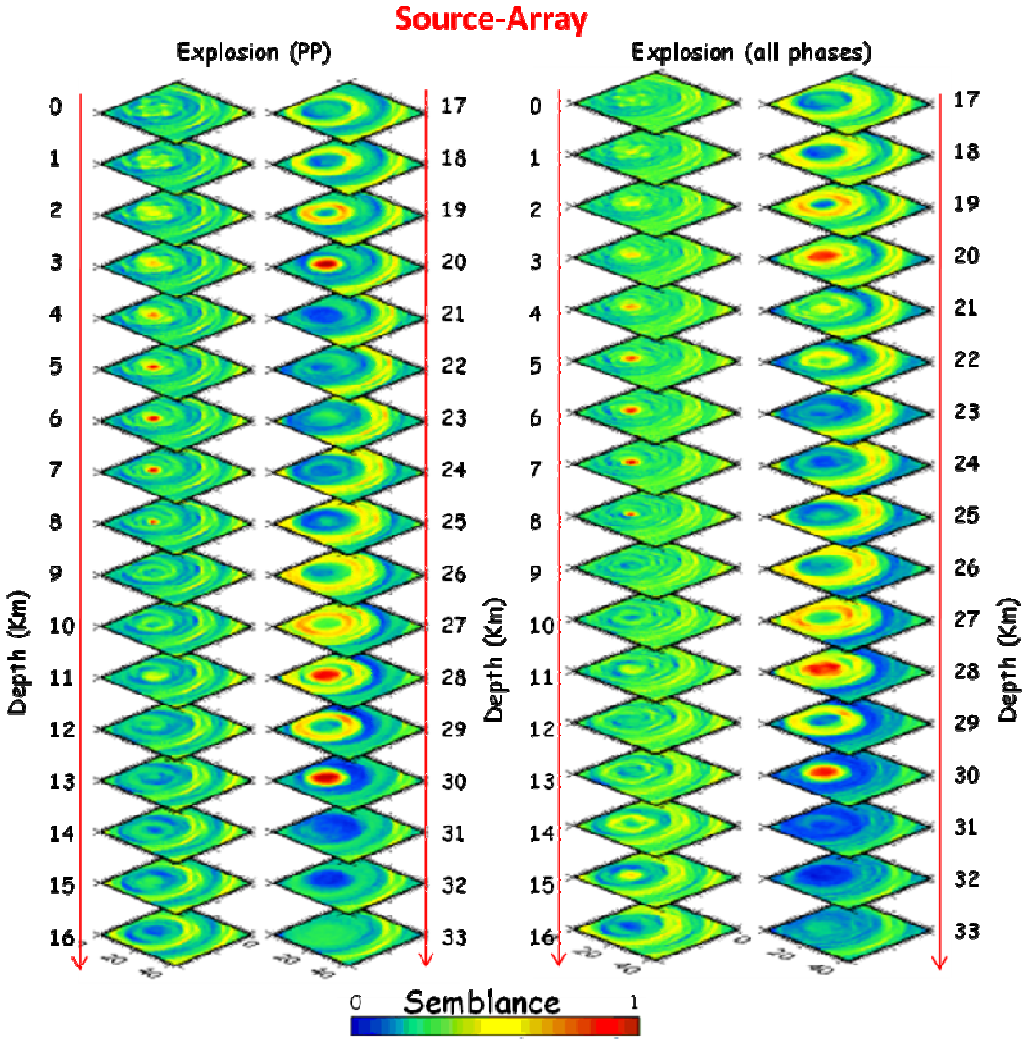

Figure 6.6: Semblance distribution for the Source-Array (explosion) as a function of depth (0–33 km). The time window is related to the time-slice 10 (start-time for event). Both PP (left plot) and PP-SS-PS-SP (right plot) case-study are shown.

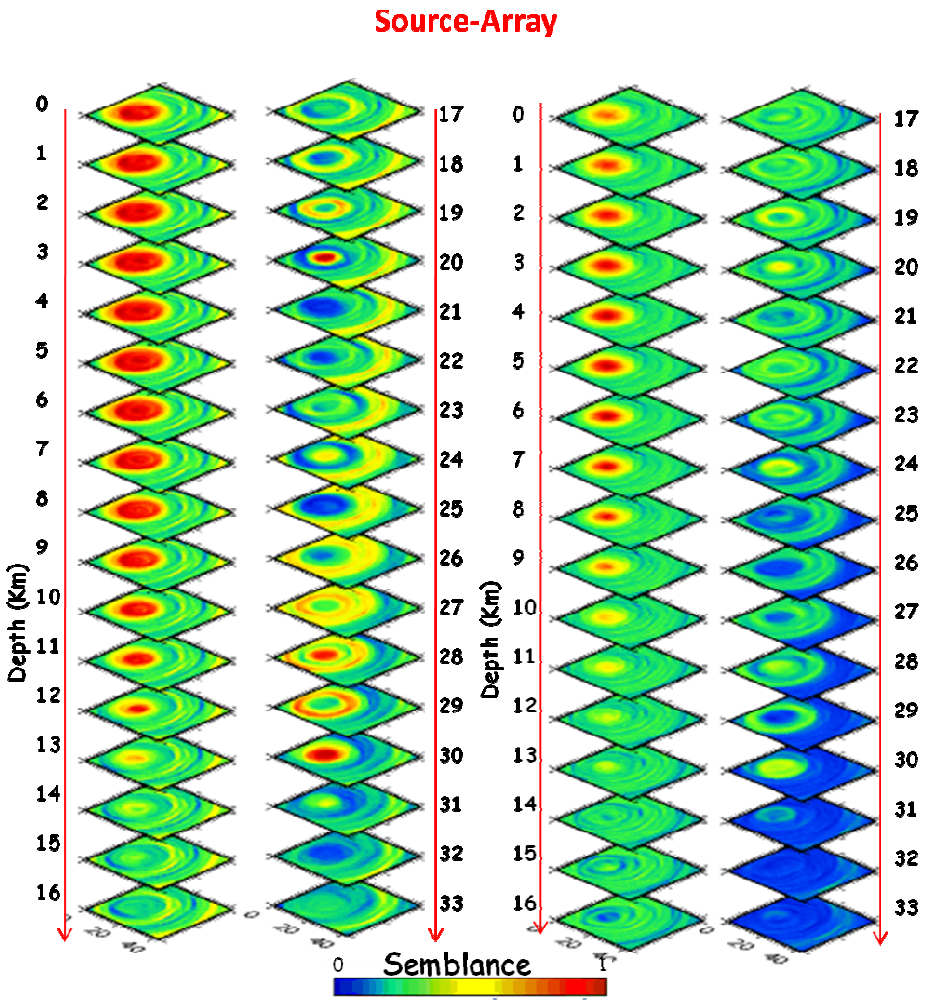

Figure 6.7: Semblance distribution for the Source-Array (double-couple event) as a function of depth (0 – 33 km). The time window is related to the time-slice 10 (start-time for event). Both PP (left plot) and PP-SS-PS-SP (right plot) case-study are shown.

In Fig. 6.6 and Fig. 6.7 the semblance distributions are plotted as a function of depth (between 0 km and 33 km) at a single time-slice close to the start-time of the seismic event. Examining the explosion (Fig. 6.6) it can be noted that both, the analysis of PP and all-phases show a good focusing, represented by the circular red areas around the source of seismic energy, in correspondence of 4-8 km, 20 km and 28-30 km. For the PP-phase the semblance contrast is about 50% larger respect to the all-phases study. In the double-couple case (Fig. 6.7) the area of high semblance values are not spatially focused at all. Moreover a strong smearing phenomenon can be observed, visible for all the upper depth layers of

Fig. 6.7 as large red-coloured areas. In the PP phases analysis the smearing is stronger and extended between 0 km and 12 km. In the all-phases analysis the red areas are smaller and shallower, ranging between 0 km and 9 km. The other areas with high semblance are located at 20 km, 28 km and 30 km, but for the PP analysis only, while in the all-phases case the scattering points located at depths larger than 20 km are not detected.

6.4 Receiver-Array Analysis

The analyzed configuration is constituted by all the nine small arrays as receivers and all the five single sources at depth. Analyses for the explosion and the double-couple event are again performed using both PP phases only and PP-SS-PS-SP phases. In Fig. 5.8 and Fig. 5.9 the semblance distributions are again plotted as a function of depth (between 0 and 33 km) at a single time-slice close to the start-time of the seismic event. Examining the explosion case (Fig. 5.8) it can be observed that both PP and all-phases plots show that high semblance values are focussed at 5-8 km, 20 km and 28-30 km. If only PP phases are considered the maximum semblance areas (red zones) are better focussed. For shallow depths, the focussing is very effective. Contrarily, in the case of the double-couple event (Fig. 5.9) a smearing phenomenon is present up to the surface, with extremely large semblance red areas. In the PP analysis the diameter size of these red areas is about 10 km, from 0 km to 12 km depth; in the case of all-phases analysis these areas are smaller (about half the size of PP case) and located from 0 km to 11 km depth. Other high semblance areas are located at 20 km, 28 km and 30 km both for PP and all-phases analysis. In general, for depth values larger than 20 km, the high semblance zones reveal a good focussing only for PP analysis, while small semblance values characterize the all-phases analysis.

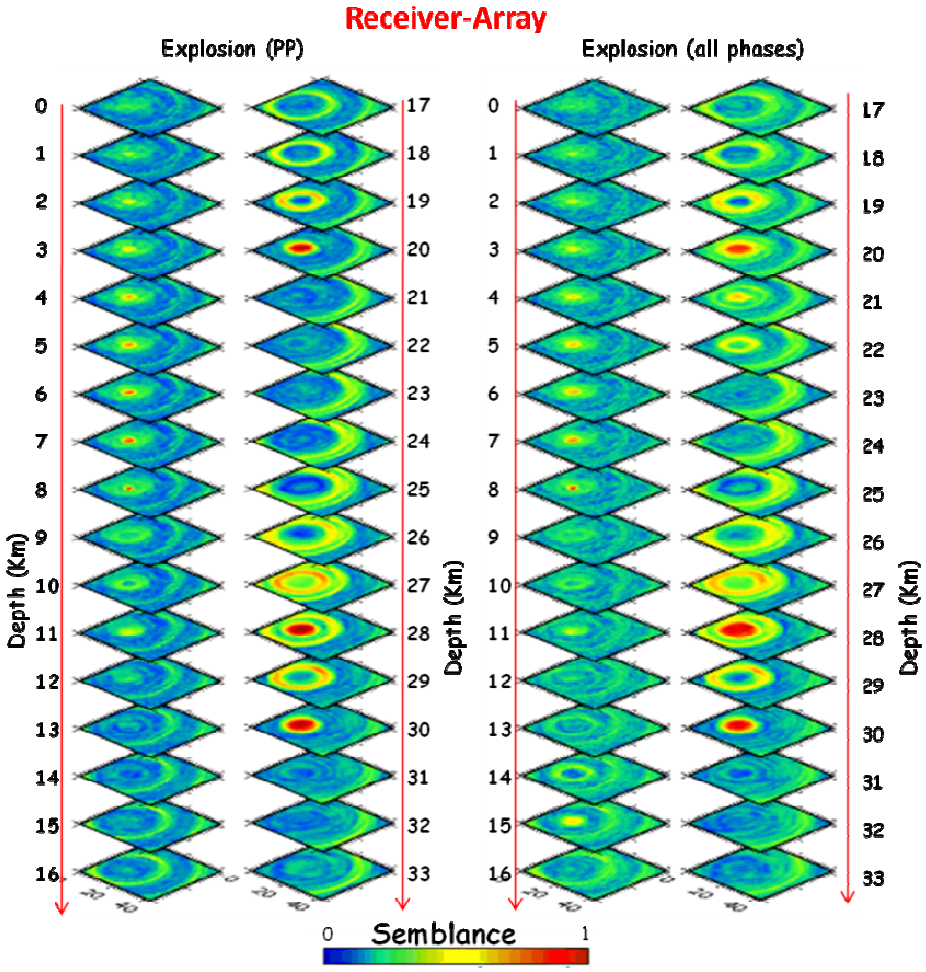

Figure 6.8: Semblance distribution for the Receiver-Array (explosion) as a function of depth (0 – 33 km). The time window is related to the time-slice 10 (start-time for event). Both PP (left plot) and PP-SS-PS-SP (right plot) case-study are shown.

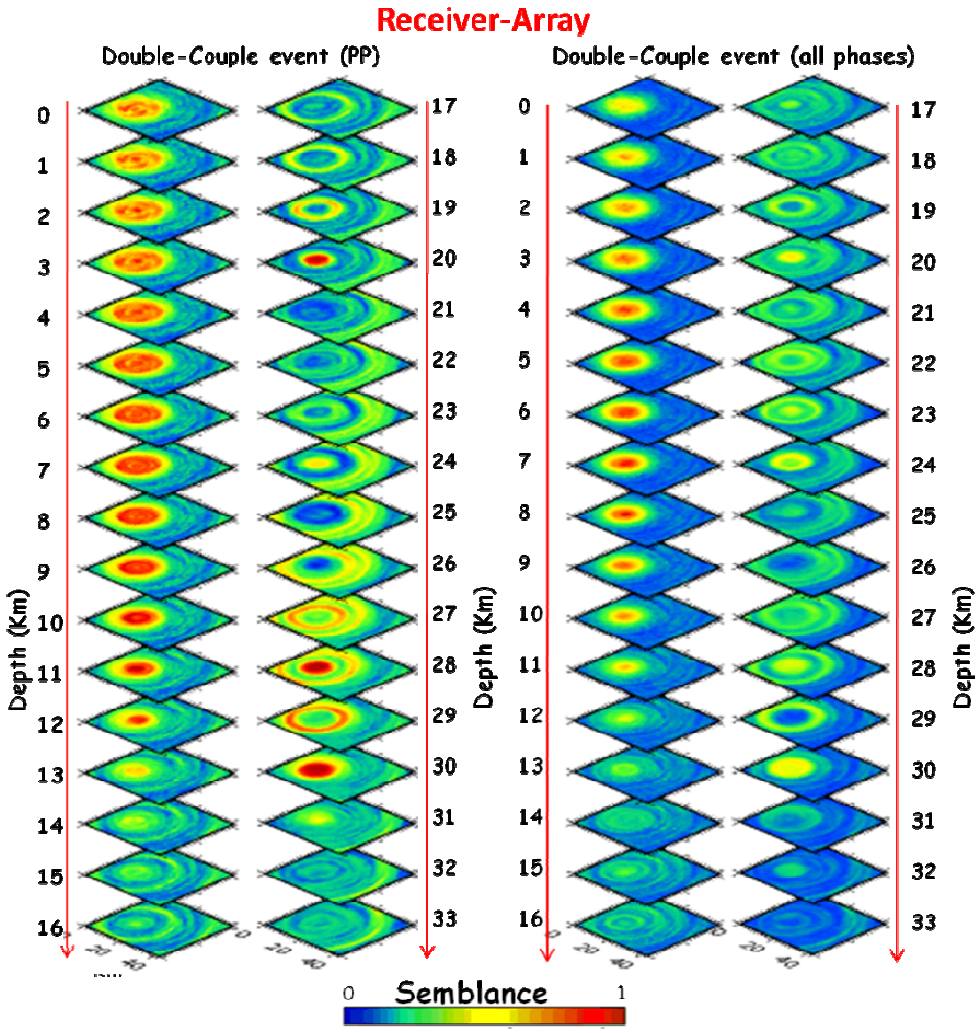

Figure 6.9: Semblance distribution for the Receiver-Array (double-couple event) as a function of depth (0 – 33 km). The time window is related to the time-slice 10 (start-time for event). Both PP (left plot) and PP-SS-PS-SP (right plot) case-study are shown.

6.5 Double Beam Results

Once evaluated the different aspects of the method by analyzing specific combinations, source- and receiver-arrays have been combined obtaining the double beam. Again, the explosion (Fig. 6.10) and double-couple event (Fig. 6.11) cases by using the PP phases only and all-phases (PP-SS-PS-SP) have been studied. In Fig. 6.10 the contrast in the semblance distributions is very large, suggesting a good suppression of incoherent phases. Moreover, the maximum of coherence is localized, indicating a very good focusing mainly between 5 and 8

km for both the phase typologies. Other focused areas of high coherence are located at 20 km, 28 km and 30 km depth.

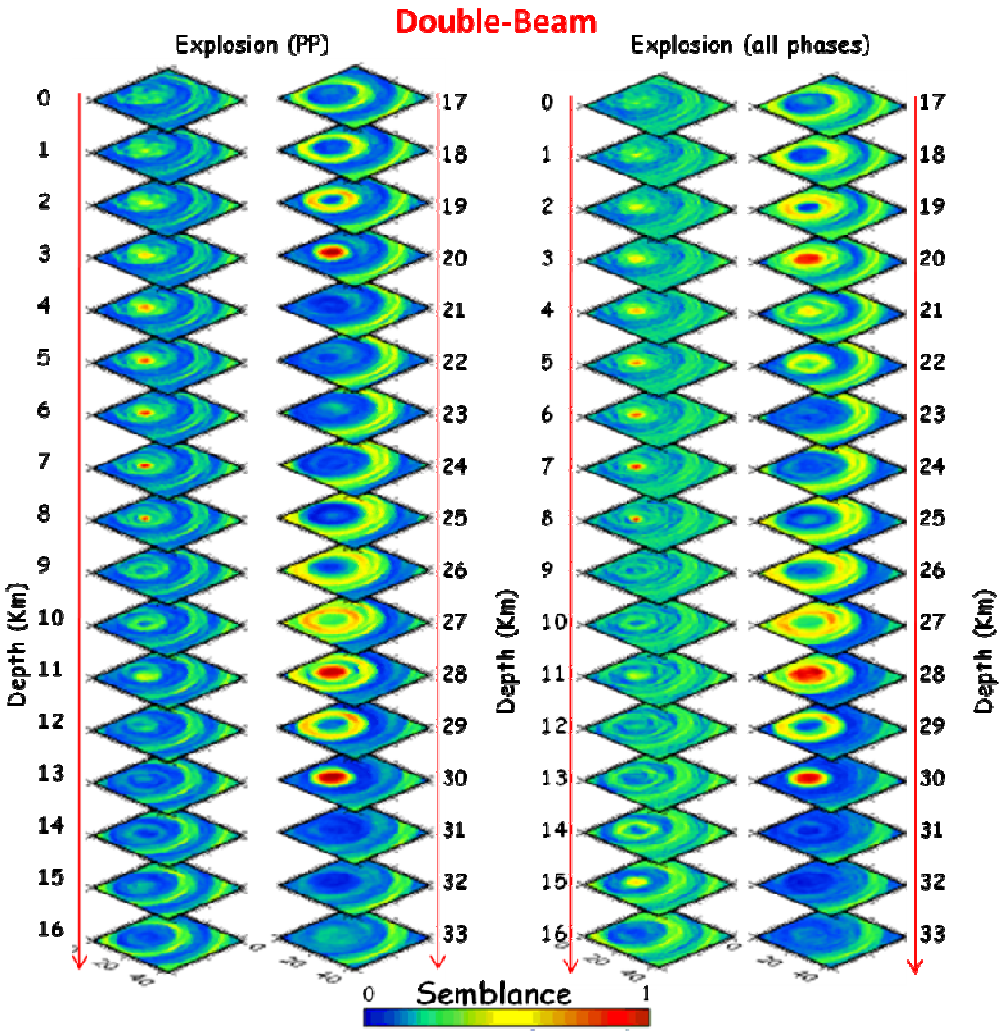

Figure 5.10: Semblance distribution for the Double Beam (explosion) as a function of depth (0 – 33 km). The time window is related to the time-slice 10 (start-time for event). Both PP (left plot) and PP-SS-PS-SP (right plot) case-study are shown.

The double beam configuration obtained from the double-couple event is shown in Fig. 6.11. In the upper crustal layers the areas with maximum semblance values are smeared between 0 - 12 km (for the PP case) and between 0 - 10 km for the analysis of all-phases.

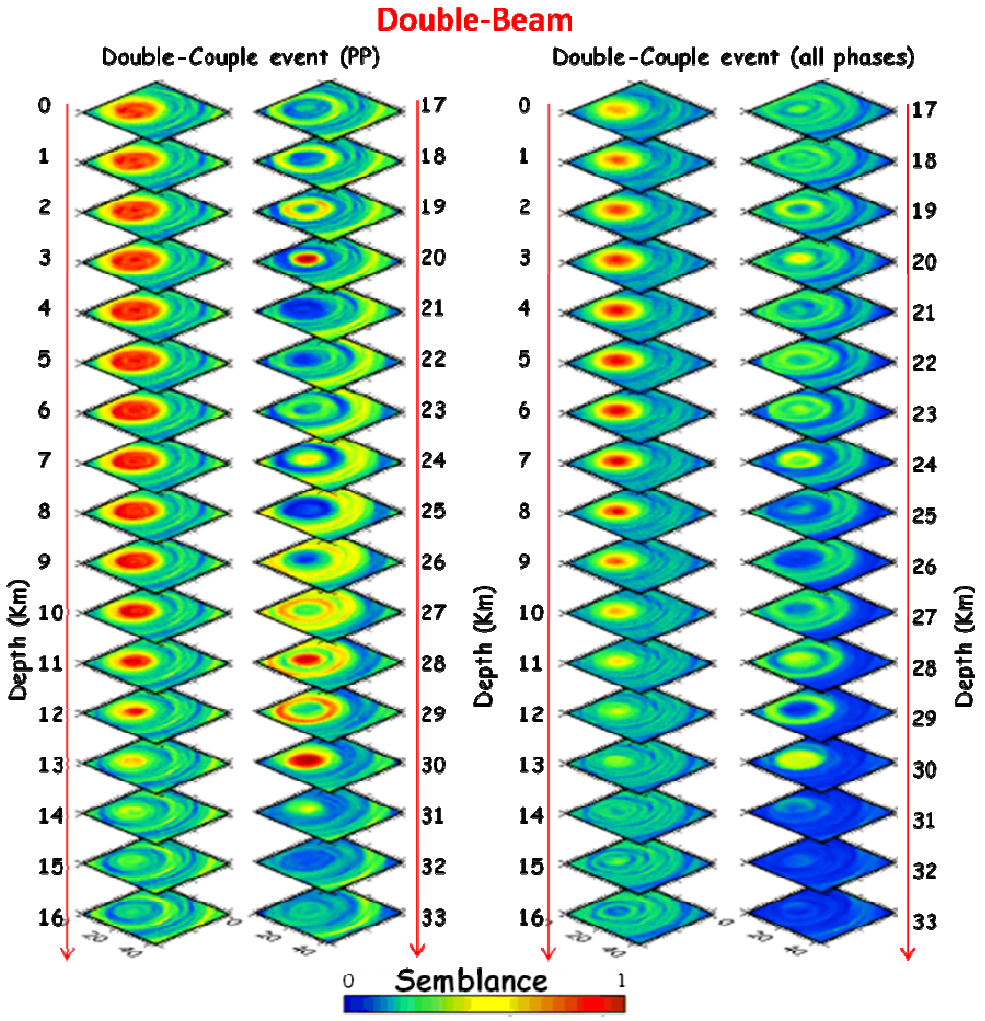

Figure 6.11: Semblance distribution for the Double Beam (double-couple event) as a function of depth (0 – 33 km). The time window is related to the time-slice 10 (start-time for event). Both PP (left plot) and PP-SS-PS-SP (right plot) case-study are shown.

Smearing is more evident in the case of PP analysis, whereas focussing is more effective considering all phases together. For larger depths, the maximum of semblance can be observed at 20 km, 28 km and 33 km for the PP phase study only. At the same depths the all-phases case yields medium semblance values (yellow areas).

Coherence values of this study have been plotted in 2D, but of course they are inherently 3D and the same results can be differently imaged in the study volume. Plotting different 3D views (Fig. 6.12, Fig. 6.13 and Fig. 6.14) of the

double beam explosion for PP-phase and a single time-slice (close to explosion time) allows portraying the formation of the characteristic *fan* features due to the travel-times spatial coherence.

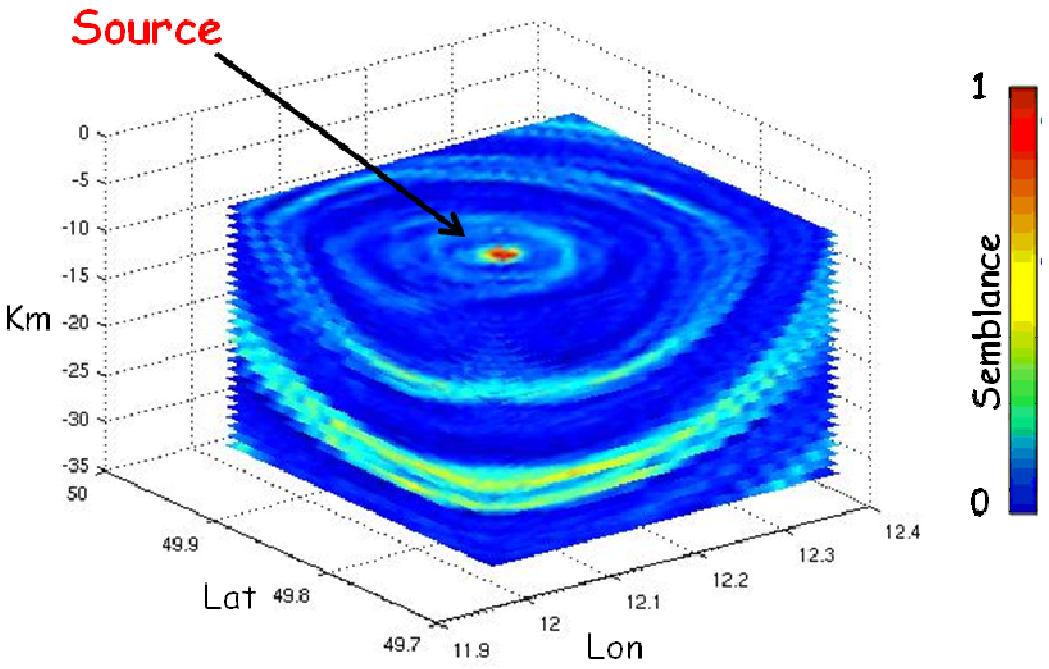

Figure 6.12: Three-dimensional view of the semblance value distribution for an isotropic source, obtained by the double beam configuration using PP-phases only. The image represents a photograph shot at a single time-slice (10). The black arrow indicates the source energy location with the maximum energy concentration (red zone). The yellow and light-blue bands represent the fans (at an initial stage for this time slice), i.e. the travel times spatial coherence zones.

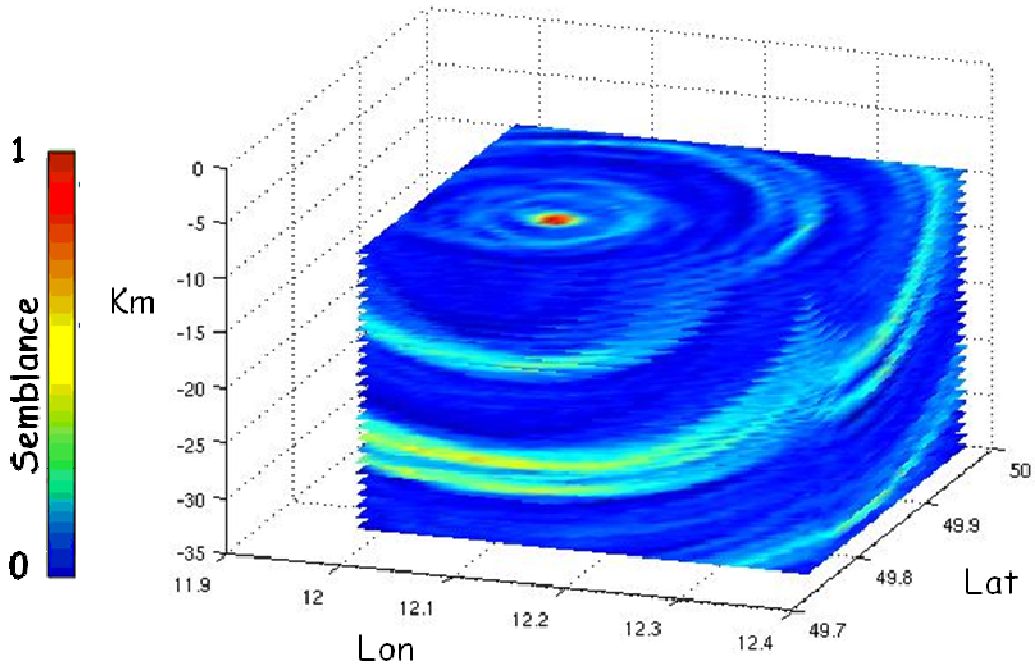

Figure 6.13: The same crustal volume as analyzed and represented in Fig. 6.12 observed from another view angle. The fans of travel-times are more marked.

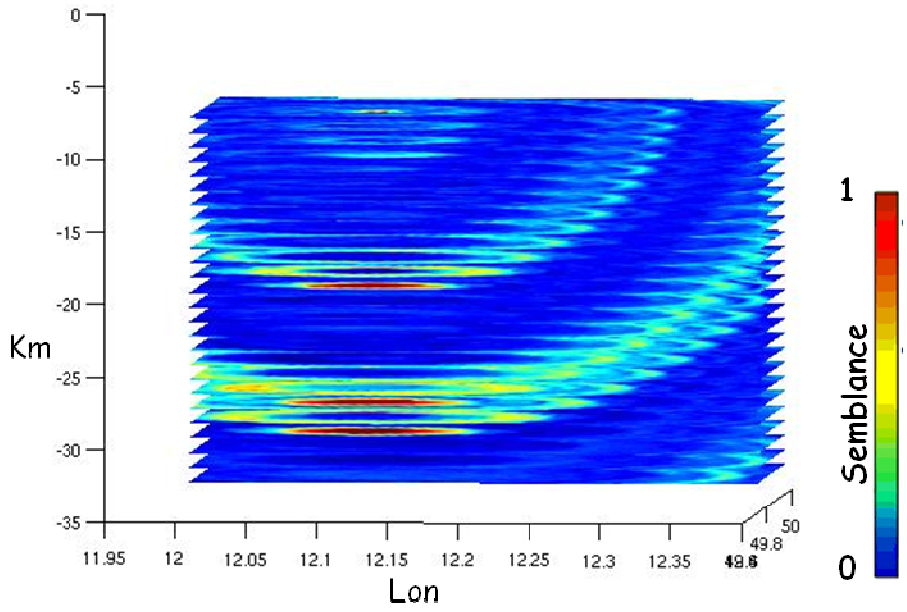

Figure 6.14: Frontal projection of the crustal volume of Fig. 6.12. The details of fans are outlined in frontal this perspective.

The yellow and light-blue coloured areas depict the fan patterns formed by the travel-times when starting to be coherent. A single snapshot at an initial time slice is shown, but looking at the semblance distribution for subsequent time steps allows the scanning of the overall time evolution. The same fans at later stages will become completely red, reaching the maximum of coherence.

6.6 Discussion of Results

The DBM method approach has been tested using synthetic data sets. By doing so, it is possible to separate method related artefacts (i.e. image smearing by "double array response") and real features. So far, the pictures and the final results obtained have been described in detail. As a conclusion, it can be observed that the semblance mapping of the preliminary results (Fig 5.2 and Fig. 5.3) were not appropriate. When plotting the first seconds after the source origin time the maximum of energy is expected to be localized in correspondence of the position and time of the source. Any deviation from this expectation must be contributed to the errors in the analysis code or parameters used in the processing or to problems when generating the synthetic data-set. By using the new data and a very simple scattering model the expected results have been obtained and the maximum of scattered energy has been correctly detected at the spatial and temporal position of the true source and the first-order discontinuities of the model. This is a stable observation for all the new-data analysis plots for a single time-slice close to the source origin time, in which the maximum of DBM energy-stack is observed at about 8 km, 20 km, 28 km and 30 km. At this initial time-slice, the maximum semblance areas do not show any focussing for depth larger than 20 km because coherence is not at maximum for all arrays. The focussing attains its maximum when all arrays involved in the analysis record the maximum coherence of travel-times. This will occur for larger depths at later time-slices, not shown here to simplify the analysis, ending up in a correct focussing at 33 km expected from the scattering model.

Concluding, the CAP-code focuses very well the scattering points in the crust both for source- and receiver-arrays and our approach to the DBM increases both the horizontal and vertical resolution. The tests of different array configurations demonstrated that the higher is the number of the arrays and the better is the suppression of noise and artefacts. Larger smearing effects are observed in the shallower crustal volume for the double-couple event, compared to the explosion case. Moreover, in the double-couple case, the energy focusing in the deeper part of the volume seems to become sharper by using a single PP-phase analysis rather than multiple phases. Contrarily, for shallow depths the energy focusing becomes sharper by multiple phases analysis. This is likely due to the effect of different phase polarities in the double-couple derived seismograms, which enter in the coherence. In order to resolve these smearing effects for the PP phases the upcoming CAP-code implementation will include the possibility to consider the radiation pattern and P-phase polarity, following a former application at SAFOD (Rentsch et al., 2010). Moreover, the resolution assessment and the application to the real data-set is in progress To this purpose an accurate 3D scattered model needs to be defined as input and a 3D ray-tracing software for theoretical travel-times computation is necessary.

CHAPTER 7

Conclusions

A 3D small scale analysis oriented to the investigation of the local crustal scattering structure has been performed for small source-receiver distances (spherical wavefront). To this scope, unconventional seismological tools such as the Double Beam Method (DBM; Krüger et al., 1993, 1996) and the Source-Scanning Algorithm (SSA; Kao & Shan, 2004) have been applied and originally implemented into the software package CAP (Continuous Array Processing; Ohrnberger 2004) in order to obtain images in both space and time of seismic sources and scattering points. While former studies have been performed at a global scale (Krüger et al., 1993; Scherbaum et al., 1997; Krüger et al., 2001), this is the second application of the DBM at the small scale of the crust, after Rietbrock & Scherbaum (1999). In this Thesis, the DBM has been applied by implementing a revised version of the Source-Scanning Algorithm (SSA; introduced by Kao & Shan, 2004). This algorithm exploits waveform information, including both relative amplitudes and arrival times, from an array of seismic stations, in order to determine whether or not a seismic source is present at a particular time and location. This is done by systematically scanning through a range of trial source locations and origin times. The new approach to the DBM is not applying the energy migration concept but computes the semblance value for each grid point of discretized hypothetic source volume using finite time-windows and fixed source times. A synthetic data-set has been produced to test the robustness of the code and the method implemented. The synthetic data-set and array geometry used are relative to the KTB-1994 experiment (Germany; Jost et al., 1998). As a result the coherence distribution (expressed in semblance) has been obtained through the whole study volume and mapped as a function of depth. The

resulting images can be seen as a (relative) joint log-likelihood of any point in the subsurface that have contributed to the full set of observed seismograms.

Concluding, the CAP-code focuses very well the scattering points in the crust both for source- and receiver-arrays. Furthermore, the present approach to the DBM increases both the horizontal and vertical resolution. Testing different array configurations has demonstrated that the higher is the number of the arrays and the better is the suppression of noise and artefacts. Different phase polarities of seismograms derived from the double-couple event are likely the cause of larger smearing effects of coherence in the shallower crustal volume, compared to the explosion case. In order to resolve these smearing effects for the PP phases the upcoming CAP-code implementation will include the possibility to consider the radiation pattern and P-phase polarity, following a former application at SAFOD (Rentsch et al., 2010). Moreover, the resolution assessment and the application to the real data-set is in progress. To this purpose, an accurate 3D scattered model needs to be defined as input and a 3D ray-tracing software for theoretical travel-times computation is necessary.

References

Aki K. & Richards P.G. (1980)."*Quantitative Seismology, Theory and Methods*". *I* and *II*, W. H. Freeman, New York.

Arlitt R., Kissling E., Ansorge J. and TOR Working Group (1999)."3-D crustal structure beneath the TOR array and effects on teleseismic wavefronts". *Tectonophysics*, 314, 309–319.

Baisch S., Bohnhoff M., Ceranna L., Yimin Tu, Harjes H.-P. (2002)." Probing the crust to 9 km depth: fluid-injection experiments and induced seismicity at the KTB superdeep drilling hole, Germany". *Bull. Seismol. Soc. Am.,* 92, 2369–2380, doi:10.1785/0120010236.

Bastow I., Stuart G., Kendall J., Ebinger C. (2005)."Upper-mantle seismic structure in a region of incipient continental breakup: northern Ethiopian rift". *Geophys. J. Int*., 162, 479–493.

Birtill J.W. & Whiteway F.E. (1965)."The application of phased arrays to the analysis of seismic body waves". *Phil. Trans. Royal Soc. of London*, Math. and Phys. Sciences A-258 (1091) 421-493.

Whiteway F.E.(1965)."The application of phased arrays to the analysis of seismic body waves". *Philos. Trans. R. Soc. London, Ser. A,* 258, 421–493.

Braun T., Schweitzer J., Azzara R.M., Piccinini D., Cocco M., Boschi E. (2004)."Results from the temporary installation of a small aperture seismic array in the Central Apennines and its merits for local event detection and location capabilities". *Annals of Geophys*., 47 (5), 1557-1568.

Braun T.; Dahm T.; Krüger F.; Ohrnberger M. & Scherbaum F. (2006)."Seismic array analysis of Tornillo-like signals recorded in Tuscany". *Atti 25° Convegno GNGTS.*

Braun T., Stammler K., Roselli P. (2007)."ELISA – Experimental Large Italian Seismic Array". GNGTS Atti del 26° Convegno Nazionale-Riassunti estesi.

Braun T. & Schweitzer J. (2008)." Spatial Noise-Field Characteristics of a Temporary Three-Component Small Aperture Array in Central Italy". *Bull. Seis. Soc. Am., 98*, 1876–1886.

Brudy M., Zoback M.D., Fuchs K., Rummel F. & Baumgärtner J. (1997)."Estimation of the complete stress tensor to 8 km depth in the KTB scientific drillholes implications for crustal strength". *J. Geophys. Res.*, 102, 18453-18475.

Bondar I., North R., Beall G. (1999). Teleseismic slowness-azimuth station corrections for the international monitoring system seismic network. Bull Seismol Soc Am 89:989–1003.

Büßelberg T., Harjes H.P., Knapmeyer M. (1995). "Source parameter of seismic events induced by fluid injection at 9 km depth in the KTB-borehole". *EOS*, 76, no. 46/supplement, F559.

Bungum H., Husebye E.S. & Ringdal F. (1971)."The NORSAR array and preliminary results of data analysis. *Geoph. J. R. astr. Soc*., 25, 115-126.

Buttkus B. (1986)."Ten years of the Gräfenberg array: defining the frontiers of broadband seismology". *Geologisches Jahrbuch* , E-35, Hannover, 135 pp.

Capon J. (1969)."High-resolution frequency-wavenumber spectrum analysis". Proc. IEEE, 57, 1408-1418.

References

Castle J.C. and Creager K.C. (1999)."A steeply dipping discontinuity in the lower mantle beneath Izu-Bonin. *J. Geophys. Res.*, 104, 7279–7292.
Carpenter E. (1965)."A historical review of seismometer array development .Proc IEEE 53: 1816-1821. Doi: 10.1109/PROC.1965.4452.

Clouser R. & Langston C. (1995)."Modeling P-Rg conversions from isolated topographic features near the NORESS array". *Bull. Seismol. Soc. Am.*, 85,859–873.

Crotwell H.P., Owens T.J., Ritsema J. (1999)."The TauP Toolkit: Flexible seismic travel-time and raypath utilities". *Seism. Res. Letters*, 70, 154-170.

Davies D., Kelly E., Filson J. (1971)."VESPA process for analysis of seismic signals". *Nat Phys. Sci.* (Lond) 232, 8-13.

Doornboos D.J. & Husebye E.S. (1972)."Array analysis of PKP phases and their precursors". *Phys. Earth Planet. Inter.*, 6, 387–399.

Douglas A. (2002)."Seismometer arrays—Their use in earthquake and test ban seismology". *Handbook of Earthquake and Engineering Seismology*, edited by P. Jennings, H. Kanamori, and W. Lee, 357–367, Academic, San Diego, Calif.

Douglas A., Bowers D., Marshall P.D., Young J.B., Porter D., and Wallis N.J. (1999)."Putting nuclear-test monitoring to the test". *Nature*, 398, 474–475.

Douze E.J. & Laster S.J. (1979)."Statics of semblance". *Geophysics*, 44, 1999-2003.

Emmermann R. & Lauterjung J. (1997)."The German Continental Deep Drilling Program KTB: Overview and major results". *J. Geophys. Res.*, 102(B8), 18,179– 18,201.

Friedrich A., Krüger F., Klinge K. (1998)."Ocean-generated microseismic noise located with the Grafenberg array". J. Seismol., 2, 47–64.

Frosch R.A. & Green P.E. Jr. (1966)."The concept of a large aperture seismic array". *Proc. Royal Soc.*, A-290, 368-384.

Goldstein P., Walter W.R., Zandt G. (1992)."Upper mantle structure beneath central Eurasia using a source array of nuclear explosions and waveforms at regional distances". *J. Geophys. Res., 97*, 14,097–14,115.

Haykin S. (1985)."Array signal processing". *Englewood Cliffs, NJ, Prentice-Hall, Inc.*, 493 pp, AA(McMaster University, Hamilton, Canada).

Harjes H.P. & Henger M. (1973)."Array-Seismologie". *Z. Geophs.*, 39, 865-905.

Harjes H.P. & Seidl D. (1978)."Digital recording and analysis of broad-band seismic data at the Gräfenberg (GRF-) array". *J. Geophys.*, 44, 511-523.

Harjes H.P., et al. (1997)."Origin and nature of crustal reflections: Results from integrated seismic measurements at the KTB super-deep drilling site". *J. Geophys. Res.*, 102(B8), 18,267– 18,288.

Haubrich R. (1968)."Array design". *Bull. Seismol. Soc. Am.*, 58, 977-991.

References

Henyey T. (2000)."Earthscope: a look into our continent". *Geotimes*, 45, 5.

Herrmann R.B. (1975)."A student's guide to the use of P and S-wave data for focal mechanism determination". *Earthquake Notes*, 46, 29-39.

Hirschmann G. (1996)."KTB—The structure of a Variscan terrane boundary: Seismic investigation-drilling-models". *Tectonophysics*, 264, 327 –339.
Ishii M., Shearer P.M., Houston H., Vidale J.E. (2005)."Extent, duration and speed of the 2004 Sumatra-Andaman earthquake imaged by the Hi-Net array". *Nature*, 435, 933-936.

Huang B.S. (2001)." Evidence for azimuthal and temporal variations of the rupture propagation of the 1999 Chi-Chi, Taiwan Earthquake from dense seismic array observations". *Geophys. Res. Lett*., 28 (17), 3377-3380.

Husebye E.S. & Ruud B.O. (1989)."Array seismology—Past, present and future developments. *Observatory Seismology*, edited by Litehiser J. J. , 123–153, Univ. of Calif. Press, Berkeley.

Johnson D.H., Dudgeon D.E. (1992)."Array signal processing: concepts and techniques". Simon & Schuster, New York.

Jost M.L., Büsselberg T., Jost Ö., Harjes H.P. (1998)."Source Parameters of injection-induced microearthquakes at 9 km depth at the KTB deep drilling site, Germany". *Bull Seis. Soc. Am*., 88(3), 815-832.

Kao H. & Shan S.-J. (2004)."The Source-Scanning-Algorithm: mapping the distribution of seismic sources in time and space". *Geophys. J. Int*., 157, 589-594.

Kao H., Shan S.-J., Dragert H., Rogers G., Cassidy J.F., Ramachandran K. (2005)."A wide depth distribution of seismic tremors along the northern Cascadia margin". *Nature,* 436, 841-844.

Kao H., Shan S.-J., Dragert H., Rogers G., Cassidy J.F., Wang K., James T.S., Ramachandran K. (2006)."Spatial-temporal patterns of seismic tremors in northern Cascadia". *J. Geophys. Res*., 111, B03309, doi:10.1029/2005JB003727.

Kao H. & Shan S.-J. (2007)."Rapid identification of earthquake rupture plane using Source-Scanning Algorithm". *Geophys. J. Int*., 168**,** 1011–1020.

Kárason H. & van der Hilst R.D. (2001)."Tomographic imaging of the lowermost mantle with differential times of refracted and diffracted core phases (*PKP*, *P*diff)". *J. Geophys. Res*., 106, 6569–6587.

Kennett B.L.N., Engdahl E.R., Buland R. (1995)."Constraints on seismic velocities in the Earth from travel times". *Geophys. J. Int*., 122, 108-124.

Kelly E.J. (1967)."Response of seismic signals to wide-band signals". *Lincoln Lab. Tech. Note 1967,* 30, Lincoln Lab., Mass. Inst. of Technol., Lexington, Mass.

Kito T. & Krüger F. (2001)."Heterogeneities in D" beneath the south-western Pacific inferred from scattered and reflected P-waves". *Geophys. Res. Lett*., 28, 2545–2548.

Kito T., Krüger F. Negishi H. (2004)."Seismic heterogeneous structure in the lowermost mantle beneath the southwestern Pacific". *J. Geophys. Res*., 109 (B9), B09304.

References

Krüger F., Weber M. (1992)."The effect of low-velocity sediments on the mislocation vectors of the GRF array". *Geophys. J. Int.*, 108, 387–393.

Krüger F., Weber M., Scherbaum F. & Schlittenhardt J. (1993)."Double beam analysis of anomalies in the core-mantle boundary region". *Geoph. Res. Lett.*, 20, 1475-1478.

Krüger F., Scherbaum F., Weber M., Schlittenhardt J. (1996)."Analysis of asymmetric multipathing with a generalization of the double-beam method". *Bull. Seismol. Soc. Am.*, 86, 737–749.

Krüger F., Baumann M., Scherbaum F. and Weber M. (2001)."Mid mantle scatterers near the Mariana slab detected with a double array method". *Geophys. Res. Lett.*, 28, 667–670.
Krüger F & Ohrnberger M. (2005)."Tracking the rupture of the Mw9.2 Sumatra earthquake over 1150 km at teleseismic distances". *Nature*, 435, 937-939, doi: 10.1038/nature03696.

Kværna T. & Doornbos D.J. (1986)."An integrated approach to slowness analysis with arrays and three-component stations". In: NORSAR Semiannual Technical Summary, 1 October 1985 – 31 March 1986, Scientific Report 2-85/86, NORSAR, Kjeller, Norway, 60-69.

Kværna T. & Ringda F. (1986)."Stability of various f-k estimation techniques". In: NORSAR Semiannual Technical Summary, 1 April 1986 – 30 September 1986, Scientific Report 1- 86/87, NORSAR, Kjeller, Norway, 29-40.

Kværna T. (1989)."On exploitation of small-aperture NORESS type arrays for enhanced P-wave detectability. *Bull. Seism. Soc. Am.*, 79, 888–900.

Martini N. & Stiller M. (1992). "Results of the ISO'89 experiment 'Durchschallung': recording of the vibrator sweeps of the 3D-seismics in the KTB borehole". *Niedersaechs. Landesamt Bodenforsch, Hannover, KTB-Report*, 92 (5), 233–246.

Mercier J., Bostock M., Audet P., Gaherty J., Garnero E., Revenaugh J. (2008)."The teleseismic signature of fossil subduction: northwestern Canada". *J. Geophys. Res.*, 113, B04308.

Mykkeltveit S., Åstebøl K., Doornbos D.J. & Husebye E.S. (1983)."Seismic array configuration optimization". *Bull. Seism. Soc. Am.* 73, 173-186.

Mykkeltveit S., Fyen J., Ringdal F.& Kværna T. (1988)."Spatial characteristics of the NORESS noise field and implications for array detection processing". *Phys. Earth Planet. Inter.*, 63, 277-283.

Neuberg J, Luckett R., Ripepe M. & Braun T. (1994)."Highlights from a seismic broadband array on Stromboli". *Geophys. Res. Lett., 21*, 749-752 .

Niazi M. (1969)."Use of source arrays in studies of regional structure". *Bull. Seismol. Soc. Am.*, 59,1631–1643.
Oldenburg D.W. (1981)."A comprehensive solution to the linear deconvolution problem". *Geophys. J. R. Astron. Soc.*, 65, 331–357.

Ohrnberger M., Bonnefoy-Claudet S., Cornou C., Guillier B., Kind F., Koehler A., Schissele-Rebel E., Savvaidiss A., Wathelet M. (2004)."User manual for software package CAP - a continuous array processing toolkit for ambient vibration array analysis". *SESAME* deliverable D18.06, SESAME EVG1- CT-2000-00026 project (http://sesame-fp5.obs.ujf-grenoble.fr).

References

Ødegaard E., Dooornbos D.J. & Kværna T. (1990)."Surface Topographic effects at arrays and three-component stations". *Bull. Seism. Soc. Am*., 80, 2214-2226.

Poupinet G., Ellsworth W.L., Frechet J. (1984)."Monitoring velocity variations in the crust using earthquake doublets: An application to the Calaveras fault, California". *J. Geophys. Res*., 89**,** 5719–5731.

Rabbel W., Beilecke T. Bohlen T., Fischer D., Frank A., Hasenclever J., Borm G.,2 Kück, Bram K., Druivenga G., Lüschen E., Gebrande H., Pujol J., Smithson S. (2004)." Superdeep vertical seismic profiling at the KTB deep drill hole (Germany): Seismic close-up view of a major thrust zone down to 8.5 km depth". *J. Geophys. Res.,* 109, B09309, doi:10.1029/2004JB002975.

Reasoner C. & Revenaugh J. (1999)."Short-period P wave constraints on D" reflectivity". *J. Geophys. Res*., 104, 955–961.

Rentsch S., Buske S., Gutjahr S., Kummerow J., Shapiro S.A. (2010)."Migration-based location of seismicity recorded with an array installed in the main hole of the San Andreas Fault Observatory at Depth (SAFOD)". *Geophys. J. Int.,* 182**,** 477–492.

Revenaugh J & Mendoza H. (1996)."Mapping shallow heterogeneity with teleseismic P to Rg scattered waves". *Bull. Seismol. Soc. Am.* 86, 1194–1199.

Rietbrock A. & Scherbaum F. (1999)."Crustal scattering at the KTB from a combined microearthquake and receiver analysis". *Geophys. J. Int*., 136, 57-67.

Ritter J.R.R., Jordan M., Christensen U. and Achauer U. (2001)."A mantle plume below the Eifel volcanic fields, Germany". *Earth Planet. Sci. Lett*., 186, 7–14.
Roecker S. (2001)."Constraints on the crust and upper mantle of the Kyrgyz Tien Shan from the preliminary analysis of GHENGIS broad-band seismic data". *Geologiya I Geofizika* , 42, 1554–1565.

Rost S. & Revenaugh J. (2001)."Seismic detection of rigid zones at the top of the core". *Science*, 294, 1911–1914.

Rost S. & Thomas C. (2002)."Array seismology: methods and applications". *Reviews of Geophysics*, 40, 1008-1035.

Rost S. & Garnero E. (2004)."Array seismology advances research into earth's interior". *EOS* 85(301), 305-306.
Rost S. & Thomas C. (2009)."Improving Seismic Resolution Throught Array Processing Tecniques". *Surv. Geophys*., 30, 271-299.

Rost S. (2010)."Seismic constraints on Ear". *Astronomy & Geophysics,* 51 (2), 2.26-2.32.

Saccorotti G., Di Lieto B., Tronca F., Fischione C., Scarpa R., Muscente R. (2006)."Performances of the UNDERground SEISmic array for the analysis of seismicity in Central Italy". *Annals of Geophys*, 49 (4/5), 1041-1057.

Saccorotti G. & Del Pezzo E. (2002)."A probabilistic approach to the inversion of data from a seismic array and its application to volcanic signals". *Geophys. J. Int*., 143, 249-261.

Scarpa R., Muscente R., Tronca F., Fischione C., Rotella P., Abril M., Alguacil G., De Cesare W., Martini M. (2004)."UNDERSEIS: The underground seismic array". *Seismol. Res. Lett*., 75, 493 504.

References

Shelly D.R., Beroza G.C., Satoshi I. (2007)."Non-volcanic tremor and low-frequency earthquake swarms". *Nature*, 446, 305-307.

Scherbaum F., Gillard D., Deichmann N. (1991)."Slowness power spectrum analysis of the coda composition of 2 microearthquake clusters in northern Switzerland". *Earth Planet. Inter.*, 67, 137–161.

Scherbaum F., Krüger F., Weber M. (1997)."Double beam imaging: mapping lower mantle heterogeneities using combinations of source and receiver arrays". *J. Geophys. Res.*, 102, 507–522.

Schweitzer J., Feyen J., Mykkeltveit S., Kværna T. (2002)."Seismic array: in new manual of seismological observatory practice – NMSOP". *IASPEI*, 481-532.

Snoke J.A., Munsey J.W., Teague A.G., Bollinger G.A. (1984)."A program for focal mechanism determination by combined use of polarity and SV-P amplitude ratio data". *Earthquake Notes*, 55, no. 3, 15.

Spudich P. & Cranswick E. (1984)."Direct observation of rupture propagation during the 1979 Imperial Valley earthquake using a short baseline accelerometer array". *Bull. Seism. Soc. Am.*; 74 (6), 2083-2114.

Spudich P. & Bostwick T. (1987)."Studies of the seismic coda using an earthquake cluster as deeply buried seismograph array". *J. Geophys. Res.*, 92, 10526-10546.

Stammler K. (1993)." Seismichandler—Programmable multichannel data handler for interactive and automatic processing of seismological analyses". *Computers & Geosciences,* 19 (2), 135-140.

Stammler K."Seismic Handler". Seismic Handler version 2.4h (05-May-2007), Copyright (C) 2006 Klaus Stammler, Seismological Observatory Graefenberg (SZGRF) http://www.seismic-handler.org/portal/wiki.

Tarenghi M. (2008)."The Atacama large millimetre/submillimeter array: overview and status". *Astrophys. Space Sci.*, 313, 1-7.

Thomas C., Weber M., Wicks C. and Scherbaum F. (1999)."Small scatterers in the lower mantle observed at German broadband arrays". *J. Geophys. Res.*, 104, 15,073–15,088.
Thomas C., Kendall J.M., Weber M. (2002)."Images of D" beneath northern Asia, 1, Multi-azimuth studies of heterogeneity". *Geophys. J. Int.*, 151 (1), 279–295.

Vidale J.E., Dodge D.A. and Earle P.S. (2000)."Slow differential rotation of the Earth's inner core indicated by temporal changes in scattering". *Nature*, 405, 445–448.

Wagner G.A., Coyle D.A., Duyster J., Henjes-Kunst F., Peterek A., Schrrder B., Stöckhert B., Wemmer K., Zulauf G. Ahrendt H., Bischoff R., Hejl E., Jacobs J., Menzel D., Lal N., Van Den Hante P., Vercoutere C. & Welzet B. (1997)."Post-Variscan thermal and tectonic evolution of the KTB site and its surroundings". *J. Geophys. Res.,* 102, 18221-18232.

Waldhauser F. & Ellsworth W.L. (2000)."A double-difference earthquake location algorithm: Method and application to the Northern Hayward Fault, California". *Bull. seism. Soc. Am.,* 90, 1353–1368.

References

Wang R. (1999)."A simple orthonormalization method for stable and efficient computation of Green's functions". *Bull. Seism. Soc. Am.*, 89 (3), 733–741.

Weber M., Davis J.P., Thomas C., Krüger F., Scherbaum F., Schlittenhardt J. and Körnig M. (1996)."The structure of the lowermost mantle as determined from using seismic arrays. *Seismic Modeling of the Earth's Structure*, edited by Boschi E., Ekström G. and Morelli A., 399–442, Instit. Naz. di Geophys., Rome.

Wessel P. & Smith W.H.F. (1998)."New, improved version of the Generic Mapping Tools Released". *EOS Trans. AGU*, 79, 579.

Whiteway F. E. (1966)."The use of arrays for earthquake seismology". *Proc. R. Soc. London, Ser. A*, 290, 328–342.

Williams E., Maynard J., Skudrzyk E. (1980)."Sound source reconstructions using a microphone array". *J. Acoust. Soc. Am.*, 68, 340-344.

Wright C. (1972)."Array studies of seismic waves arriving between *P* and *PP* in the distance range 90 to 115. *Bull. Seismol. Soc. Am.*, 62, 385–400.

Zoback M.D. & Harjes H.P. (1997)."Injection-induced earthquakes and crustal stress at 9 km depth at the KTB deep drilling site, Germany". *J. Geophys. Res.,* 102**,** 18,477-18,491.

Zhou H.W. (1994)."Rapid three-dimensional hypocentral determination using a master station method". *J. Geophys. Res.*, 99, 15 439–15 455.

References

Appendix

CHAPTER 5

Input files for QSEIS

Example Input-file for QSEIS for A100-array explosion:

```
# This is the input file of FORTRAN77 program "qseis5.5" for calculation of
# synthetic seismograms based on a layered halfspace earth model.
#
# by
# Rongjiang  Wang <wang@gfz-potsdam.de>
# GeoForschungsZentrum Potsdam
# Telegrafenberg, D-14473 Potsdam, Germany
#
# first written: Potsdam, Aug 19, 1997
# Last modified: Potsdam, June 2, 2006
#
# = = = = = = = = = = = = = = = = = = = = = = = = = = = = = = = = = = = = = = = =
# If not specified, SI Unit System is used overall!
#
# Coordinate systems:
# cylindrical (z,r,t) with z = downward,
#                          r = from source outward,
#                          t = azmuth angle from north to east;
# cartesian (x,y,z) with   x = north,
#                          y = east,
#                          z = downward;
# = = = = = = = = = = = = = = = = = = = = = = = = = = = = = = = = = = = = = = = =
#
#      SOURCE PARAMETERS
#      =================
# 1. source depth [km]
#--------------------------------------------------------------------------------
 7.9               |dble: source_depth;
#--------------------------------------------------------------------------------
#
#      RECEIVER PARAMETERS
#      ===================
# 1. receiver depth [km]
# 2. switch for distance sampling role (1/0 = equidistant/irregular); switch
#    for unit used (1/0 = km/deg)
# 3. number of distance samples
# 4. if equidistant, then start and end trace distance (> 0); else distance
#    list (please order the receiver distances from small to large)
# 5. (reduced) time begin [sec] & length of time window [sec], number of time
#    samples (<= 2*nfmax in qsglobal.h)
# 6. switch for unit of the following time reduction parameter: 1 = velocity
#    [km/sec], 0 = slowness [sec/deg]; time reduction parameter
#--------------------------------------------------------------------------------
# A111,A110,A100,A112
 0.000                 |dble: receiver_depth;
 0  1                  |int: sw_equidistant, sw_d_unit;
 4                     |int: no_distances;
 1.34867,1.44278,1.47153,1.53687   |dble: d_1,d_n; or d_1,d_2, ...(no comments in
between!);
 -1.0  19.46 2048      |dble: t_start,t_window; int: no_t_samples;
 1  0.0                |int: sw_t_reduce; dble: t_reduce;
#--------------------------------------------------------------------------------
#
#      WAVENUMBER INTEGRATION PARAMETERS
#      =================================
# 1. select slowness integration algorithm (0 = suggested for full wave-field
#    modelling; 1 or 2 = suggested when using a slowness window with narrow
```

Appendix

```
#    taper range - a technique for suppressing space-domain aliasing);
# 2  4 parameters for the low and high slowness cut-offs [s/km] with tapering:
#    slw1 <= slw2 defining the cosine taper at the lower end, and slw3 <= slw4
#    defining the cosine taper at the higher end. if the given slowness cut-
#    offs are all zero of inconsistent with each other, then their default
#    values for the full wave solution will be considered (that possibly
#    results in very large computation time)
# 3. parameter for sampling rate of the wavenumber integration (1 = sampled
#    with the simple Nyquist frequency, 2 = sampled as twice as the Nyquist,
#    and so on: the larger this parameter, the smaller are the spatial
#    aliasing efects, but also the more computation effort);
# 4. the factor for suppressing time domain aliasing (> 0 and <= 1) (Note 1).
#-------------------------------------------------------------------------------
 0                                  |int: sw_algorithm;
 0.000  0.000  0.000  0.000         |dble: sw_cut_off, slw(1-4);
 8.00                               |dble: sample_rate;
 0.1                                |dble: supp_factor;
#-------------------------------------------------------------------------------
#
#               OPTIONS FOR PARTIAL SOLUTIONS
#       (only applied to the source-site structure)
#          ============================================
#
# 1. switch for filtering free surface effects (0 = with free surface, i.e.,
#    do not select this filter; 1 = without free surface; 2 = without free
#    surface but with correction on amplitude and wave form. Note switch 2
#    can only be used for receivers at the surface)
# 2. switch for filtering waves with a shallow penetration depth (concerning
#    their whole trace from source to receiver), penetration depth limit [km]
#
#    if this option is selected, waves whose travel path never exceeds the
#    given depth limit will be filtered ("seismic nuting"). the condition for
#    selecting this filter is that the given shallow path depth limit should
#    be larger than both source and receiver depth.
#
# 3. number of depth ranges where the following selected up/down-going P or
#    SV waves should be filtered
# 4. the 1. depth range: upper and lower depth [km], switch for filtering P
#    or SV wave in this depth range:
#
#    switch no:              1      2        3       4         other
#    filtered phase:         P(up)  P(down)  SV(up)  SV(down)  Error
#
# 5. the 2. ...
#
#    The partial solution options are useful tools to increase the numerical
#    significance of desired wave phases. Especially when the desired phases
#    are smaller than the undesired phases, these options should be selected
#    and carefully combined.
#-------------------------------------------------------------------------------
 0                           |int: isurf;
 0   0.000                   |int: sw_phase_filter; dble:shallow_depth_limit;
 0                           |int: no_of_depth_ranges;
# 0.0 0.4  3
# 0.0 0.4  4
#-------------------------------------------------------------------------------
#
#       SOURCE TIME FUNCTION (WAVELET) PARAMETERS (Note 2)
#       ================================================
# 1. wavelet duration [unit = time sample rather than sec!], that is about
#    equal to the half-amplitude cut-off period of the wavelet (> 0. if <= 0,
#    then default value = 2 time samples will be used), and switch for the
#    wavelet form (0 = user's own wavelet; 1 = default wavelet: normalized
#    square half-sinusoid for simulating a physical delta impulse; 2 = tapered
#    Heaviside wavelet, i.e. integral of wavelet 1)
# 2. IF user's own wavelet is selected, then number of the wavelet time samples
#    (<= 1024), and followed by
# 3. equidistant wavelet time samples
# 4  ...(continue) (! no comment lines allowed between the time sample list!)
#    IF default, delete line 2, 3, 4 ... or comment them out!
#-------------------------------------------------------------------------------
 10   1                        |int:dble: wavelet_duration; sw_wavelet;
```

Appendix

```
# 100                            |int: no_w_samples; below dble: w_samples;
#  0.000  0.063  0.127  0.189  0.251  0.312  0.372  0.430  0.486  0.541
#  0.593  0.643  0.690  0.735  0.776  0.815  0.850  0.881  0.910  0.934
#  0.955  0.972  0.985  0.994  0.999  1.000  0.997  0.990  0.979  0.964
#  0.945  0.922  0.896  0.866  0.833  0.796  0.756  0.713  0.667  0.618
#  0.567  0.514  0.458  0.401  0.342  0.282  0.220  0.158  0.095  0.032
# -0.032 -0.095 -0.158 -0.220 -0.282 -0.342 -0.401 -0.458 -0.514 -0.567
# -0.618 -0.667 -0.713 -0.756 -0.796 -0.833 -0.866 -0.896 -0.922 -0.945
# -0.964 -0.979 -0.990 -0.997 -1.000 -0.999 -0.994 -0.985 -0.972 -0.955
# -0.934 -0.910 -0.881 -0.850 -0.815 -0.776 -0.735 -0.690 -0.643 -0.593
# -0.541 -0.486 -0.430 -0.372 -0.312 -0.251 -0.189 -0.127 -0.063  0.000
#-------------------------------------------------------------------------------
#
#       FILTER PARAMETERS OF RECEIVERS (SEISMOMETERS OR HYDROPHONES)
#       ===========================================================
# 1. constant coefficient (normalization factor)
# 2. number of roots (<= nrootmax in qsglobal.h)
# 3. list of the root positions in the complex format (Re,Im). If no roots,
#    comment out this line
# 4. number of poles (<= npolemax in qsglobal.h)
# 5. list of the pole positions in the complex format (Re,Im). If no poles,
#    comment out this line
#-------------------------------------------------------------------------------
 1.0
 0
# (0.0, 0.0), (0.0, 0.0)
 0
# (-4.35425, 4.44222), (-4.35425,-4.44222)
#-------------------------------------------------------------------------------
#
#      OUTPUT FILES FOR GREEN'S FUNCTIONS (Note 3)
#      ===========================================
# 1. selections of source types (yes/no = 1/0)
# 2. file names of Green's functions (please give the names without extensions,
#    which will be appended by the program automatically: *.tz, *.tr, *.tt
#    and *.tv are for the vertical, radial, tangential, and volume change (for
#    hydrophones) components, respectively)
#-------------------------------------------------------------------------------
#  explosion   strike-slip dip-slip   clvd       single_f_v  single_f_h
#-------------------------------------------------------------------------------
   1           1           1          1          1           1         |int
   'ex-l'      'ss-l'      'ds-l'     'cl-l'     'fz-l'      'fh-l'    |char
#-------------------------------------------------------------------------------
#      OUTPUT FILES FOR AN ARBITRARY POINT DISLOCATION SOURCE
#            (for applications to earthquakes)
#      ===================================================
# 1. selection (yes/no = 1/0), the 6 moment tensor components [N*m]: Mxx, Myy,
#    Mzz, Mxy, Myz, Mzx (x is northward, y is eastward and z is downard)
# 2. switch for azimuth distribution of the stations (0 = uniform azimuth,
#    else = irregular azimuth angles)
# 3. list of the azimuth angles [deg] for all stations given above (if the
#    uniform azimuth is selected, then only one azimuth angle is required)
#
#    Note: to use this option, the Green's functions above should be computed
#          (selection = 1) if they do not exist already.
#
#                 north(x)
#                  /
#                 /\ strike
#                *------------------------>  east(y)
#                |\                         \
#                |-\                         \
#                |  \     fault plane         \
#                |90 \                         \
#                |-dip\                         \
#                |     \                         \
#                |      \                         \
#           downward(z)  \-----------------------\
#
#-------------------------------------------------------------------------------
#     Mxx         Myy         Mzz         Mxy         Myz         Mzx        File
#-------------------------------------------------------------------------------
```

Appendix

```
#  1  -0.61E+09  -0.02E+09   0.64E+09  0.61E+09    0.35E+09   0.34E+09   'seis-l'
  1  1.0E+09      1.0E+09   1.0E+09     0.E+09      0.E+09     0.E+09   'seis-l'
  1
 79.74,81.90,86.09,89.72
#-------------------------------------------------------------------------------
#
#       GLOBAL MODEL PARAMETERS (Note 4)
#       ================================
# 1. switch for flat-earth-transform
# 2. gradient resolution [%] of vp, vs, and ro (density), if <= 0, then default
#    values (depending on wave length at cut-off frequency) will be used
#-------------------------------------------------------------------------------
 0                              |int: sw_flat_earth_transform;
 0.0  0.0  0.0                  |dble: vp_res, vs_res, ro_res;
#-------------------------------------------------------------------------------
#
#                       LAYERED EARTH MODEL
#       (SHALLOW SOURCE + UNIFORM DEEP SOURCE/RECEIVER STRUCTURE)
#       ========================================================
# 1. number of data lines of the layered model (source site)
#-------------------------------------------------------------------------------
 6                             |int: no_model_lines;
#-------------------------------------------------------------------------------
#
#       MULTILAYERED MODEL PARAMETERS (source site)
#       ===========================================
# no  depth[km]  vp[km/s]  vs[km/s]  ro[g/cm^3] qp      qs
#-------------------------------------------------------------------------------
  1      0.000   5.0000    3.0000    2.7000      300.0   60.0
  2     20.000   5.0000    3.0000    2.7000      300.0   60.0
  3     20.000   6.5000    3.7000    2.9000      300.0   60.0
  4     33.000   6.5000    3.7000    2.9000      300.0   60.0
  5     33.000   7.8000    4.4000    3.3000      300.0   60.0
  6     40.000   7.8000    4.4000    3.3000      300.0   60.0

#-------------------------------------------------------------------------------
#
#                LAYERED EARTH MODEL
#       (ONLY THE SHALLOW RECEIVER STRUCTURE)
#       =====================================
# 1. number of data lines of the layered model
#
#    Note: if the number = 0, then the receiver site is the same as the
#          source site, else different receiver-site structure is considered.
#          please be sure that the lowest interface of the receiver-site
#          structure given given below can be found within the source-site
#          structure, too.
#
#-------------------------------------------------------------------------------
 0                              |int: no_model_lines;
#-------------------------------------------------------------------------------
#
#       MULTILAYERED MODEL PARAMETERS (shallow receiver-site structure)
#       ===============================================================
# no  depth[km]    vp[km/s]    vs[km/s]   ro[g/cm^3]   qp      qs
#-------------------------------------------------------------------------------
#--------------------------------end of all inputs------------------------------
```

Note 1:

The suppression of the time domain aliasing is achieved by using the complex frequency technique. The suppression factor should be a value between 0 and 1. If this factor is set to 0.1, for example, the aliasing phase at the reduced time begin is suppressed to 10%.

Note 2:

The default basic wavelet function (option 1) is (2/tau)*sin^2(pi*t/tau), for 0 < t < tau, simulating physical delta impuls. Its half-amplitude cut-off frequency is 1/tau. To avoid high-frequency noise, tau should not be smaller than 4-5 time samples.

Appendix

```
Note 3:

  Double-Couple   m11/ m22/ m33/ m12/ m23/ m31  Azimuth_Factor_(tz,tr,tv)/(tt)
  ========================================================================
  explosion       1.0/ 1.0/ 1.0/ -- / -- / --       1.0         /   0.0
  strike-slip     -- / -- / -- / 1.0/ -- / --       sin(2*azi)  /   cos(2*azi)
                  1.0/-1.0/ -- / -- / -- / --       cos(2*azi)  /  -sin(2*azi)
  dip-slip        -- / -- / -- / -- / -- / 1.0      cos(azi)    /   sin(azi)
                  -- / -- / -- / -- / 1.0/ --       sin(azi)    /  -cos(azi)
  clvd           -0.5/-0.5/ 1.0/ -- / -- / --       1.0         /   0.0
  ========================================================================
  Single-Force    fx / fy / fz                  Azimuth_Factor_(tz,tr,tv)/(tt)
  ========================================================================
  fz              -- / -- / 1.0                       1.0      /   0.0
  fx              1.0/ -- / --                        cos(azi) /   sin(azi)
  fy              -- / 1.0/ --                        sin(azi) /  -cos(azi)
  ========================================================================

Note 4:

Layers with a constant gradient will be discretized with a number of homogeneous
sublayers. The gradient resolutions are then used to determine the maximum
allowed thickness of the sublayers. If the resolutions of Vp, Vs and Rho
(density) require different thicknesses, the smallest is first chosen. If this
is even smaller than 1% of the characteristic wavelength, then the latter is
taken finally for the sublayer thickness.
```

Input-files for CAP

Example of mig-z-file:

```
    ********** processing settings ************************

    METHOD     16             # select method of processing:
                        0: CVFK        # Conventional FK after Kvaerna and Ringdahl, 1986
                                       # Sliding window analysis - Semblance based
                        1: CVFK2       # Conventional FK Beampower analysis
                                       # From average complex cross spectral matrix
                        2: CAPON       # Capon's high-resolution FK
                                       # From average complex cross spectral matrix
                        3: SLANTSTACK  # SLANTSTACK analysis steered on single azimuth
                                       # Stacked average of shifted FFT's
                                         <--- was deleted once, but will be
                                              reconsidered asap
                        4: MSPAC       # Modified SPAC
                                       # Sliding window analysis
                        5: MUSIC       # MUltiple SIgnal Classification
                                       # Sliding window analysis
                        6: MUSIC2      # MUltiple SIgnal Classification
                                       # From average complex cross spectral matrix
                        7: HTOV        # computes H/V ratios for given stations
                                       # and array/network-wide average
                                         <--- not yet implemented

                        # methods for pre-selection of ''useful'' time windows
                        # output used as input for methods 0, 3(?), 4, 6(?)
                        8: CHECK_EIGSPEC# pre-selection method
                        9: HYPTEST     # hypothesis testing for pre-selection
                                       # allows combinations of hypothesis testing
                                       # routines as specified by HYPMETH

                        # experimental methods, not fully tested/explored
                        10: CCSTACK    # simple CC-stacks between stations
                                       # can be used for ZZ stacks only or
                                       # for all combinations (COMP keyword)
                        11: QEST       # window based estimation of attenuation
```

Appendix

```
                                # according to Ph.D. Thesis by Daren Zywicki
                    12: CHOETAL    # paper from Cho et al. 2003/4

********** submethods for HYPTEST **********************

HYPMETH             0       # selects method(s) for hypothesis testing
                    # argument: list of integer separated by '+' signs
                    # e.g. 0+3+4
                    0: t-f pol.-analysis (array-wide, Jurkevics, 1988)
                    1: pol.-model test Christofferson et al., 1988
                    2: pol.-analysis Vidale, 1986
                    3: t-f 3-C complex trace analysis (Rene et al., 1986)
                    4: t-f energy criteria (ridge+energy, Schissele, 2002)
                    5: t-f smoothed phase stack (Schimmel ++ )
                    6: t-f cross analytic signal coherence measure
                    # so far, only option 4 is implemented

********** threshold list for submethods of HYPTEST ****

TFPOLJURK_TH1       0.9     <- not yet implemented
TFPOLJURK_TH2       0.      <- not yet implemented

PAMLTEST_TH1        xx      <- not yet implemented
PAMLTEST_TH2        xx      <- not yet implemented

PAVIDALE_TH1        xx      <- not yet implemented
PAVIDALE_TH2        xx      <- not yet implemented

TFCOMPLEX_TH1       xx      <- not yet implemented
TFCOMPLEX_TH2       xx      <- not yet implemented

TFENERGY_TH1        0.01    <- relative energy threshold per freq. band
TFENERGY_TH2        0.8     <- percentage of array stations contributing

TFSCHIMMEL_TH1      xx      <- not yet implemented
TFSCHIMMEL_TH2      xx      <- not yet implemented

TFXANSIG_TH1        xx      <- not yet implemented
TFXANSIG_TH2        xx      <- not yet implemented

********** applies just for CVFK and CCSTACK method ****************

PREWHITEN       0       # toggle prewhitening on or off
                        0: toggles off
                        1: toggles on

********** applies just for CVFK method in the moment **************

DETECT_DOMINANT     0       # toggles detection of single dominant signal
                    # in current window by determination of
                    # eigenspectra characteristics - needs SINGVAL_RATIO

SINGVAL_RATIO       10.     # ratio of first to second eigenvalue
                    # from eigenvalue decomposition of covariance matrix

SLOWRESP    0       # computes slowness response for ideal harmonic waves
                    # centered on previously determined fk-maximum
                    # May be used for postprocessing, but slows down
                    # processing speed

****** applies to CVFK(2), CAPON, MUSIC(2) and MSPAC ********

NUM_BANDS   1       # number of bands for FK or MSPAC

LOWEST_CFREQ        0.05    # center frequency of lowest band

HIGHEST_CFREQ       0.21    # center frequency of lowest band

BANDWIDTH   0.8     # half bandwidth of CVFK or MSPAC bands as fraction of
                    # center frequency - filter (1-bw)*fc <-> (1+bw)*fc

BANDSTEP    -1.     # factor used to multiply center frequency in order to
```

Appendix

```
                  # get to next higher center frequency
                    <-- if set to negative values, BANDSTEP is determined
                        from HIGHES/LOWEST_CFREQ and NUM_BANDS

********* applies to CAPON and MUSIC(2) ********

SPATIAL_SMOOTH    0       # toggle spatial smoothing
                  0: toggles off
                  1: toggles on

******** applies only for MUSIC(2) methods ****************

NSRC_SELECT       0       # selection of number of sources
                  negative integer: use full solution from nsrc = 1 .... M-1
                  0: automatic determination with AIC
                  positive integer .lt. M-1: fixed number of sources
                    <--- not yet used - still full solution & akaike for info!

******** applies only for MSPAC method ****************

RING_SELECT       0       # ring selection method
                  0: automatic selection
                  1: manual selection by expert
                     <--- stops processing and writes out coarray
                          waits for selection and proceeds
                          (this is the intention - QT based in any case)

*** applies for MSPAC inversion scheme - may be unnecessary inf future ********

OMEGA             -1.     # smoothing for a priori gauss distribution
                  # of model parameters for MSPAC dispersion curve
                  # inversion - if set less than 0 - a priori
                  # information is set to unity matrix

APRIORI           1.      # standard deviation of a priori distribution
                  # of model parameters for MSPAC dispersion curve
                       # inversion - if OMEGA is set less than 0
                       # this parameter is not used...

CR@1HZ            0.6     # cR(2*PI*f) at f = 1 Hz, Rayleigh wave velocity at 1 Hz
                  # for initial dispersion curve model (MSPAC)

CREXP             0.1     # exponent for initial dispersion curve model
                  # c(2*PI*f) = c(1)*(2*PI*f)^-CREXP

LAMBDA_MIN 0.1    # use this to determine valid max freq. for
                  # mspac inversion scheme (fraction of wavelength)

LAMBDA_MAX 0.5    # use this to determine valid min freq. for
                  # mspac inversion scheme... (fraction of wavelength)

***** applies to all grid dependent computations *****************
      CVFK(2), CAPON, MUSIC(2), SLANTSTACK

GRID_LAYOUT       0       # select grid layout
                  0: POLAR
                  1: CARTESIAN
                  2: LINEAR
                     <--- provided by M. Wathelet
                          for similar functionality as SLANTSTACK
                          here semblance-based, SLANTSTACK power-based

GRID_TYPE  0      # select grid type
                  0: equidistant sampling in SLOWNESS
                  1: equidistant sampling in APPARENT VELOCITY
                     <--- option 1 NOT recommended

GRID_RESOL 301    # number of grid points in sampling direction
                  # for cartesian grid used for x, y coordinate axis
                  # for polar grid layout used for radial axis

GRID_MAX       0.3# maximum of grid either app. vel. or slowness
```

Appendix

```
                    # for cartesian grid [-GRID_MAX,GRID_MAX]
                    # for polar grid [0,GRID_MAX]
                      <--- note: polar grids are sampled 2 times better
                                 for same GRID_RESOL compared to cartesian grids
                    slowness/app.vel. resolution polar: GRID_MAX/(GRID_RESOL-1)
                    slowness/app.vel. resolution cartesian: 2*GRID_MAX/(GRID_RESOL-1)

NPHI                360     # number of azimuthal steps for polar grid layout
                      <--- Azimuth resolution = 360/NPHI

LINEAR_PHI 220.     # Backazimuth for steering in case of LINEAR GRID_LAYOUT
                    # value is given in DEGREES -
                    # value is the backazimuth usual convention (N == 0., E == 90.)

MAPFRAC             0.00001 # percentage of highest fk-map values dumped to output

********* applies to CCSTACK method ***************************

NSTACK              5000

SEED                0       # 0 will select some seed from system clock,
                    # any other value will be used
                    # used as fixed seed to start the random number
                    # generator

********* applies to all methods *******************************

COMP                1       # select component to process
                    1: vertical component Z
                    2: north component N
                    3: east component E
                    22: radial component R
                    33: transverse component T
                    123: all three components

WINFAC              -5.0    # window length is adjusted to center frequency
                    # of processed frequency band FCENT -
                    # window length is set to:
                    # WINLEN = WINFAC * 1./FCENT
                    # WINFAC set to positive value OVERRIDES
                    # settings for WINLEN and STEP!
                    # Turned off if WINFAC < 0

OVERLAP             -1      # selects amount of overlap depending
                    # on center frequency:
                    # 0 -> STEP = 0.5*WINLEN(HIGHEST_CFREQ)
                    #   ---> may cause highly oversampled
                    #        processing for lower freqs.
                    #   ---> causes long processing times
                    # 1 -> STEP = 0.5*WINLEN(LOWEST_CFREQ)
                    #   ---> may cause gaps in data processing
                    #        for higher freqs.
                    # 0 < OVERLAP < 1
                    #   -> STEP approx.
                    #   0.5*WINLEN(OVERLAP*(HIGHEST_CFREQ-LOWEST_FREQ))
                    #   ---> some compromise in OVERLAP
                    # OVERLAP < 0 -> uses STEP = 0.5*WINLEN(FCENT)
                    #   ---> 50% overlap in all freq. bands

WINLEN              0.2     # window length in seconds
                    # fixed window length for all frequency bands
                    # if WINFAC is set to negative values

STEP                0.1     # forward step in seconds
                    # only used if fixed window length is selected
                    # (WINFAC set to negative values)

TAPER_FRAC 0.2      # fraction for cosine taper
                    # used for all FFT computations

********** applies for SLANTSTACK and HTOV ******
```

Appendix

```
POWSPEC            0       # flag whether power spectrum is calculated by
                   # stacking windows or smoothing in spectral domain
                   0: window stacking
                   1: smoothing in Fourier domain

********** applies just for HTOV ******

KOSMOOTH   30      # smoothing parameter b for smoothing window after
                   # Konno & Ohmachi 1998

********** applies just for SLANTSTACK ******

STRIKE             -1.     # strike of line for slantstack analysis
                   # values < 0 indicates use of regression result
                   # from linear array configuration
                   # values >= 0 are interpreted as the LINEAR_PHI parameter

******** I/O settings *********************************

OUTPUT_FILE        test.out       # basename of output file -
                          # extensions are added for output files

OFILE_TYPE         0       # flag for output file type
                   0: write out ASCII file
                   1: write out BINARY file
                      ---> header is always ascii

WRITE_TRACES       1       # flag if preprocessed traces should be written out
                   # used for finding errors in preprocessing steps
                   0: don't write out preprocessed traces
                   1: write out preprocessed traces

******** preprocessing parameters **********************

DECIMATE   1       # integer decimation factor - .leq. 1 turns off

UPSAMPLING 4       # upsampling the original traces

SEIDL              0       # flag for instrument simulation
                   0: don't simulate common instrument response
                   1: simulate common instrument response
                      <--- requires instrument response files in GSE1.0 PAZ format
                           just applicable for GIANT-based processing

FSIM               0.002   # corner frequency of simulated instrument

HSIM               0.707   # fraction of crit. damping of simulated instrument

BBP_FILTER 0       # flag for butterworth bandpass filtering
                   0: don't filter
                   1: filter

BBP_LOW            1.00    # lower corner frequency for butterworth bandpass

BBP_HIGH   30.0    # upper corner frequency for butterworth bandpass

BBP_ORDER  2       # number of sections for butterworth bandpass
                     <--- remember: 1 section contains 1 conjugate complex pole pair

ZERO_PHASE 0       # flag for zero phase filtering
                   0: just forward filtering
                   1: zero phase filter - forward/backward filtering
                      <--- doubles number of sections!

GAUSSNOISE 0.05    # if value .lt. 0 then gaussian noise is added to all traces
                   # GAUSSNOISE specifies the standard deviation of gaussian noise
                   # as a fraction of the standard deviation computed for
                   # each individual trace
                   # allows to control fixed signal to noise ratios for
                   # stationary signals

******** more specialized parameters **********************
```

Appendix

```
TIME_CORR  0       # flag if time corrections have to be applied
                   0: don't need time correction
                   1: need time correction

3DCORRECT  0       # flag whether 3D array geometry is evaluated
                   0: option turned off
                   1: best plane fitted to 3D geometry of array
                   # Comment: this option is only reasonable for arrays
                   # set up on steep slopes, however directions are then
                   # calculated with respect to the gradient of the best
                   # fitting plane -> this is no longer a ZNE coordinate system!
```

Example of station.slist-file:

```
A100 BHZ 12.1251 49.828833 492 MARK3K.cal
A100 BHN 12.1251 49.828833 492 MARK3K.cal
A100 BHE 12.1251 49.828833 492 MARK3K.cal
A110 BHZ 12.128583 49.828367 503 MK3.cal
A111 BHZ 12.123717 49.8277 481 MK3.cal
A112 BHZ 12.121983 49.829283 490 MK3.cal

A200 BHZ 12.1334 49.815783 512 MARK3K.cal
A200 BHN 12.1334 49.815783 512 MARK3K.cal
A200 BHE 12.1334 49.815783 512 MARK3K.cal
A210 BHZ 12.136883 49.815683 504 MK3.cal
A211 BHZ 12.13215 49.81465 502 MK3.cal
A212 BHZ 12.133417 49.81735 500 MK3.cal

A300 BHZ 12.110817 49.811983  .cal
A300 BHN 12.110817  49.811983  .cal
A300 BHE 12.110817  49.811983  .cal
A310 BHZ 12.111517  49.81355   .cal
A311 BHZ 12.111433  49.8104    .cal
A312 BHZ 12.107417  49.811483  .cal

A400 BHZ 12.1107 49.820967 515 S13.cal
A400 BHN 12.1107 49.820967 515 S13.cal
A400 BHE 12.1107 49.820967 515 S13.cal
A410 BHZ 12.11035 49.822717 480 S13.cal
A411 BHZ 12.113133 49.820967 502 S13.cal
A412 BHZ 12.110617 49.819483 515 S13.cal

B100 BHZ 12.114167 49.861167 490 MARK3K.cal
B100 BHN 12.114167 49.861167 490 MARK3K.cal
B100 BHE 12.114167 49.861167 490 MARK3K.cal
B110 BHZ 12.113167 49.863667 495 MARK3K.cal
B110 BHN 12.113167 49.863667 495 MARK3K.cal
B110 BHE 12.113167 49.863667 495 MARK3K.cal
B111 BHZ 12.114833 49.856 490 MARK3K.cal
B111 BHN 12.114833 49.856 490 MARK3K.cal
B111 BHE 12.114833 49.856 490 MARK3K.cal
B112 BHZ 12.1115 49.862167 505 GEOPH.cal
B120 BHZ 12.117667 49.865833 525 GEOPH.cal
B121 BHZ 12.123 49.861167 531 GEOPH.cal
B122 BHZ 12.116333 49.856 477 GEOPH.cal
B123 BHZ 12.1055 49.861 498 GEOPH.cal
B124 BHZ 12.108333 49.8665 515 MARK3K.cal
B124 BHN 12.108333 49.8665 515 MARK3K.cal
B124 BHE 12.108333 49.8665 515 MARK3K.cal

B200 BHZ 12.190667 49.829833 445 MARK3K.cal
B200 BHN 12.190667 49.829833 445 MARK3K.cal
B200 BHE 12.190667 49.829833 445 MARK3K.cal
B210 BHZ 12.191167 49.831333 445 MARK3K.cal
B210 BHN 12.191167 49.831333 445 MARK3K.cal
```

Appendix

```
B210 BHE 12.191167 49.831333 445 MARK3K.cal
B211 BHZ 12.194167 49.8285 450 MARK3K.cal
B211 BHN 12.194167 49.8285 450 MARK3K.cal
B211 BHE 12.1942 49.8285 450 MARK3K.cal
B212 BHZ 12.188667 49.829 480 MARK3K.cal
B212 BHN 12.188667 49.829 480 MARK3K.cal
B212 BHE 12.188667 49.829 480 MARK3K.cal
B221 BHZ 12.198 49.830333 495 GEOPH.cal
B222 BHZ 12.192167 49.825667 470 GEOPH.cal
B223 BHZ 12.183167 49.828167 495 GEOPH.cal
B224 BHZ 12.1845 49.832667 505 GEOPH.cal

B300 BHZ 12.1305 49.780167 487 GEOPH.cal
B310 BHZ 12.134 49.7835 547 GEOPH.cal
B310 BHN 12.134 49.7835 547 GEOPH.cal
B310 BHE 12.134 49.7835 547 GEOPH.cal
B311 BHZ 12.129333 49.778833 490 GEOPH.cal
B312 BHZ 12.1295 49.781667 500 MARK3K.cal
B312 BHN 12.1295 49.781667 500 MARK3K.cal
B312 BHE 12.1295 49.781667 500 MARK3K.cal
B320 BHZ 12.132333 49.7845 540 GEOPH.cal
B321 BHZ 12.1365 49.779667 532 GEOPH.cal
B322 BHZ 12.129833 49.776167 487 MARK3K.cal
B322 BHN 12.129833 49.776167 487 MARK3K.cal
B322 BHE 12.129833 49.776167 487 MARK3K.cal
B323 BHZ 12.123833 49.779 503 GEOPH.cal
B324 BHZ 12.123167 49.784667 520 MARK3K.cal
B324 BHN 12.123167 49.784667 520 MARK3K.cal
B324 BHE 12.123167 49.784667 520 MARK3K.cal

B400 BHZ 12.058166 49.813 598 GEOPH.cal
B410 BHZ 12.056666 49.814333 609 GEOPH.cal
B411 BHZ 12.059 49.810167 615 GEOPH.cal
B412 BHZ 12.053833 49.812 590 GEOPH.cal
B420 BHZ 12.0615 49.8155 555 GEOPH.cal
B421 BHZ 12.062833 49.810833 622 GEOPH.cal
B422 BHZ 12.061166 49.807667 652 MARK3K.cal
B422 BHN 12.061166 49.807667 652 MARK3K.cal
B422 BHE 12.061166 49.807667 652 MARK3K.cal
B423 BHZ 12.049666 49.812 595 MARK3K.cal
B423 BHN 12.049666 49.812 595 MARK3K.cal
B423 BHE 12.049666 49.812 595 MARK3K.cal
B424 BHZ 12.053833 49.817833 560 MARK3K.cal
B424 BHN 12.053833 49.817833 560 MARK3K.cal
B424 BHE 12.053833 49.817833 560 MARK3K.cal

B500 BHZ 12.017333 49.845667 567 MARK3K.cal
B500 BHN 12.017333 49.845667 567 MARK3K.cal
B500 BHE 12.017333 49.845667 567 MARK3K.cal
B510 BHZ 12.017333 49.847 568 GEOPH.cal
B511 BHZ 12.0195 49.844333 539 GEOPH.cal
B512 BHZ 12.014666 49.8455 590 GEOPH.cal
B520 BHZ 12.016 49.848667 590 MARK3K.cal
B520 BHN 12.016 49.848667 590 MARK3K.cal
B520 BHE 12.016 49.848667 590 MARK3K.cal
B521 BHZ 12.023666 49.844333 525 MARK3K.cal
B521 BHN 12.023666 49.844333 525 MARK3K.cal
B521 BHE 12.023666 49.844333 525 MARK3K.cal
B522 BHZ 12.019833 49.839833 560 GEOPH.cal
B523 BHZ 12.009666 49.8425 594 MARK3K.cal
B523 BHN 12.009666 49.8425 594 MARK3K.cal
B523 BHE 12.009666 49.8425 594 MARK3K.cal
B524 BHZ 12.009 49.848833 535 GEOPH.cal
```

Appendix

Example of synthetic.flist-file:

```
    # DATAPATH /home/pamela/POTSDAM-KTB/DATA-TEST-GAUSS/S92/PLOTS/
    # WAVEFORMAT GSE2
    S92-A100/ASCII/19941218000000_0.100 WID2 1994 12 18 00 00 00.000 A100  BHZ      CM6
    4096 105.1524734 3.9655e-15   1.000 NOTYPE  -1.0  0.0
    S92-A100/ASCII/19941218000000_0.110 WID2 1994 12 18 00 00 00.000 A110  BHZ      CM6
    4096 105.1524734 3.9458e-15   1.000 NOTYPE  -1.0  0.0
    S92-A100/ASCII/19941218000000_0.111 WID2 1994 12 18 00 00 00.000 A111  BHZ      CM6
    4096 105.1524734 3.8469e-15   1.000 NOTYPE  -1.0  0.0
    S92-A100/ASCII/19941218000000_0.112 WID2 1994 12 18 00 00 00.000 A112  BHZ      CM6
    4096 105.1524734 3.9476e-15   1.000 NOTYPE  -1.0  0.0
    S92-A200/ASCII/19941218000000_0.200 WID2 1994 12 18 00 00 00.000 A200  BHZ      CM6
    4096 105.1524734 4.0811e-15   1.000 NOTYPE  -1.0  0.0
    S92-A200/ASCII/19941218000000_0.210 WID2 1994 12 18 00 00 00.000 A210  BHZ      CM6
    4096 105.1524734 3.9804e-15   1.000 NOTYPE  -1.0  0.0
    S92-A200/ASCII/19941218000000_0.211 WID2 1994 12 18 00 00 00.000 A211  BHZ      CM6
    4096 105.1524734 4.0692e-15   1.000 NOTYPE  -1.0  0.0
    S92-A200/ASCII/19941218000000_0.212 WID2 1994 12 18 00 00 00.000 A212  BHZ      CM6
    4096 105.1524734 4.0817e-15   1.000 NOTYPE  -1.0  0.0
    S92-A300/ASCII/19941218000000_0.300 WID2 1994 12 18 00 00 00.000 A300  BHZ      CM6
    4096 105.1524734 3.9947e-15   1.000 NOTYPE  -1.0  0.0
    S92-A300/ASCII/19941218000000_0.310 WID2 1994 12 18 00 00 00.000 A310  BHZ      CM6
    4096 105.1524734 4.0185e-15   1.000 NOTYPE  -1.0  0.0
.................
```

Example ktb-region-file:

```
    SWLAT 49.7277
    NELAT 49.9677
    DLAT 0.006
    NUM_LATSTEP 41
    SWLON 11.9989
    NELON 12.2522
    DLON 0.010
    NUM_LONSTEP 41
    MINDEPTH 0.0
    MAXDEPTH 33.0
    NUM_H 34
    DH 1
```

Output-files for CAP

Example file.max:

```
# Start of processing at Sat Nov  6 11:46:36 2010
# cap was started with the following comand line
# cap_sa -f 19941218000000.000 -l 19941218000100.000 -i mig-z.cfg -g
B300+B310+B311+B312+B320+B321+B322+B323+B324 -s B300.slist -w synthetic.flist -m SB300.SS-
S92.tttable -o SB300-Z.SS-S92
# We got the following parameters from the configuration file
# METHOD 16
# HYPMETH 0
# TFPOLJURK_TH1 0.900000
# TFPOLJURK_TH2 0.000000
# TFENERGY_TH1 0.010000
# TFENERGY_TH2 0.800000
# PREWHITEN 0
# SIMPLENORM OFF
# DETECT_DOMINANT 0
# SINGVAL_RATIO 10.000000
# SLOWRESP 0
# NUM_BANDS 1
# LOWEST_CFREQ 0.050000
# HIGHEST_CFREQ 0.210000
```

Appendix

```
# BANDWIDTH 0.800000
# BANDSTEP -1.000000
# SPATIAL_SMOOTH 0
# NRC_SELECT FULL
# OMEGA -1.000000
# APRIORI 1.000000
# CR@1HZ 0.600000
# CREXP 0.100000
# BESSMINARG 0.4
# BESSMAXARG 3.2
# GRID_LAYOUT 0
# GRID_TYPE 0
# GRID_RESOL 301
# NPHI 360
# GRID_MAX 0.300000
# LINEAR_PHI 220.000000
# MAPFRAC 0.000010
# NSTACK 5000
# SEED 0
# COMP 1
# WINFAC -5.000000
# OVERLAP -1.000000
# WINLEN 0.200000
# STEP 0.100000
# TAPER_FRAC 0.200000
# POWSPEC 0
# KOSMOOTH 30
# STRIKE -1.000000
# OUTPUT_FILE test.out
# OFILE_TYPE 0
# WRITE_TRACES 1
# DECIMATE 1
# SEIDL 0
# FSIM 0.002000
# HSIM 0.707000
# BBP_FILTER 0
# BBP_LOW 1.000000
# BBP_HIGH 30.000000
# BBP_ORDER 2
# ZERO_PHASE 0
# GAUSSNOISE 0.050000
# TIME_CORR 0
# 3DCORRECT 0
# List of frequency bands selected for processing:
# Bandstep: inf
# List of stations selected for processing:
# start stat B300 chan 1 19941218000000.000
# start stat B310 chan 1 19941218000000.000
# start stat B311 chan 1 19941218000000.000
# start stat B312 chan 1 19941218000000.000
# start stat B320 chan 1 19941218000000.000
# start stat B321 chan 1 19941218000000.000
# start stat B322 chan 1 19941218000000.000
# start stat B323 chan 1 19941218000000.000
# start stat B324 chan 1 19941218000000.000
# Common sampling frequency: 105.152468
0 787708802.000000 49.781700 12.128900 13.000000 0.965639 33610389456284.109375 -0.164021
```